

# Design, Calibration, and Performance of the MINERvA Detector

L. Aliaga<sup>a</sup>, L. Bagby<sup>b</sup>, B. Baldin<sup>b</sup>, A. Baumbaugh<sup>b</sup>, A. Bodek<sup>c</sup>, R. Bradford<sup>c,1</sup>, W.K. Brooks<sup>d</sup>, D. Boehnlein<sup>b</sup>, S. Boyd<sup>e</sup>, H. Budd<sup>c</sup>, A. Butkevich<sup>f</sup>, D.A. Martinez Caicedo<sup>g</sup>, C.M. Castromonte<sup>g</sup>, M.E. Christy<sup>h</sup>, J. Chvojka<sup>c</sup>, H. da Motta<sup>g</sup>, D.S. Damiani<sup>a</sup>, I. Danko<sup>e</sup>, M. Datta<sup>h</sup>, R. DeMaat<sup>b,2</sup>, J. Devan<sup>a</sup>, E. Draeger<sup>i</sup>, S.A. Dytman<sup>e</sup>, G.A. Díaz<sup>j</sup>, B. Eberly<sup>e</sup>, D.A. Edmondson<sup>a</sup>, J. Felix<sup>k</sup>, L. Fields<sup>l</sup>, G.A. Fiorentini<sup>g</sup>, A.M. Gago<sup>m</sup>, H. Gallagher<sup>n</sup>, C.A. George<sup>e</sup>, C. Gingu<sup>b</sup>, B. Gobbi<sup>l,2</sup>, R. Gran<sup>i</sup>, N. Grossman<sup>b</sup>, D. A. Harris<sup>b,\*</sup>, J. Heaton<sup>i</sup>, A. Higuera<sup>k</sup>, J.A. Hobbs<sup>l</sup>, I.J. Howley<sup>a</sup>, K. Hurtado<sup>g,m</sup>, M. Jenkins<sup>o</sup>, T. Kafka<sup>n</sup>, M.O. Kantner<sup>a</sup>, C. Keppel<sup>h,3</sup>, J. Kilmer<sup>b</sup>, A.H. Krajieski<sup>a</sup>, H. Lee<sup>c</sup>, A.G. Leister<sup>a</sup>, G. Locke<sup>s</sup>, G. Maggi<sup>d,4</sup>, E. Maher<sup>p</sup>, S. Manly<sup>c</sup>, W.A. Mann<sup>n</sup>, C.M. Marshall<sup>c</sup>, K.S. McFarland<sup>c</sup>, C.L. McGivern<sup>e</sup>, A. M. McGowan<sup>c</sup>, J.G. Morfin<sup>b</sup>, J. Mousseau<sup>q</sup>, D. Naples<sup>e</sup>, J.K. Nelson<sup>a</sup>, G. Niculescu<sup>r</sup>, I. Niculescu<sup>r</sup>, C.D. O'Connor<sup>a</sup>, N. Ochoa<sup>j</sup>, J. Olsen<sup>b</sup>, B. Osmanov<sup>q</sup>, J. Osta<sup>b</sup>, J.L. Palomino<sup>g</sup>, V. Paolone<sup>e</sup>, J. Park<sup>c</sup>, G. N. Perdue<sup>c</sup>, C. Peña<sup>d</sup>, A. Pla-Dalmau<sup>b</sup>, L. Rakotondravohitra<sup>b,5</sup>, R. D. Ransome<sup>s</sup>, H. Ray<sup>q</sup>, L. Ren<sup>e</sup>, P. Rubinov<sup>b</sup>, C. Rude<sup>i</sup>, K.E. Sassin<sup>a</sup>, H. Schellman<sup>l</sup>, D.W. Schmitz<sup>t,b</sup>, R.M. Schneider<sup>a</sup>, C. Simon<sup>u</sup>, F.D. Snider<sup>b</sup>, M.C. Snyder<sup>a</sup>, C.J. Solano Salinas<sup>m</sup>, N. Tagg<sup>v</sup>, B. G. Tice<sup>s</sup>, R.N. Tilden<sup>l</sup>, G. Tzanakos<sup>w,2</sup>, J.P. Velásquez<sup>j</sup>, T. Walton<sup>h</sup>, A. Westerberg<sup>i</sup>, J. Wolcott<sup>c</sup>, B.A. Wolthuis<sup>a</sup>, N. Woodward<sup>i</sup>, T. Wytock<sup>l</sup>, G. Zavala<sup>k</sup>, D. Zhang<sup>a</sup>, L.Y. Zhu<sup>h</sup>, B.P. Ziemer<sup>u</sup>

<sup>a</sup>Department of Physics, College of William & Mary, Williamsburg, Virginia 23187, USA

<sup>b</sup>Fermi National Accelerator Laboratory, Batavia, Illinois 60510, USA

<sup>c</sup>University of Rochester, Rochester, New York 14610 USA

<sup>d</sup>Departamento de Física, Universidad Técnica Federico Santa María, Avda. España 1680 Casilla 110-V Valparaíso, Chile

<sup>e</sup>Department of Physics and Astronomy, University of Pittsburgh, Pittsburgh, Pennsylvania 15260, USA

<sup>f</sup>Institute for Nuclear Research of the Russian Academy of Sciences, 117312 Moscow, Russia

<sup>g</sup>Centro Brasileiro de Pesquisas Físicas, Rua Dr. Xavier Sigaud 150, Urca, Rio de Janeiro, RJ, 22290-180, Brazil

<sup>h</sup>Hampton University, Dept. of Physics, Hampton, Virginia 23668, USA

<sup>i</sup>Department of Physics, University of Minnesota – Duluth, Duluth, Minnesota 55812, USA

<sup>j</sup>Sección Física, Departamento de Ciencias, Pontificia Universidad Católica del Perú, Apartado 1761, Lima, Perú

<sup>k</sup>Lascuran de Retana No. 5, Col. Centro. Guanajuato 36000, Guanajuato. Mexico

<sup>l</sup>Northwestern University, Evanston, Illinois 60208

<sup>m</sup>12 Facultad de Ciencias, Universidad Nacional de Ingeniera, Apartado 31139, Lima, Perú

<sup>n</sup>Physics Department, Tufts University, Medford, Massachusetts 02155, USA

---

\*Corresponding Author

Email address: dharris@fnal.gov (D. A. Harris)

<sup>1</sup>Present Address: Argonne National Laboratory, 9700 S. Cass Avenue, Lemont, IL 60439, USA

<sup>2</sup>Deceased.

<sup>3</sup>Present Address: now at the Thomas Jefferson National Accelerator Facility, Newport News, VA 23606 USA

<sup>4</sup>Present Address: now at Vrije Universiteit Brussel, Pleinlaan 2, B-1050 Brussels, Belgium

<sup>5</sup>Present Address: also at Department of Physics, University of Antananarivo, Madagascar

<sup>o</sup>Department of Physics, University of Texas, 1 University Station, Austin, Texas 78712, USA

<sup>p</sup>Massachusetts College of Liberal Arts, 375 Church Street, North Adams, Massachusetts 01247

<sup>q</sup>University of Florida, Department of Physics, Gainesville, Florida 32611, USA

<sup>r</sup>James Madison University, Harrisonburg, Virginia 22807, USA

<sup>s</sup>Rutgers, The State University of New Jersey, Piscataway, New Jersey 08854, USA

<sup>t</sup>Enrico Fermi Institute, University of Chicago, Chicago, Illinois 60637, USA

<sup>u</sup>Department of Physics and Astronomy, University of California, Irvine, Irvine, California 92697, USA

<sup>v</sup>Department of Physics, Otterbein University, 1 South Grove Street, Westerville, Ohio, 43081, USA

<sup>w</sup>Department of Physics, University of Athens, GR-15771 Athens, Greece

---

## Abstract

The MINERvA<sup>1</sup> experiment is designed to perform precision studies of neutrino-nucleus scattering using  $\nu_\mu$  and  $\bar{\nu}_\mu$  neutrinos incident at 1-20 GeV in the NuMI beam at Fermilab. This article presents a detailed description of the MINERvA detector and describes the *ex situ* and *in situ* techniques employed to characterize the detector and monitor its performance. The detector is comprised of a finely-segmented scintillator-based inner tracking region surrounded by electromagnetic and hadronic sampling calorimetry. The upstream portion of the detector includes planes of graphite, iron and lead interleaved between tracking planes to facilitate the study of nuclear effects in neutrino interactions. Observations concerning the detector response over sustained periods of running are reported. The detector design and methods of operation have relevance to future neutrino experiments in which segmented scintillator tracking is utilized.

*Keywords:* NuMI, MINERvA, Neutrinos, Cross Sections, Nuclear Effects

---

## Contents

<b>1</b>	<b>Experiment Overview</b>	<b>4</b>
1.1	MINERvA Physics Goals and Detector Design . . . . .	6
1.2	The MINOS Near Detector . . . . .	9
1.3	The NuMI Neutrino Beam at Fermilab . . . . .	10

---

<sup>1</sup>Main INjector ExpeRiment  $\nu$ -A

<b>2</b>	<b>Module Assemblies and Nuclear Targets</b>	<b>11</b>
2.1	Tracking Modules . . . . .	12
2.2	Electromagnetic and Hadronic Calorimeter Modules . . . . .	13
2.3	Solid Nuclear Target Modules . . . . .	14
2.4	Water Target . . . . .	16
2.5	Liquid Helium Target . . . . .	18
<b>3</b>	<b>The Optical System</b>	<b>20</b>
3.1	Scintillator . . . . .	20
3.2	Wavelength Shifting Fibers . . . . .	22
3.3	Optical Connectors and Clear Fiber Cables . . . . .	24
3.4	Photomultiplier Tubes and Optical Boxes . . . . .	26
3.5	Readout Electronics and Data Acquisition . . . . .	31
<b>4</b>	<b>Event Formation and Hit Calibration Chain</b>	<b>31</b>
<b>5</b>	<b><i>Ex situ</i> Calibrations of Optical System Components</b>	<b>36</b>
5.1	Module Mapper . . . . .	36
5.2	PMT Testing . . . . .	39
5.3	FEB Response Measurements . . . . .	40
<b>6</b>	<b><i>In situ</i> Calibrations and Monitoring</b>	<b>42</b>
6.1	Pedestal Monitoring . . . . .	43
6.2	PMT Gain Monitoring . . . . .	44
6.2.1	Light Injection System . . . . .	45
6.2.2	Gain Calculation . . . . .	46
6.3	Scintillator Plane Alignment . . . . .	50
6.4	Relative Strip-to-Strip Response Variations . . . . .	51
6.5	Absolute Energy Scale Determination Using Minimum Ionizing Particles . .	55
6.6	Timing Calibration . . . . .	58

6.7	Cross-talk Measurements . . . . .	61
<b>7</b>	<b>Muon Reconstruction</b>	<b>64</b>
7.1	Cluster Formation . . . . .	65
7.2	Track Reconstruction in MINERvA . . . . .	67
7.3	Charge Determination and Energy Reconstruction . . . . .	71
7.4	Muon Reconstruction Efficiency and Acceptance . . . . .	75
<b>8</b>	<b>Recoil Energy Reconstruction</b>	<b>76</b>
<b>9</b>	<b>Test Beam Detector Response Calibration</b>	<b>79</b>
9.1	Pions . . . . .	81
9.2	Protons . . . . .	83
9.2.1	Stopping protons and Birks' parameter . . . . .	83
<b>10</b>	<b>Detector Performance</b>	<b>85</b>
10.1	Charged Current Interactions . . . . .	85
10.2	Energy Loss for Stopping Particles . . . . .	86
10.3	Michel Electrons . . . . .	87
10.4	Energy loss by Electrons and Photons . . . . .	89
<b>11</b>	<b>Conclusions</b>	<b>90</b>
<b>12</b>	<b>Acknowledgments</b>	<b>92</b>

## 1. Experiment Overview

There are many uncertainties in the knowledge of the fundamental interactions of neutrinos with the nucleon and the more complex interactions with nuclei. The properties of the neutrino, such as its purely weak interaction and its unique flavor sensitivity, make it an ideal probe, but its small cross sections, together with the difficulty of producing intense neutrino beams, have impeded detailed investigations of the interaction. The

intense neutrino beam produced in the Neutrinos at the Main Injector (NuMI) beamline [1] at Fermilab has opened up new possibilities for the detailed study of neutrino interactions with nuclei. The MINERvA experiment takes advantage of this new opportunity. MINERvA is studying neutrino interactions on a variety of nuclei, including helium, carbon, oxygen, lead, and iron, which complement the wealth of electron scattering data in helping to understand the weak interaction in the nuclear environment.

The field of neutrino oscillations is rapidly advancing towards our understanding the complete picture of neutrino masses and mixings [2, 3, 4, 5]. In particular, the next generation of accelerator-based long-baseline experiments aims to determine the mass hierarchy of neutrinos and test for CP violation by comparing the oscillation probabilities for neutrinos and antineutrinos. Reaching the level of precision needed in these challenging measurements requires a detailed understanding of neutrino- and antineutrino-nucleus scattering processes in the relevant energy range of a few hundred MeV to a few GeV. Currently, however, the specific processes that provide signal and background channels for these experiments are, in many cases, either poorly measured or suffer from discrepant measurements across various experiments. In addition, an important feature of oscillation experiments is the need to measure oscillation probabilities as a function of the neutrino energy. This requires experiments to have robust models of the relationship between the initial neutrino energy and the visible energy deposited in the detectors. Such models must incorporate the impact of the complex nuclear environment in which the interactions are occurring; studies have shown that neglecting these effects can lead to biases in the neutrino energy determination. Both the impact of the initial state and the interactions of final-state particles traversing the parent nucleus must be understood. Through measurements of specific interaction cross sections and comparisons among different nuclear targets, MINERvA can provide data to considerably improve the models of neutrino-nucleus scattering and thus to reduce systematic uncertainties in the results from oscillation experiments.

### 1.1. MINERvA Physics Goals and Detector Design

The key design features of the MINERvA detector have been determined by the physics goals of the experiment. An overview of the detector design and its component systems is presented in this section. Detailed technical descriptions of the main components are provided in subsequent sections.<sup>6</sup>

The physics goals of MINERvA require a detector that can resolve multi-particle final states, identify the produced particles, track low energy charged particles (for energies greater than about 100 MeV), contain electromagnetic showers, contain high-energy (up to at least 10 GeV) final states, and resolve multiple interactions in a single beam spill. The detector must include targets with a wide range of nucleon number  $A$  to enable studies of the nuclear dependence of neutrino interactions. In order to track and resolve multi-particle final states with low thresholds, the core of the detector must be fully active with good spatial resolution and of relatively low mass. Full containment of events requires that the inner region be surrounded with electromagnetic and hadronic calorimetry. Ideally, charge identification would be included by adding a magnetic field. This proved impractical for the main detector, as did containment of high energy muons. However, by placing MINERvA immediately upstream of the Main Injector Oscillation Search (MINOS) near detector [6] (henceforth referred to as MINOS), a neutrino detector composed of magnetized iron plates interleaved with scintillator planes, charge and energy measurements of forward-going muons can be made.

A schematic view of the detector is shown in Fig. 1. Neutrino reactions in the rock upstream of the detector hall can produce hadrons and muons. A “veto wall” upstream of the main detector shields against lower energy hadrons from the rock and tags the muons (referred to below as “rock muons”), which can traverse all or part of the downstream detector. The veto wall consists of a 5 cm thick steel plate, a 1.9 cm thick plane of scintillator, a 2.5 cm thick steel plate, and a second plane of 1.9 cm thick scintillator. A cubic meter

---

<sup>6</sup>The doctoral dissertation of Jesse Chvojka [7] contains additional detail on aspects of the detector which are beyond the scope of this paper.

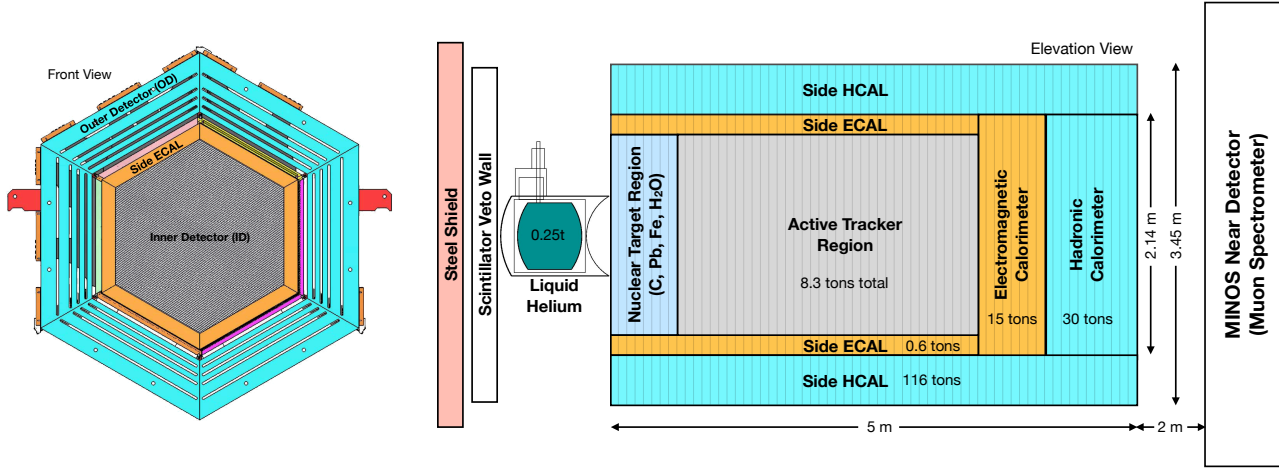


Figure 1: Schematic views of the MINERvA detector. Left: front view of a single detector module. Right: side view of the complete detector showing the nuclear target, the fully-active tracking region and the surrounding calorimeter regions.

cryogenic vessel filled with liquid helium, described below, is placed between the veto wall and the main detector.

The main MINERvA detector is segmented transversely into: the inner detector (ID), with planes of solid scintillator strips mixed with the nuclear targets; a region of pure scintillator; downstream electromagnetic calorimetry (ECAL) and hadronic calorimetry (HCAL); and an outer detector (OD) composed of a frame of steel with imbedded scintillator, which also serves as the supporting structure. Both the ID and OD are in the shape of a regular hexagon. For construction and convenience of handling, a single unit of MINERvA incorporates both the scintillator and outer frame. Up to two planes of scintillator are mounted in one frame, called a “module”. Figure 1 (left) shows a view of a tracking module. There are three orientations of strips in the tracking planes, offset by  $60^\circ$  from each other, which enable a three-dimensional reconstruction of tracks. The  $60^\circ$  offset fits naturally with the hexagonal transverse cross section of the detector.

The MINERvA coordinate system is defined such that the  $z$  axis is horizontal and points downstream along the central axis of the detector, the  $y$  axis points upward, and

the  $x$  axis is horizontal pointing to beam left, with the  $x - y$  origin at the center of the ID. The  $z$  axis is defined to place the front face of MINOS at  $z = 1,200$  cm. In this system the neutrino beam central axis is in the  $y - z$  plane and points downward at  $3.34^\circ$ .

The core of the MINERvA design is the active tracking region, composed purely of scintillator, which serves as the primary fiducial volume where precise tracking, low density of material, and fine sampling ensure that some of the most difficult measurements can be performed. These measurements include particle identification using energy loss per unit length ( $dE/dx$ ), and reconstruction of the neutrino interaction vertex in the presence of several final state charged particles. The upstream part of the detector contains solid targets of carbon, iron, and lead interleaved with the scintillator planes. Because these targets are relatively thin, the ability to precisely reconstruct the location of the interaction vertex is crucial for studies of the  $A$  dependence.

Electromagnetic calorimetry is accomplished using a 0.2 cm thick by 15 cm wide lead “collar” (orange ring in Fig. 1) between each scintillator plane in the central tracking region. Additionally there are lead plates, each 0.2 cm thick and covering the full transverse span of the inner detector, which are deployed between each scintillator plane within the 10 modules immediately downstream of the tracking region. For hadronic calorimetry the outer frames of all modules are instrumented with strips of scintillator interleaved into the steel. Further, in the most downstream 20 modules of the detector, the inner detector scintillator planes alternate with 2.54 cm thick steel plates. Thus the combination of the outer frame detectors and the downstream calorimeter section provides containment of hadrons initiated by interactions in the tracking region.

The MINERvA experiment uses several different simulation codes to model the detector and its performance. The neutrino interactions are modeled by the GENIE v2.6.2 event generator [8]. The final-state particle interactions in the detector itself are modeled by a GEANT4 version 9.4.p02 [9] simulation. The different detector components such as the electronics and scintillator and absorbers are also modeled using GEANT4. Both the GENIE and GEANT4 parts of the detector simulation include a detailed model of the



nuclear makeup of the detector, described in Sec. 2.1 and Sec. 2.3. The simulation also takes into account the variations over time and position of the detector components, and includes accidental detector activity.

### 1.2. The MINOS Near Detector

The MINERvA detector is situated 2.1 meters upstream of the MINOS near detector in the NuMI beamline. The MINOS magnetic spectrometer is used to momentum analyze muons which exit the MINERvA detector volume in the forward direction. The detector technology and readout are described in detail in Ref. [6]. The segmentation and layout of the MINOS near detector are described in this section. Performance aspects relevant to its use for MINERvA are discussed in Sec. 7.2.

MINOS, shown in Fig. 2, is a tracking calorimeter composed of planes of magnetized iron and plastic scintillator with a total mass of 1 kTon. It has a toroidal magnetic field of average strength of 1.3 T, which is produced by a current-carrying coil passing through the entire length of the detector. The direction of curvature of a charged particle in the field allows the sign of the track charge to be determined. In the normal operational mode, the field is set to focus the same charge as that selected in the NuMI secondary beam focusing system.

MINOS consists of 282 steel plates, each 2.54 cm thick, of which 152 are instrumented with 1 cm thick scintillator planes. The scintillator planes are made of 4.1 cm wide strips oriented  $\pm 45^\circ$  with respect to the vertical and alternating  $\pm 90^\circ$  in successive planes. In the upstream region (“calorimeter region”), comprising the first 120 planes, a partially-instrumented (or fully-instrumented every fifth plane) scintillator plane follows each steel plane. In the downstream 162 planes (“muon spectrometer”), there are no partially-instrumented planes and every fifth plane has full scintillator coverage. In the spectrometer region, the signals from four different pixels in a spectrometer plane are electrically summed prior to digitization.

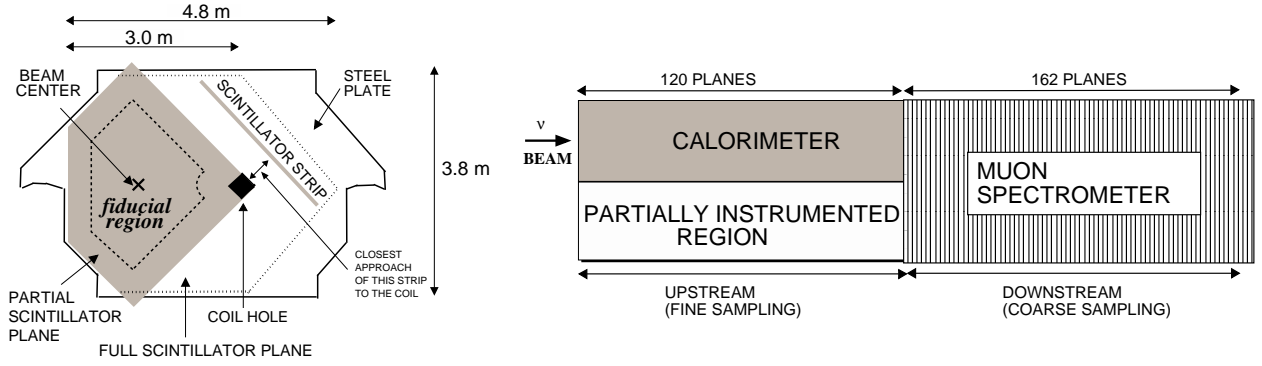


Figure 2: Schematic view of the MINOS Near Detector. Left: transverse view of a Near Detector plane. The shaded area shows a partially instrumented active scintillator plane and the dashed line within shows the boundary of the fiducial region. The dotted line shows the outline of a fully instrumented scintillator plane. Right: top view showing the calorimeter and muon spectrometer. The drawing is not to scale. Figure taken from Ref. [10]

### 1.3. The NuMI Neutrino Beam at Fermilab

MINERvA uses the Fermilab NuMI beamline to produce a high intensity beam of muon neutrinos and anti-neutrinos [1]. A beam of 120 GeV protons from the Main Injector strikes a graphite target over an 8.1 or 9.72  $\mu\text{s}$  spill every 2.2 seconds. The two different spill durations correspond to different modes of operation for the accelerator complex. The secondary pions and kaons produced by the incident protons are then focused by a system of two magnetic horns which direct the mesons into a 675 m long decay pipe where most of them decay. A total of 240 m of rock downstream of the decay pipe range out the tertiary muons that are created in the beamline concurrently with the neutrinos.

The focusing horns can be pulsed in either polarity. When the horns are focusing positively charged mesons (forward horn current or FHC) the resulting beam is primarily neutrinos, and when the horn is in the reverse horn current (RHC) the peak of the beam is primarily anti-neutrinos. MINERvA collected data with  $4.0 \times 10^{20}$  ( $1.7 \times 10^{20}$ ) protons on target in FHC (RHC) over the period of time described in this article (March 2010 through April 2012).

The NuMI beamline has considerable flexibility and can run with the target in different positions relative to the focusing horns. For most of the run the graphite target was

located as close to the horns as possible to create a beam whose energy of the peak in neutrino flux was approximately 3 GeV, a configuration known as the low energy (LE) beam. Of the total exposure roughly 10% of the protons on target were collected in configurations with the target moved farther upstream of the first horn, which results in a higher peak-neutrino-energy flux. These special runs were taken to better understand the neutrino flux, but the detector calibration and reconstruction procedures remained the same as those described in the remainder of this article. Future runs will use a horn separation that gives a higher peak neutrino energy.

As discussed in Sec. 6.5, an important calibration source produced by this beam comes from muons resulting from neutrino charged-current interactions that occur in the rock located upstream of the MINERvA detector. On average once every two beam pulses a rock muon traverses the entire central tracking region of the MINERvA detector.

## 2. Module Assemblies and Nuclear Targets

The MINERvA detector is comprised of 120 modules suspended vertically and stacked along the beam direction. There are four basic types of modules: tracking modules, electromagnetic calorimeter modules, hadronic calorimeter modules, and passive nuclear targets. The four types of modules are distinguished by their makeup in the ID region; the outer module frames are identical except for their thickness. The OD frames provide structural support, alignment, and outer hadronic calorimetry. Each hexagonal steel frame is 56 cm wide and instrumented with eight strips of scintillator of varying lengths to span each wedge in the frame. The OD frames are 3.49 cm thick, except in the HCAL, where they are 3.81 cm thick due to the steel plates being thicker than scintillator planes. Successive modules are connected with bolts that ensure a 2.5 mm air gap between pairs of scintillator planes. The air gap between the steel frames is 8.7 mm.

The subsections below provide detailed descriptions of the construction and material composition of each module type. The material composition of the tracking planes, in particular, has relevance for the interpretation of cross sections measured by the MIN-

ERvA detector.

### 2.1. Tracking Modules

Tracking modules consist of two scintillator planes each composed of triangular scintillator strips, described in Section 3.1. Each plane consists of 127 strips glued together with 3M-DP190 translucent epoxy. Sheets of Lexan cover the planes and are attached with 3M-DP190 gray epoxy to make them light tight and to add rigidity. Black PVC electrical tape is used to seal joints in the Lexan and patch any light leaks. Optical epoxy (Epon Resin 815C and Epicure 3234) provides the coupling between the scintillator and WLS fibers.

A plane can have one of three different orientations, referred to as X-planes, U-planes or V-planes according to the coordinate in the MINERvA system in which each plane measures particle hit positions. X-planes have scintillator strips aligned vertically, hence hits in this view give position information in the horizontal or  $x$ -direction. The U- and V-planes are rotated 60 degrees clockwise and counterclockwise from the X-planes in the  $x$ - $y$  plane, respectively. Three different views are used in order to avoid ambiguities with reconstructed hit associations that can occur when multiple tracks traverse two orthogonal planes. Each tracking and electromagnetic calorimeter module has one X-plane, and either a U- or V-plane, with modules alternating between a UX or VX structure with the X-planes always located downstream of the U- or V-planes. The nuclear target region contains 22 tracking modules, and the central tracking region contains 62 tracking modules.

The tracking modules are designed to perform electromagnetic calorimetry using a 0.2 cm thick lead collar that starts at roughly 90 cm from the module center and extends to the outer frame. The collar forms a hexagonal ring whose purpose is to reduce the leakage of electromagnetic showers that originate in the central detector.

The chemical composition and areal density (mass per unit surface area) of the planes is determined by combining measured densities (pure scintillator and coated strips), assayed compositions (coated strips and epoxies), and data sheet values (tape and Lexan).

Material	Density (g/cm <sup>3</sup> )	H	C	N	O	Al	Si	Cl	Ti
Scintillator	1.043 ± 0.002	7.6%	92.2%	0.06%	0.07%	-	-	-	-
Coating	1.52	6.5%	78.5%	-	6.0%	-	-	-	9.0%
Lexan	1.2	6.7%	66.7%	-	26.7%	-	-	-	-
PVC tape	1.2	4.8%	38.7%	-	-	-	-	56.5%	-
DP190 transl.	1.32	10.0%	69.0%	2.6%	17.0%	-	-	0.5%	-
DP190 gray	1.70	5.0%	47.0%	1.7%	27.0%	6.0%	6.0%	0.05%	-

Table 1: Density and elemental composition by mass percentage for the various materials in the scintillator planes.

Component	H	C	O	Al	Si	Cl	Ti
Strip	7.59%	91.9%	0.51%	-	-	-	0.77%
Plane	7.42%	87.6%	3.18%	0.26%	0.27%	0.55%	0.69%

Table 2: Elemental composition of scintillator strips and constructed planes, by mass percentage.

The estimated areal densities of the epoxy and tape are based on their usage in plane construction. The densities and composition of the components are listed in Table 1. The elemental compositions of the strips and assembled tracker scintillator plane are given in Table 2. The chemical composition of the components is well known. There is some uncertainty in the composition of the coated strips due to the uncertainty in the coating thickness, which is estimated to have a relative uncertainty of about 10%. This affects most strongly the fraction of the strips which is scintillator. The estimated areal density for the scintillator plane is  $1.65 \pm 0.03$  g/cm<sup>2</sup>. The estimated areal density of an assembled plane is  $2.02 \pm 0.03$  g/cm<sup>2</sup>, as described in Sec. 3.1.

## 2.2. Electromagnetic and Hadronic Calorimeter Modules

An ECAL module is very similar to a central tracking module. It differs in that it has a 0.2 cm thick sheet of lead covering that the entire scintillator plane instead of a 0.2 cm thick lead collar covering only the outer edge of the scintillator region. A transition

module is placed between the last central tracking module and first ECAL module. This module contains a 0.2 cm thick lead sheet on the downstream end of the last plane in the module so that each plane of the ECAL has a lead absorber upstream of it. The fine granularity of the ECAL ensures excellent photon and electron energy resolution and provides directional measurement for these particles. There are 10 modules in the ECAL region of the detector (Fig. 1).

The lead sheets used for the side electromagnetic calorimetry were measured using an ultrasonic device to determine the variation in thickness along the length of the sheet. The thickness along each piece vary at the 5% level, and the average thickness of the different pieces vary at the 3.5% level. The thicknesses of the lead sheets used in the downstream electromagnetic calorimetry also vary at this level.

The HCAL consists of 20 modules that are similar to the tracking modules; however, instead of two planes of scintillator in each module, there is only one plane of scintillator and one 2.54 cm thick hexagonal steel plane in the inner detector region. The scintillator planes located in the HCAL have a repeating pattern of XVXU.

### 2.3. *Solid Nuclear Target Modules*

In order to study neutrino interactions on different nuclei, the most upstream part of the detector includes five layers of passive targets, the “nuclear targets”, separated by four tracking modules each. The four modules (eight planes of scintillator) between one target and the next ensure good vertex position resolution for events originating in the nuclear targets. Each solid nuclear target is mounted in the same instrumented hexagonal steel frame as the scintillator planes for ease of detector construction and for event containment. The five targets are configured such that the thicker targets are most upstream, and the thinner targets are downstream. This optimizes reconstruction of events occurring upstream. The thinner targets are included in order to study specific reactions that contain low-momentum final-state particles. Except for the fourth of the five targets, all contain mixed materials with different orientations in order to minimize the effect of acceptance differences for different regions of the detector. Target 4 is pure lead and

Material	Density (g/cm <sup>3</sup> )	C	Si	Mn	Fe	Cu	Pb
Steel	$7.83 \pm 0.03$	0.13%	0.2%	1.0%	98.7%	-	-
Lead	$11.29 \pm 0.03$	-	-	-	-	0.05%	99.95%
Graphite	$1.74 \pm 0.01$	>99.5%	-	-	-	-	-

Table 3: Density and element composition by mass percentage for the nuclear targets.

aids in upstream electromagnetic calorimetry and serves as the thinnest lead target. Targets 1, 2, and 5 are mixed steel and lead. The steel plate section is larger than the lead plate section, with the dividing line 20.5 cm from the plane center. Target 3 is composed of graphite, iron and steel. The graphite covers half the area of the hexagon, the steel one-third, and the lead one-sixth. The orientation of the planes, as viewed looking downstream, is shown in Fig. 3. The orientation of the planes along the axis of the beamline is shown in Fig. 4. The composition by element of the targets is given in Table 3.

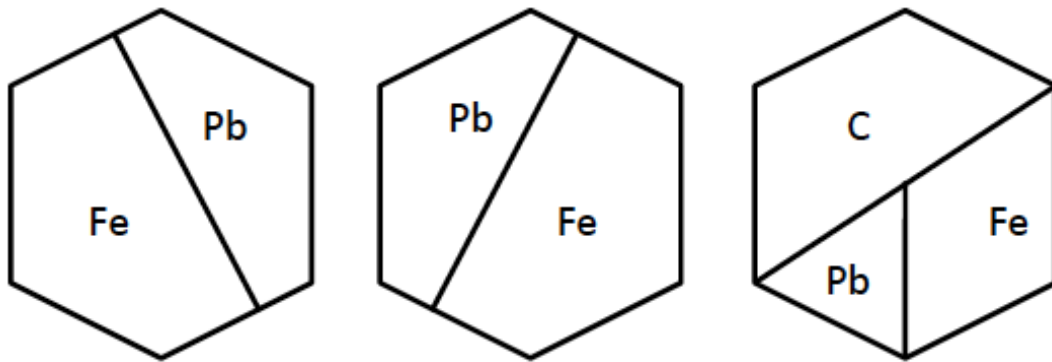


Figure 3: Orientation of the nuclear targets looking downstream. Targets 1 and 5 have the leftmost orientation, target 2 the middle orientation, and target 3 the rightmost orientation.

The residual radioactivity of the lead was measured by the Fermilab Radionuclide Analysis Facility to be below the maximum allowable radioactivity of  $0.15 \gamma/\text{sec}/\text{kg}$  with energy above 0.5 MeV. The fiducial area for the mixed targets is bounded by a hexagon

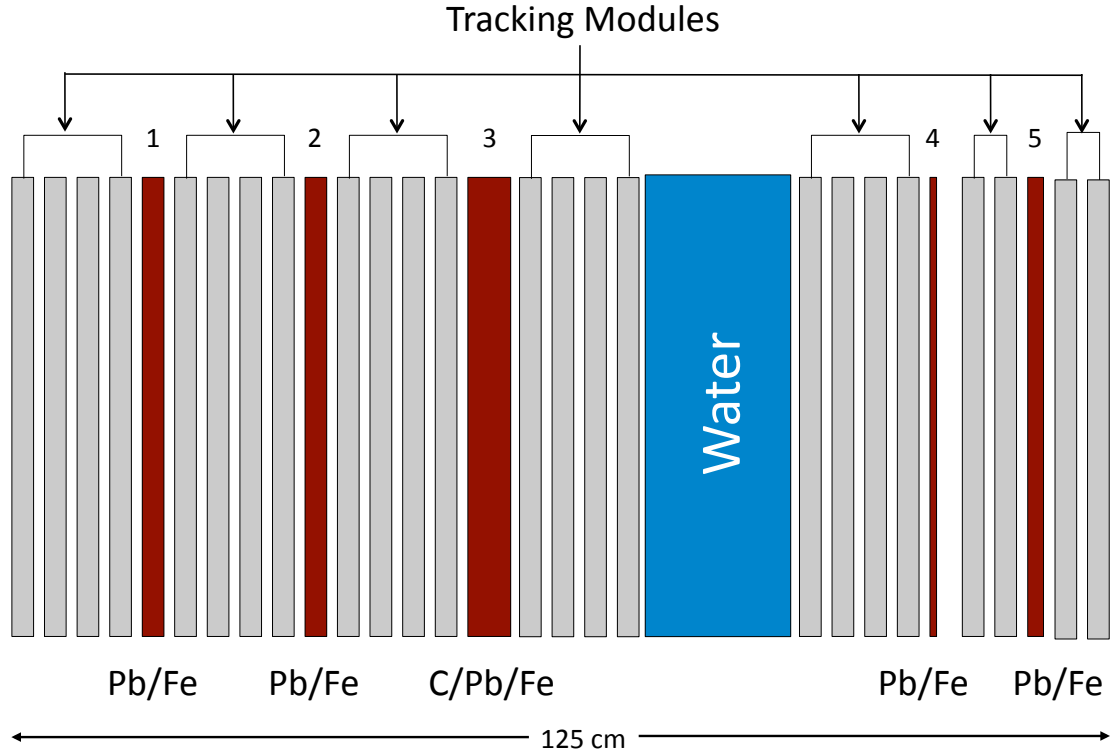


Figure 4: Orientation of the nuclear target region along the beamline axis. The thinner targets are located downstream and the thicker targets are located upstream.

with an 85 cm apothem, and a 2.5 cm cut on each side of the boundary between materials. The  $z$ -location of the center of each target and the fiducial mass of each material for each target is given in Table 4. The estimated uncertainty on the fiducial masses due to density and thickness variations is less than 1%.

#### 2.4. Water Target

A water target is positioned between solid targets 3 and 4, with a mean position of 530.8 cm. It consists of a circular steel frame with a diameter slightly larger than the MIN-ERvA inner detector size, and Kevlar® (polymerized  $C_{14}H_{10}N_2O_2$ ) sheets stretched across the frame as shown in Fig. 5. The shape of the water target is not as well known as that of the solid targets. When the target is filled the lower part expands more than the upper



Target	$z$ -location (cm)	Thickness (cm)	Fiducial Area (cm <sup>2</sup> )	Fiducial Mass (kg)	Total Mass (kg)
1-Fe	452.5	$2.567 \pm 0.006$	15999	322	492
1-Pb	452.5	$2.578 \pm 0.012$	9029	263	437
2-Fe	470.2	$2.563 \pm 0.006$	15999	321	492
2-Pb	470.2	$2.581 \pm 0.016$	9029	263	437
3-Fe	492.3	$2.573 \pm 0.004$	7858	158	238
3-Pb	492.3	$2.563 \pm 0.004$	3694	107	170
3-C	492.3	$7.620 \pm 0.005$	12027	160	258
Water	528.4	17-24	25028	452	627
4-Pb	564.5	$0.795 \pm 0.005$	25028	225	340
5-Fe	577.8	$1.289 \pm 0.006$	15999	162	227
5-Pb	577.8	$1.317 \pm 0.007$	9029	134	204

Table 4: Nuclear target locations, thickness and fiducial mass. The total mass is for the entire plate of target material. The location is in the MINERvA coordinate system, which is defined in the text.

part, and it is not possible to access the entire target in order to make precise measurements. The shape of the target is estimated via a finite element analysis and compared with the actual volume, which is determined by measuring the volume of water when the target is emptied. The thickness varies from about 17 cm at the edge of the fiducial region to 24 cm at the thickest part. The estimated mass within an 85 cm apothem hexagon is 452 kg with an uncertainty of about 3%. The Kevlar walls add  $0.1 \text{ g/cm}^2$ , for a total mass of 2.5 kg. The water target chemical composition by mass is 88.5% O and 11.1% H with negligible amounts of C and N.

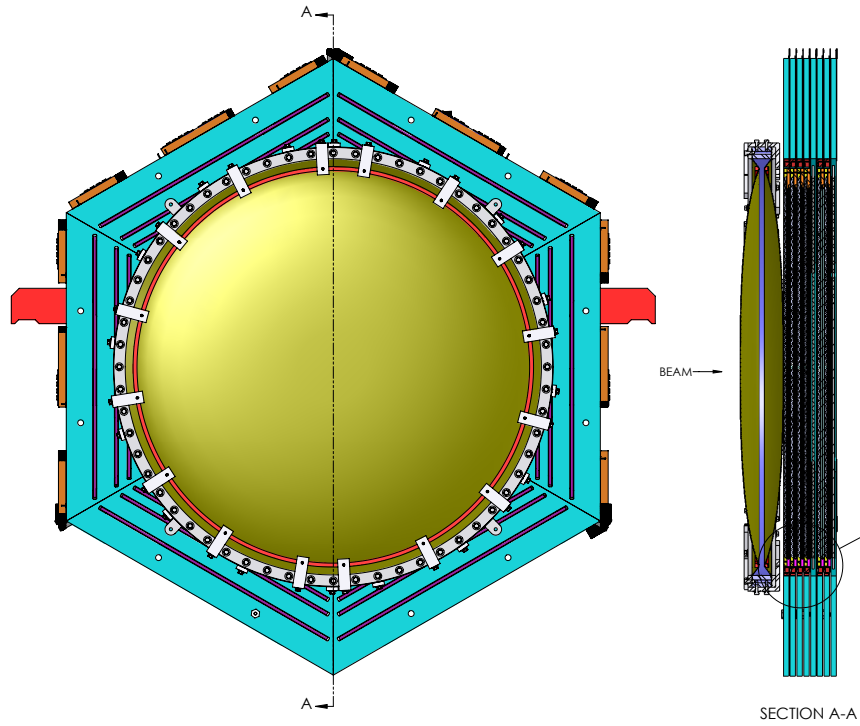


Figure 5: Schematic drawing of the MINERvA water target, showing a front view and side view of the center section.

### 2.5. Liquid Helium Target

The MINERvA cryogenic helium target is located immediately upstream of the active detector and was filled with liquid helium during the latter parts of the run. Its design

reflects the following considerations: the largest volume possible for increased statistics; a minimum of material to be traversed in reaching the tracking detectors by particles originating from interactions in the helium; the largest acceptance possible for neutrino events scattering off helium; and an acceptable level of backgrounds produced from the containment vessels and support structures. The cryogenic target consists of an aluminum cryostat capable of holding approximately 2300 l of cryogen. The cryostat consists of an inner vessel containing the cryogen, which is thermally isolated from an outer vacuum vessel, and which hangs from a set of four Kevlar ropes. The vacuum region contains layers of thin aluminum baffles for minimizing the radiative heat transfer from the inside of the outer vessel to the inner vessel. The inner vessel itself consists of a cylinder with an inner diameter of 152 cm, length of 100 cm, and a wall thickness of 0.635 cm. The ends of the inner vessel are capped with 0.635 cm thick American Society of Mechanical Engineers (ASME) flanged and dished heads, which are welded to the cylinder. The outer vessel cylinder has an inner diameter of 183 cm and a wall thickness of 0.952 cm. In order to minimize energy loss and rescattering of final state particles entering MINERvA, the amount of aluminum on the downstream end of the cryostat was minimized in the design. Consequently, the flanged and dished head on the upstream end has a thickness of 0.635 cm, while the hemispherical head on the downstream end has a nominal thickness of 0.160 cm and a radius of curvature of 107 cm with the center of curvature downstream.

The target is instrumented with the following: a set of four load cells (one on each support leg) for measuring the total weight of the cryostat; a cryogen depth gauge in the inner vessel fill tube for determining the volume of cryogen; a cryogen temperature sensor; and a pressure sensor for measuring the pressure of the vapor in thermodynamic equilibrium with the cryogen. Since the equation of state for helium is known, the temperature and pressure sensors allow an accurate determination of cryogen density. Combining the density and depth gauge measurements provides a determination of the cryogen total mass, which is complementary to the measurement from the load cells. In addition, the temperature is regulated to within 25 mK via a feedback loop which controls a heater. The

regulation of the helium density is thus estimated to better than 0.5%.

### 3. The Optical System

Light signals from the over 32,000 scintillator strips in MINERvA must be converted to electrical pulses which carry accurate timing information and have amplitudes proportional to the energies deposited. This section describes the MINERvA optical system, which begins with the light generated when charged particles pass through the individual scintillator strips. Scintillation light is collected in wavelength shifting fibers at the center of each bar and transmitted through clear optical cables to 64-anode photo-multiplier tubes (PMTs) mounted above the detector. Each PMT is housed in a metal cylindrical “box” which contains an additional set of fibers, called an optical decoder unit (ODU), to guide the light to the front face of the PMT. Each box also houses the associated PMT base. The front-end electronics board that services the PMT is mounted to the exterior of the box on one endplate.

#### 3.1. Scintillator

MINERvA uses extruded plastic scintillator technology for the tracking detectors of the ID and embedded scintillators in the OD. The blue-emitting extruded plastic scintillator strips are read out with a green wavelength shifting (WLS) fiber placed in the center of the strips. The extruded scintillator strips are made from polystyrene pellets (Dow Styron 663 W) doped with 1% (by weight) 2,5-diphenyloxazole (PPO) and 0.03% (by weight) 1,4-bis(5-phenyloxazol-2-yl) benzene (POPOP). This scintillator composition was previously utilized in the MINOS scintillator strips [6]. PPO and POPOP are used for their spectroscopic properties. The strips are co-extruded with a white reflective coating based on 15%  $\text{TiO}_2$  (by weight) in polystyrene.

The ID scintillator strips are triangular in cross-section with a height of  $17 \pm 0.5$  mm and width of  $33 \pm 0.5$  mm (Fig. 6). Each ID strip has a  $2.6 \pm 0.2$  mm diameter hole centered at  $8.5 \pm 0.25$  mm above the widest part of the triangle. Both ends of the scintillator strips are painted with white EJ-510  $\text{TiO}_2$  Eljen paint [11]. The OD scintillator strips have

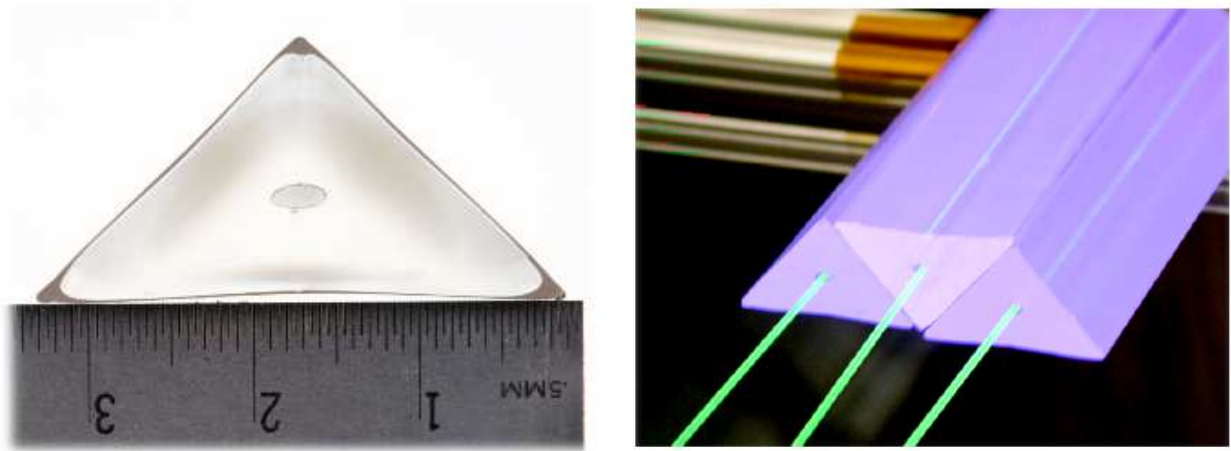


Figure 6: The MINERvA scintillator strips are triangular in cross section (left) and range from 122 cm to 245 cm in length. Planes are built by stacking the triangular strips as shown in the right figure. This configuration ensures that any charged particle traversing the plane creates a scintillation signal in a minimum of two strips.

two different rectangular cross sections. For 90% of the detector the OD scintillator strips have a base of  $19 \pm 0.5$  mm and a height of  $16.6 \pm 0.5$  mm. For the hadron calorimeter region the OD steel is thicker, hence the OD scintillator strips are also thicker to improve hermeticity. The OD scintillator strips have a  $3.5 \pm 0.2$  mm diameter hole. Both ID and OD scintillator strips were extruded in the Extrusion Line Facility at Fermilab supported by both Fermilab and the Northern Illinois Center for Accelerator and Detector Development. The extrusion equipment allows for a continuous process from the polystyrene pellets received in boxes to the final product, with little manual handling. Only the dopants and the  $\text{TiO}_2$  pellet mixture have to be periodically added to the gravimetric feeder and co-extruder hopper, respectively, which dispenses the extrusions. The extrusion line operates under a nitrogen purge from the dryer which uses high pressure nitrogen to dry the polystyrene pellets in the die.

### 3.2. Wavelength Shifting Fibers

The scintillator strips are read out by 1.2 mm diameter, 175 ppm Y-11 doped, S-35, multicladd wavelength shifting (WLS) fibers produced by the Kuraray corporation. MIN-ERvA reads out only one end of its WLS fibers. To maximize light collection, the unread end of each fiber is mirrored. This mirroring procedure consists of 3 steps: polishing the end to be mirrored using a technique called “ice-polishing” [12], then depositing a 2500 Å thick reflective coating of 99.999% pure aluminum by sputtering, and finally applying a protective layer of Red Spot UV Epoxy to the mirrors.

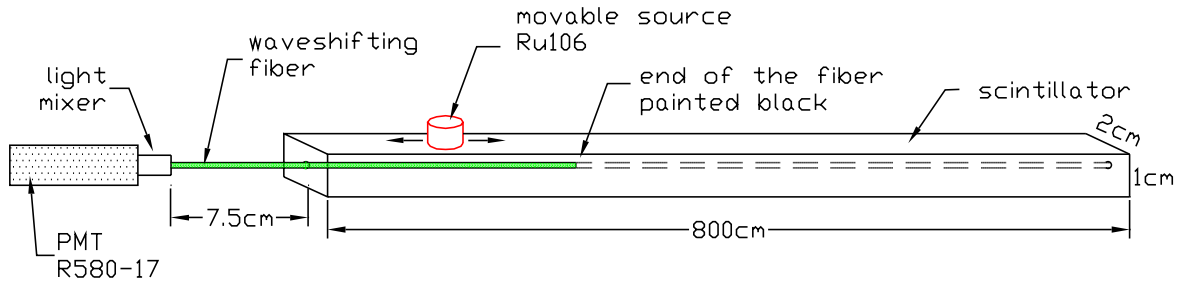


Figure 7: A schematic diagram of the scanner used to measure the attenuation length of WLS fibers.

After this process, a destructive measurement of the mirror reflectivity is made with five 2.1 m mirrored fibers from each sputtering session. The unmirrored ends are inserted into a 10 cm by 10 cm scintillator tile and illuminated with a Cs-137 source collimated by a lead cone which sits on top of the tile. The mirrored end is then cut off at 45° and painted with black paint, Model Master Flatblack 4768, and the fiber is remeasured. The reflectivity is then defined using the measured intensities in the two cases as  $R = 1 - I_{\text{black}}/I_{\text{mirror}}$ . The average mirror reflectivity is 83% with a standard deviation of 7%.

The fibers are manufactured in batches, called preforms. Five 320 cm fibers from each preform are tested using a fiber scanner, shown in Fig. 7, to determine if the attenuation is acceptable. To measure the attenuation, a fiber is inserted into the long scintillator bar and read out at one end using a R580-17 Hamamatsu PMT attached to a picoammeter for different positions of a  $^{106}\text{Ru}$  source along its length. Figure 8 shows an example of

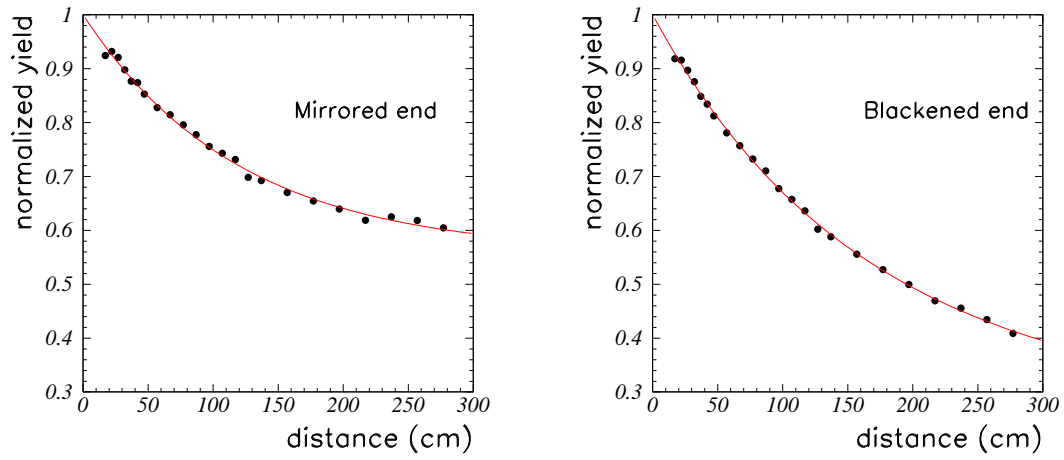


Figure 8: Two measurements of the same fiber using the WLS scanner. The fiber is first measured with the non-readout end mirrored (left). Next, the mirror is cut off, the end painted black and the fiber is remeasured (right). The fit is a double exponential function,  $p(1)e^{-x/p(2)} + p(3)e^{-x/p(4)}$ , where  $x$  is the distance to the phototube and  $p(i)$  are the fit parameters.

the same fiber being scanned when the terminated end has been mirrored versus when it has been blackened. The data are fit to a double exponential and extrapolated to 320 cm. The quality control is based on the measured attenuation length and the amount of light at 320 cm from the readout end since the longest WLS fibers in MINERvA are 320 cm. The measured attenuation varied over different batches from 0.31 to 0.37, with standard deviations varying from 0.015 to 0.033.

### 3.3. Optical Connectors and Clear Fiber Cables

The WLS fibers are terminated with optical connectors from Fujikura-DDK [13], referred to as DDK connectors. Each connector groups eight fibers. The DDK connectors are used to connect to cables containing eight clear optical fibers which transmit light from the WLS fibers to the PMT boxes above the detector. These connectors were originally developed by DDK for the plug upgrade for the CDF experiment at Fermilab [14], in consultation with Tsukuba University.

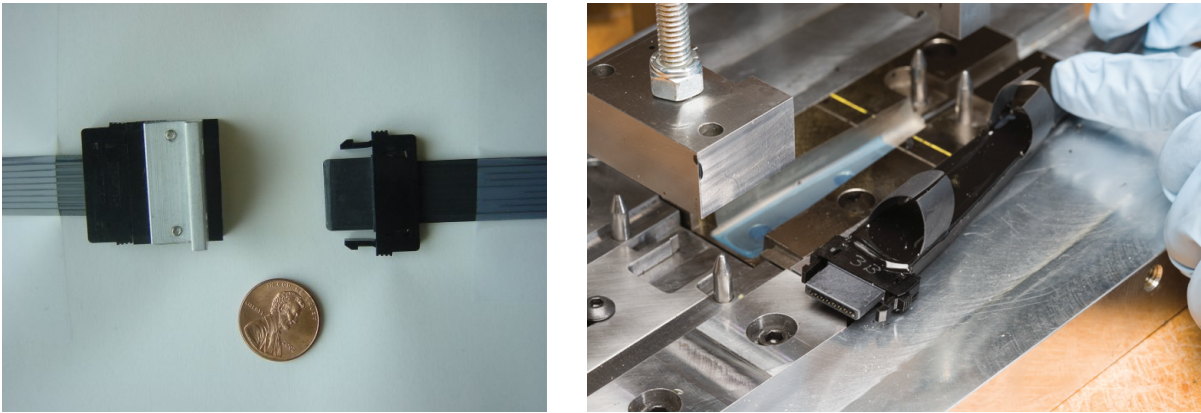


Figure 9: The DDK connector used to connect 8 WLS fibers to 8 clear optical fibers which carry signals to the PMTs mounted above the detector (left). The aluminum mold used to attach the light-tight boot to the optical cable shown in the foreground (right).

The DDK connectors consist of a ferrule, clip, and box (Fig. 9). They snap together without screws or pins. The clear optical cables are made of 1.2 mm, S-35 multicladd clear fiber from Kuraray to match the WLS fiber. Clear fibers are also used in the PMT boxes to



transmit light from the cable to the PMT via the ODU, described in Section 3.4. There are four different lengths of clear cables used in the detector depending on where the WLS bundles exit the detector: 1.08 m, 1.38 m, 3.13 m, and 6 m.

To make a clear fiber cable, the fibers are first cut to the correct length. The fibers are then inserted into a ferrule and the tops are taped against a horizontal piece of metal. BC600 epoxy is then placed in the pocket of the ferrule with a syringe. After the epoxy cures (the next day), two clips are placed on the fibers and a light-tight tube is placed over the entire length of the fibers except for approximately 5 cm near the ends where the fibers enter the ferrules. The free end of the fibers are placed in a second ferrule and epoxied in place. After curing, the fibers on both ends of the cable are trimmed to about 0.3 cm at the connector in anticipation of polishing. After the ferrules and fiber ends are polished, the clips are pushed up onto the two ferrules.

To ensure light-tightness the fibers are surrounded by a 0.6 cm thick opaque sheath of INSUL #4900/3. Figure 9 (right) shows the mold used to surround the region near the connectors with a light-tight boot. The mold is filled with custom epoxy “MP5405 bk with extra carbon black” from Heigl Technologies [15]. The boots are made fire-resistant by putting on a single coat of Performix HCF from Plasti Dip, a flexible acrylic water-based coating.

Before use in the experiment, the light transmission of each fiber in each connector is measured on a dedicated test stand. Figure 10 shows a schematic diagram of the apparatus used for this measurement. A light-emitting diode (LED) shines on the fibers in a repeatable way with normalization provided by a calibration pin diode. Each cable is connected from the LED source box to a readout box by optical jumper cables. The jumper cables help to preserve the fiber optical surfaces of both boxes by reducing the number of connections made to them. The transmission is determined by measuring the light transmission through the apparatus without the cable (the Direct Measurement), then with the cable inserted, (the Cable Measurement). The transmission is defined to be Cable Measurement/Direct Measurement. The attenuation length is determined by

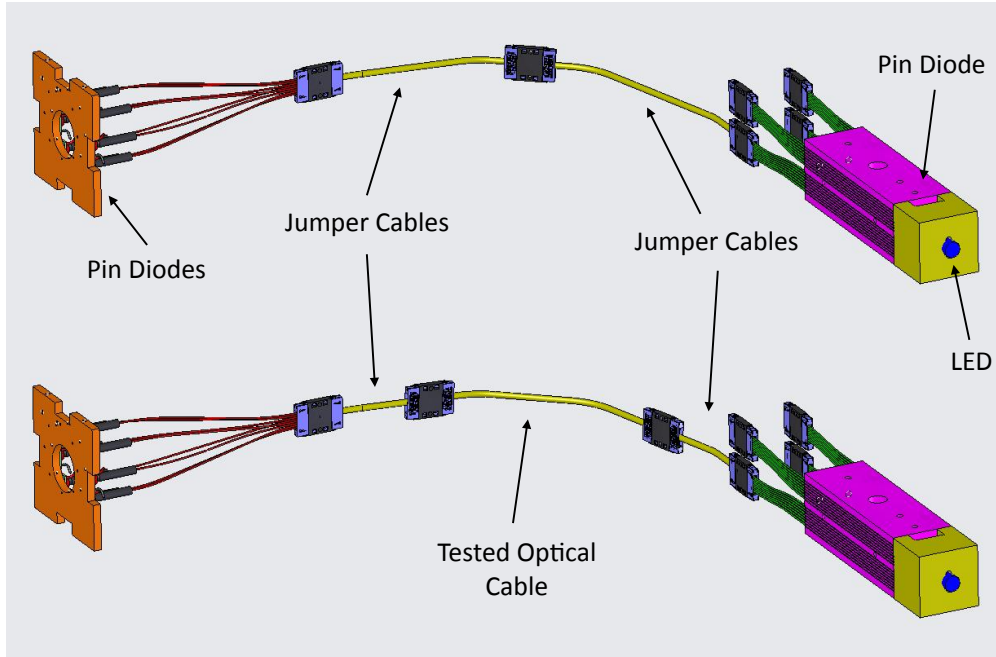


Figure 10: Schematic of the setup used to measure the transmission coefficients of the clear optical cables.

fitting the measurements from 0.5 m, 1.08 m, 1.38 m, and 3.13 m length cables to an exponential. The fit gives an attenuation length of 7.83 m for the clear fiber. The attenuation in the clear fiber can then be subtracted to determine the transmission across the connector.

Measurements of the production ODU's yield transmissions with an average value of 87.5% with a standard deviation of 3.5%. The connector transmissions averaged about 87.0% with a standard deviation of 4.8%. Fibers are visually checked for breaks or cracks, and are tested for light tightness and for correct fiber ordering at the end of the assembly.

### 3.4. Photomultiplier Tubes and Optical Boxes

The light output for a minimum ionizing particle (MIP) traversing a scintillator strip in the detector is sufficient to enable the use of a low quantum efficiency photosensor. However, a timing resolution of better than  $\sim 5$  ns is important for distinguishing overlapping events within a single spill of the NuMI beamline and for measuring time-of-flight and decay times of charged mesons created in neutrino interactions. With these considerations in mind, the multi-anode photomultiplier tube (PMT) model number H8804MOD-2

manufactured by Hamamatsu Photonics was chosen to serve as the experiment’s signal readout photosensor. It is essentially the same PMT as was used by MINOS [16].

The H8804MOD-2 PMT has an  $8 \times 8$  array of pixels laid out on a  $2 \text{ cm} \times 2 \text{ cm}$  grid, i.e. 64 pixels per PMT with each pixel having an effective size of  $2 \times 2 \text{ mm}^2$ . The general properties of the H8804MOD-2 PMT are listed in Table 5 and the operating characteristics provided by the manufacturer are given in Table 6. The PMTs for the detector are required to have a minimum quantum efficiency of 12% at 520 nm and a maximum-to-minimum pixel gain ratio less than three. A total of 507 PMTs are used in the fully instrumented detector.

Parameter	Description/Value
Spectral Response	300 – 650 nm
Peak Wavelength	420 nm
Photocathode Material	Bialkali
Photocathode Minimum Effective Area	$18 \times 18 \text{ mm}^2$
Window Material	Borosilicate Glass
Dynode Structure	Metal Channel Dynodes
Number of Stages	12
Weight	30 g
Operating Ambient Temperature	-30 – 50 °C
Average Anode Current	0.1 mA

Table 5: General properties of the Hamamatsu H8804MOD-2 multi-anode photomultiplier tube.

Each PMT is housed in an individual light-tight cylindrical enclosure made of 2.36 mm thick steel. The boxes provide mechanical protection to the PMTs, facilitate the routing of signal and voltage cables, and provide shielding from ambient magnetic fields due to the close proximity of the MINOS detector. The cylindrical housings are capped with machined steel endplates. Each endplate has a gasket and a room temperature vulcanizing (RTV) silicone seal to ensure that no light can leak in from the outside. The front-end

Parameter	Min.	Typical	Max.	Unit
Luminous (2856K) Cathode Sensitivity	60	70	-	$\mu\text{A}/\text{lm}$
Quantum Efficiency at 420 nm	-	20	-	%
Anode Dark Current	-	2	20	nA
Anode Pulse Rise Time	-	1.4	-	ns
Electron Transit Time	-	8.8	-	ns
Pulse Linearity $\pm 2\%$	-	30	-	mA

Table 6: Hamamatsu H8804MOD-2 multi-anode photomultiplier tube operating characteristics at 25° C.

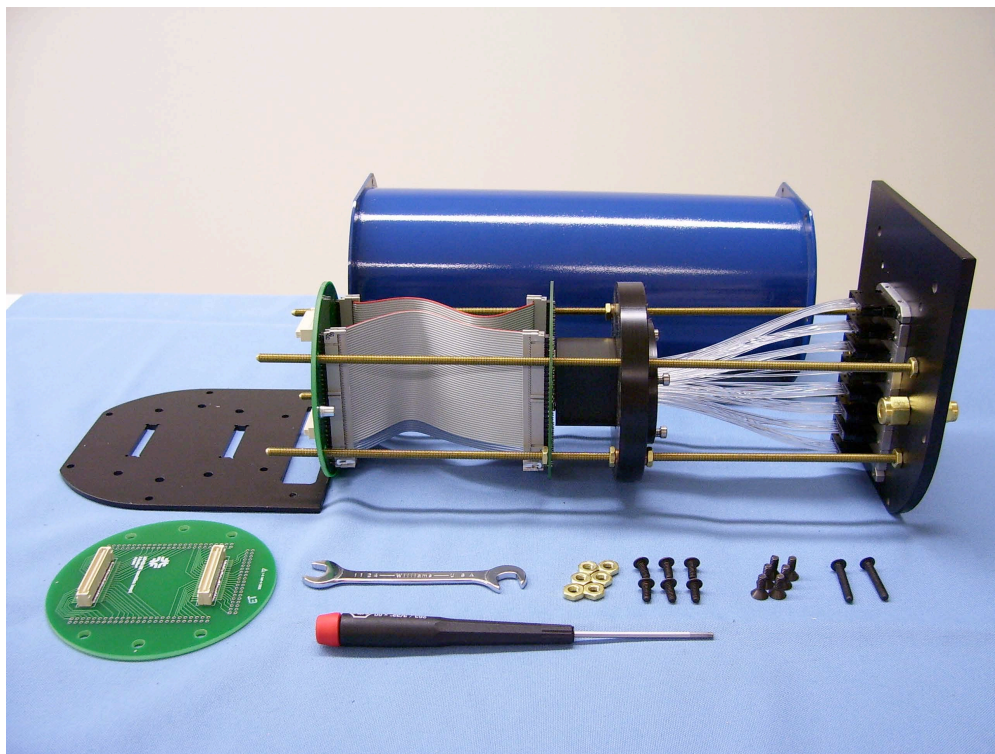


Figure 11: Optical box with interior mounting frame, prior to assembly. The frame holds the fiber cookie and PMT alignment plate within the shielding enclosure. The Optical Decoder Unit can be seen between the PMT and face plate on the right.

board (FEB) that services the PMT is mounted directly to the outside of one of the endplates to reduce input capacitance and allow easy access for connections, testing, and replacement. Within the optical box, the PMT is mounted to a base circuit board that includes a Cockcroft-Walton high voltage generator and provides signal routing to the FEB. On the other endplate is a set of eight connectors to receive clear fiber cables, which connect to the ODU inside the box. Precise alignment of individual fibers to PMT pixels is assured by routing the fibers onto a mounting “cookie.” The fiber mounting cookie together with the PMT are firmly held within a mounting holder which guarantees their relative alignment. Each box supports two additional optical fiber ports terminated by diffusers which allow all pixels of the PMT to be “flushed” in a controlled way by an external light injection system (Sec. 6.2.1). An optical box with its component parts before assembly is shown in Fig. 11.

One requirement in designing these assemblies is that light signals from physically adjacent scintillator strips in the detector do not go into physically adjacent pixels on a phototube. This is because nearest neighbor pixels are the most likely to experience signal cross-talk. The ODU uses a special weave of the optical fibers to ensure this separation, as shown in Fig. 12.

MINERvA optical boxes are deployed in the vicinity of the energizing coils and magnetized steel of the MINOS near detector. In some regions occupied by the box array, the ambient magnetic fields are typically 5–10 gauss and can be as high as 30 gauss. Because the efficiency of a PMT begins to degrade when subjected to an ambient field exceeding 5 gauss, some shielding must be provided. Several steps have been taken to reduce the field strength at the PMTs: the 2.36 mm steel provides some shielding; the boxes are oriented perpendicular to the residual magnetic field; a steel “mirror plane” has been placed between MINOS and MINERvA in the region of the return coil; and 40 of the MINERvA PMT boxes closest to MINOS have been augmented with an interior shielding of high permeability metal cylinders.

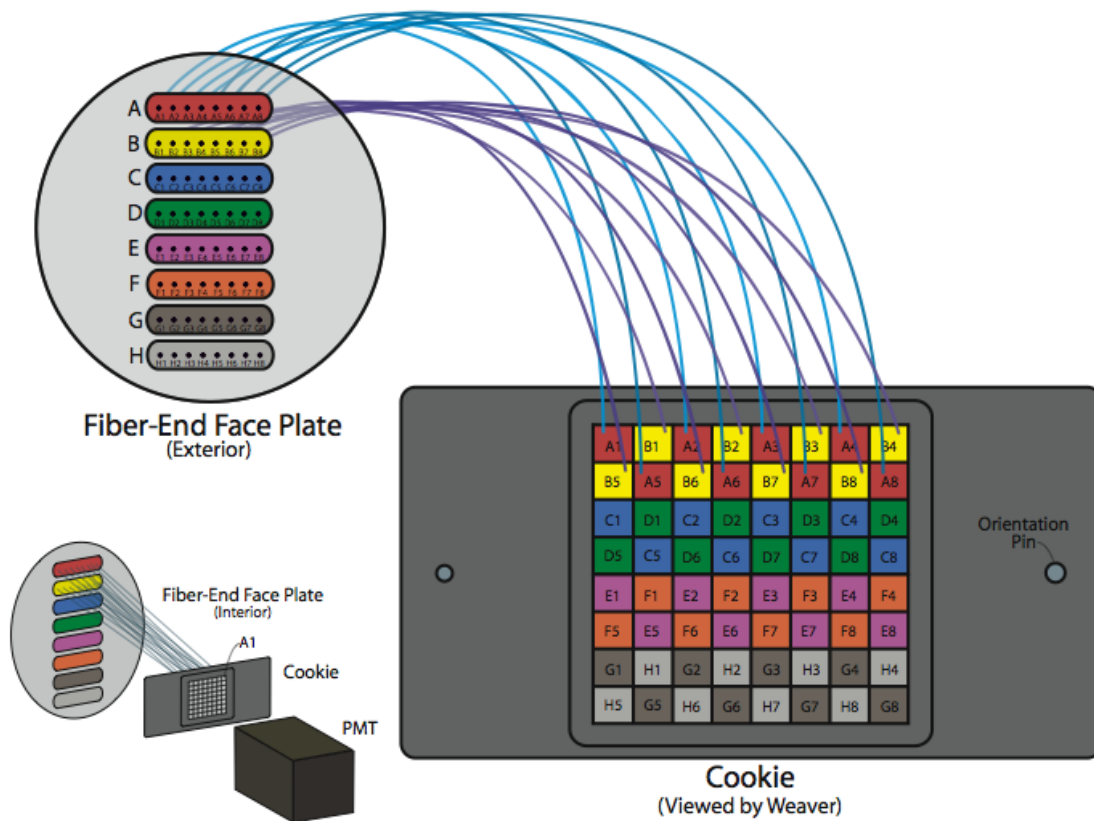


Figure 12: Diagram showing the pattern of the fiber weave within each PMT box. The weave carries light signals arriving on optical fibers going into the box fiber port to the pixel grid on the front face of the PMT. The end of each fiber of the weave is epoxied into a machined fiber cookie; the cookie is precisely aligned, via its mounting to the PMT holder, to witness marks located on the PMT pixel grid.

### 3.5. Readout Electronics and Data Acquisition

Fast analog signals from the PMTs are fed to the FEBs attached to the optical box. The FEBs digitize timing and pulse-height signals, provide high voltage for the PMTs and communicate with VME-resident readout controller modules over a Low-Voltage Differential Signaling (LVDS) token-ring. Pulse-heights and latched times over a  $16\ \mu\text{s}$  readout gate are recorded for all channels at the end of each  $10\ \mu\text{s}$  spill of the NuMI beam. The additional  $6\ \mu\text{s}$  ensure that any delayed detector activity, such as from Michel electrons from muon decays, is recorded.

The FEB design is based on the D0 TriP-t [17] Application-Specific Integrated Circuit (ASIC) which is a redesign of the readout ASIC of the fiber tracker and preshower systems of the D0 experiment at Fermilab. Each FEB services one PMT (64 channels) which requires 6 TriP-t chips per board. The TriP-t chips are controlled by a commercial Field-Programmable Gate Array (FPGA) using custom firmware. The readout chain is connected at both ends to a custom VME module called the Chain Read Out Controller (CROC), which serves up to 4 FEB chains, with each chain having up to ten FEBs. The CROCs receive timing and trigger commands from a custom module, the CROC Interface Module (CRIM). There is no hit-based trigger, but rather a timing based integration gate synchronized to the FNAL Main Injector timing signal. A full description of the MINERvA data acquisition (DAQ) system is given in Ref. [18].

## 4. Event Formation and Hit Calibration Chain

The neutrino beam is sufficiently intense to produce multiple neutrino interactions in the MINERvA detector within one  $10\ \mu\text{sec}$  beam spill. The use of a non-triggered integration-style readout system requires that individual interactions be separated offline using timing information. Figure 13 shows the hit time profile of a typical readout gate. Several isolated groupings of activity are clearly visible.

Raw time-to-digital converter (TDC) data are first corrected for propagation delays to the center of each scintillator strip. Clusters of activity in time are grouped without



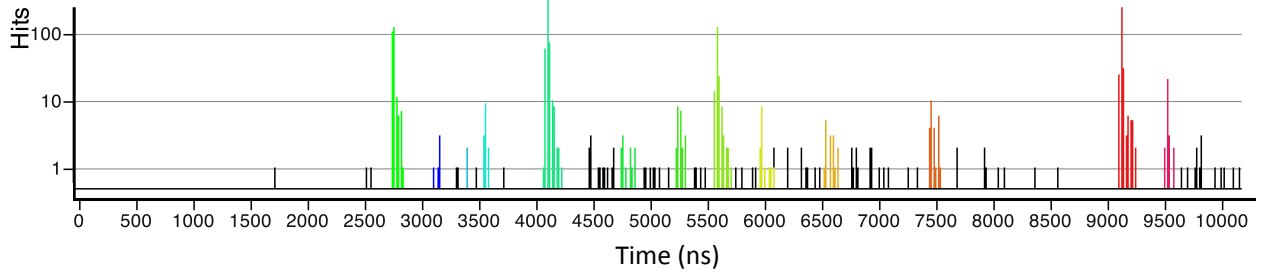


Figure 13: Time profile of PMT signals recorded in a typical readout gate (corresponding to a single  $10 \mu\text{s}$  spill of the NuMI beam). In this particular gate, 2,743 scintillator strips in the detector produce signals above the TDC discriminator threshold of about 0.7 photoelectrons. The colored groupings of hits indicate peaks found by the offline event forming algorithm. The black entries are groupings below the algorithm's threshold for forming an event.

consideration of any spatial relationships between the scintillator channels by an offline peak-finding algorithm to create “time slices”. Time slices are initiated when hits firing the discriminator within an 80 ns time window exceed a total charge threshold of 10 photoelectrons (corresponding to 2/3 of the signal over a plane for an normally-incident minimum ionizing particle). The window then slides forward until the threshold requirement is no longer met. Hits which do not fire the discriminator are then added if they share a TriP-t with a hit already in the collection. The colored peaks in Fig. 13 indicate groupings of hits made with this algorithm in one readout gate. Figure 14 shows the number of time slices per gate over a period of FHC (“neutrino mode”) and RHC (“antineutrino mode”) running at typical intensities. With the exception of electrons from the decay of stopped muons (Michel electrons), activity from a single neutrino interaction is usually contained in a single time slice. Michel electrons are identified by using spatial information to stitch together two time slices.

Raw analog-to-digital converter (ADC) data must be calibrated to provide an estimate of the energy deposited in each scintillator strip. Differences between channels as well as



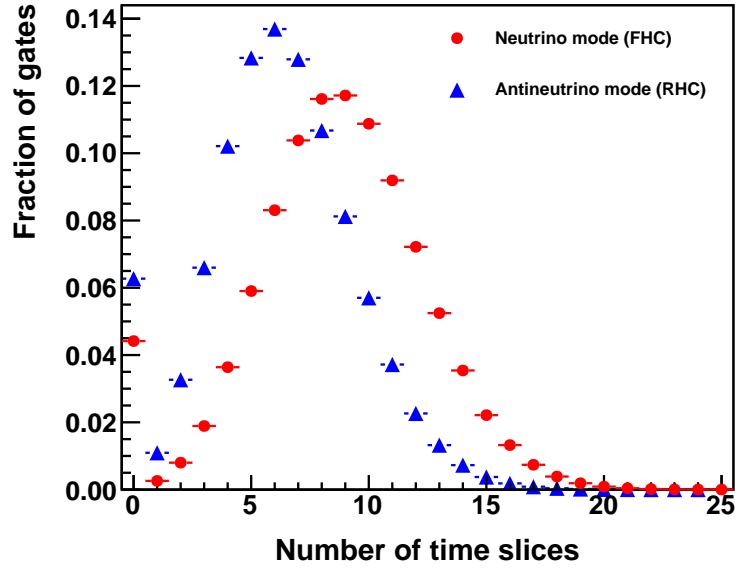


Figure 14: The number of time slices per readout gate for a period of forward horn current (neutrino mode) running from 22 March to 12 July, 2010, and reverse horn current (antineutrino mode) running from 5 November, 2010 to 24 February, 2011. The zero bin is over-populated due to occasional gates where a trigger is recorded but no protons are delivered. For these data the average protons on the NuMI target is about  $344 \times 10^{12}$  per spill.

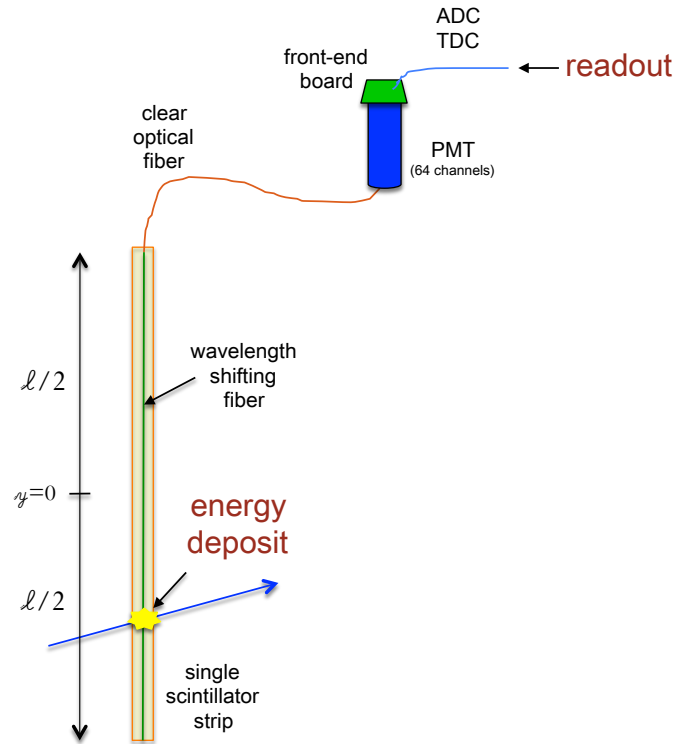


Figure 15: Schematic diagram of a single optical readout channel in MINERvA. Raw ADC counts are converted into energy through a series of calibrations that account for the various components in the chain.

variations of individual channel responses over long periods of time must be taken into account. Figure 15 shows a schematic of the components in each readout channel as described in Sec. 3. There are four effects which must be accounted for in order to convert the ADC value to an estimate of the energy deposited. (1) photons are attenuated as they travel along the wavelength shifting fiber to the end of the strip. This attenuation depends on details of the construction process for each channel and has been measured using a radioactive source on each strip in the detector prior to installation as described in Sec. 5.1. (2) The light signal is attenuated in the clear optical fibers, which have a characteristic attenuation length of 7.83 m as described in Sec. 3.3. (3) Photons reaching the PMT generate photoelectrons which are amplified in the dynode chain. The PMT gains (output charge per photoelectron) are monitored *in situ* for every channel as described in Sec. 6.2. (4) The readout charge is digitized on the FEB. The ADC conversion function was measured with a bench-top charge injection setup for every channel on every FEB before installation in the detector as described in Sec. 5.3.

Additional channel-to-channel response variations can exist due to a variety of small effects that are difficult to characterize individually. These include construction differences, the varying quality of connections between components, temperature or humidity dependence, and other effects. The relative differences between channels can be precisely monitored in real time using the high statistics sample of through-going rock muons produced upstream of the detector, as described in Sec. 6.4. The rock muon sample also provides a means for determining the absolute energy scale, as discussed in Sec. 6.5.

Each of the above effects is accounted for in the event reconstruction through multiplicative correction factors applied to the raw ADC data. The energy deposited in scintillator strip  $i$  is estimated according to

$$E_i = [C(t) \cdot S_i(t) \cdot \eta_i^{att} \cdot e^{\ell_i/\lambda_{clear}} \cdot G_i(t) \cdot Q_i(ADC)] \times ADC_i \quad (1)$$

where  $C(t)$  is the time dependent overall energy scale constant for the entire detector and  $S_i(t)$  is the relative correction factor for channel  $i$ . The correction factor for attenuation within the scintillator strip,  $\eta_i^{att}$ , comes from the point-by-point source map data described

in Section 5.1. The factor  $e^{\ell_i/\lambda_{clear}}$  is a correction for the attenuation in the clear optical fiber of length  $\ell_i$  and attenuation constant  $\lambda_{clear} = 7.83$  m. The function  $G_i(t)$  is the measured PMT pixel gain, and  $Q_i(\text{ADC})$  is the ADC-to-charge conversion factor for the FEB channel used to read out strip  $i$ .

## 5. *Ex situ* Calibrations of Optical System Components

The previous section introduced the factors that need to be applied to translate between ADC counts and energy deposited in the scintillator. Although several of those factors are measured throughout the course of the run with the operating detector, there are others which are best measured by *ex situ* measurements prior to final assembly of the detector. In Sec. 3 the measurements of the WLS fiber attenuation, reflection, and clear fiber cable transmission are described. However, the response of the scintillator strips in a full module after construction must also be measured, as well as the functionality of the PMTs and their associated electronics.

This section describes the *ex situ* measurements that are made before the detector is assembled. These measurements ensure that the components met the experimental requirements and provide several of the constants needed to reconstruct energy depositions in the detector.

### 5.1. Module Mapper

In order to translate the light output from each channel in the detector into energy deposits for further analysis, it is necessary to determine the attenuation of optical pulses as a function of position along the scintillator strip. A custom “module mapper” makes this measurement on all channels in the detector, one module at a time. The mapper also serves as the final quality check for each module before it is deployed in the detector, identifying dead channels and those having anomalous response distributions.

Corrections need to be made for optical attenuation of scintillation light in order to determine the amount of energy deposited in the scintillator by through-going charged

particles. In addition, local anomalies in the optical path (compromised WLS fiber or imperfect coupling between WLS fiber and scintillator, for example) can affect light collection. These anomalies are identified and characterized allowing appropriate corrections to be applied to physics data.

The module mapper is shown in Fig. 16. The scanner provides independent motion to two Cs-137 radioactive sources. As the sources are moved through a pre-defined scan pattern over a detector module, the scintillator response is recorded by a series of Hamamatsu M-64 PMTs interfaced to a computer running custom data-acquisition software.

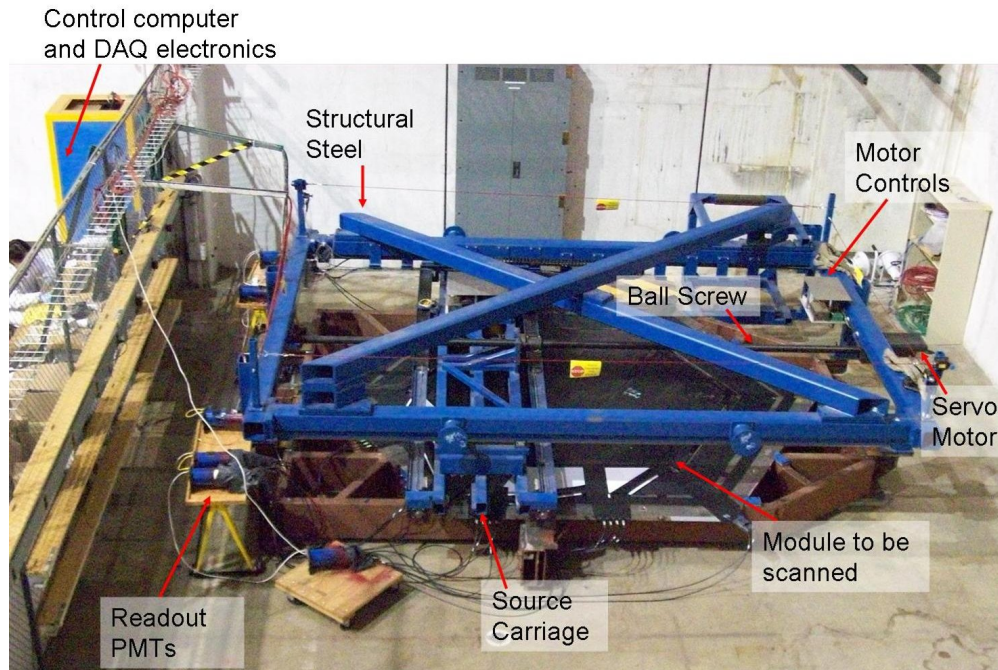


Figure 16: The module mapper uses two Cs-137 sources to characterize the optics of MINERvA detector modules. Sources were mounted on the source carriage. Ball screws controlled by servo motors provide independent motion to both sources. The scintillator response is read out by a DAQ system, and the entire scan is coordinated by the control computer.

A set of three computer-controlled servo motors coupled to ball screws move the radioactive sources through a pre-defined scan pattern. A hexagonal source location grid is optimized to minimize the total scan time while providing sufficient transverse and

longitudinal resolution for strips in both the upper and lower plane. A grid with transverse spacing of 19.05 mm in the two transverse dimensions was measured, with a total of 18,012 measurements in the inner tracking region. The outer detector scintillator was measured over a grid that had 10 mm transverse and 100 mm longitudinal spacings, corresponding to about 1100 measurements per outer detector scintillator.

The raw data stream records one ADC distribution at each source location for all channels instrumented (254 channels, for a typical two-layer tracking module). The data stream must therefore be sorted to isolate the response of a single strip for grid positions centered on that strip's coordinate system.

The mapper data analysis consists of three stages: identifying the response of each strip at each individual radioactive source position; reconstructing a transverse scan for many points perpendicular to each strip by ordering the strip response and source positions appropriately; and reconstructing the strip response as a function of longitudinal distance along the fiber. Offline analysis refinements (lead correction, layer correction) provide the final attenuation constants for the detector data calibration.

Careful tracking of the pedestal value (zero optical signal) for each channel is crucial for determining the response to the radioactive source. Due to the nature of the DAQ electronics (operated in a mode in which the mean of the ADC distribution remains constant) the pedestal value for a given electronics channel shifts to lower ADC counts when the corresponding optical channel is illuminated. This pedestal shift has been determined to be directly proportional to the current from the PMT pixel. In order to measure the pedestal shift due to the response to the source illumination of a fiber, two reference pedestals are recorded: one prior to the illumination and one after the illumination. The mean of these two source-absent pedestal locations is used as the reference point. Then the ADC distribution for this channel is recorded as the source is brought in proximity to the corresponding scintillator strip.

After the strip response is measured at a number of transverse distances from the strip at a given longitudinal position, the pedestal shift is plotted as a function of the transverse

position. This distribution is then fit to a Lorentzian profile to locate the center of the fiber position and the maximum response amplitude. Based on the source mapping program there were 15 dead channels identified (out of over 32,000) prior to installation.

After fitting many such transverse scans to obtain the maximum response as a function of longitudinal position along the strip, an attenuation response curve is determined. The response curve is used to correct for the attenuation once the position of a hit along a strip is determined by later tracking algorithms. The response curves made with the radioactive source technique are in agreement with what is measured in the data using minimum ionizing particles, but are measured to a higher precision using the radioactive source.

## 5.2. PMT Testing

Before installation in its steel enclosure, each of the 507 deployed PMTs is tested for efficiency, linearity, pixel-to-pixel gain variation, dark noise, and cross-talk prior to installation in the steel enclosure of its optical box. Figure 17 shows a schematic diagram of the light-tight test stand used to collect these data. Six PMTs are mounted onto cookies on the test stand. Each cookie connects to one of the endpoints of 64 clear optical fibers, such that the center of each pixel is above the center of a fiber. The other ends of the fibers connected to the same pixel on each PMT are bundled together; for example, the six fibers attached to each PMT's pixel two are grouped. A blue LED beams light into one end of a green wavelength-shifting fiber, while the other end of the fiber is attached to a four-axis motion control system so it can be used to illuminate one bundle of pixels at a time. Thus the WLS fiber is used to illuminate the same pixel on all PMTs simultaneously. The fourth axis of the motion control sets the amount of light filtered from the WLS fiber, and uses a mechanical neutral density filter.

Once the PMTs are installed in optical boxes, they are subjected to additional tests to better understand the operational properties of the entire unit. Specifically, any misalignment between the PMT and the cookie that holds the clear fibers from the ODUs could introduce additional cross-talk that would not be measured on the test setup described

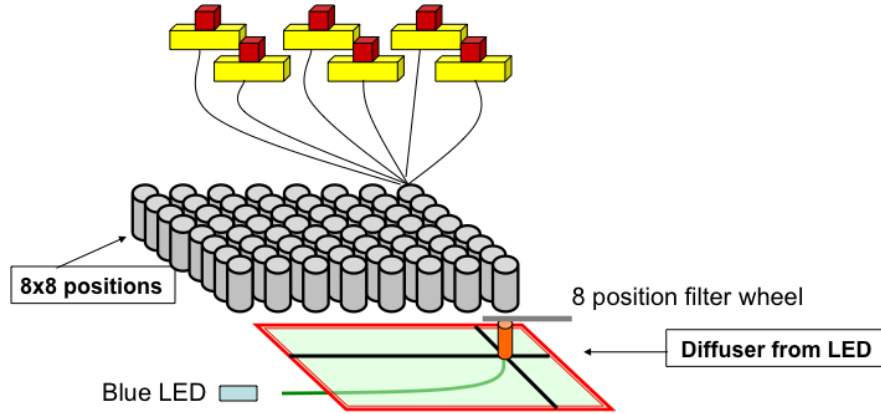


Figure 17: A schematic diagram of the PMT test stand. The motion control positions the LED beneath a bundle of six clear optical fibers, which lead to the centers of individual pixels on six PMTs. Light from the LED is collected by a green WLS fiber, which shines on a bundle of six clear fibers so that one pixel on each of the 6 PMTs is illuminated simultaneously.

above. The optical box testing uses the same light source as is used for testing the optical cables, but without the PIN diode readout. The test setup additionally uses special optical cables where only one pixel in a row of pixels is illuminated. In this way, four pixels that are far from each other can be tested simultaneously for cross-talk, and PMT boxes which exhibit high cross-talk can be repaired before installation on the detector. The cross-talk used in the detector simulation is that measured using muons in an *in situ* technique (see Sec. 6.7). DA

### 5.3. FEB Response Measurements

Each PMT is read out by a 64-channel FEB which contains six (32-channel) TriP-t ASIC chips. The signal from each PMT anode segment is divided capacitively in the ratio of 1 : 4 : 12 and routed into separate TriP-t channels to provide a low, a medium, and a high gain response to the same input charge, thereby increasing the dynamic range of the electronic circuits.

The 507 deployed FEBs were tested prior to installation in the detector. The tests included burn-in, HV control, basic input/output functionality, discriminator, digital con-



trol, charge calibration, and cross-talk measurements.

The charge calibration measurements are performed using a custom built test stand that injects a series of external charges into four selected input channels. The external charge is provided by 10 pF capacitors charged to 4 V by a pulse generator and discharged to the FEB input. The pulse from the generator is divided equally using a passive voltage divider and routed to four charge injection capacitors at the same time using remote controlled relay switches. Injecting charge to four well-separated FEB input channels is a compromise to minimize the impact of cross talk on the measurement and to maximize the number of channels tested one time.

The DAQ of the charge-calibration test stand is a replica of the MINERvA detector DAQ, consisting of a VME crate containing a CRIM and a CROC that read out the FEB being tested via Ethernet cable using the LVDS protocol. The data is passed to the DAQ via optical fiber by a PC/VME controller. The CRIM also provides the external trigger to the pulse generator for synchronous charge injection. The relay switches and the pulse generator voltage levels are controlled via a general purpose interface bus (GPIB) interface and their operation has been integrated into the DAQ software for automatic testing. A typical response of one FEB channel as a function of the input charge is shown in Fig. 18.

The response of the electronics cannot be characterized by a simple linear function of the input charge. In order to characterize the non-linearity, the high, medium, and low gain response of each channel is fitted to a tri-linear function that consists of three distinct linear segments. This simple parameterization of the response is accurate within approximately 1% over the full dynamic range. As a result, each electronics channel has three sets of six parameters (the slope and the starting point of the three linear segments) describing its high, medium, and low gain response. These parameters are stored in an offline database and used to convert the raw ADC response to linearized charge. The charge is calculated from the high, medium, or low gain response (in that order) if the corresponding digitized output is below the saturation of the electronics (approximately 2500 ADC counts).

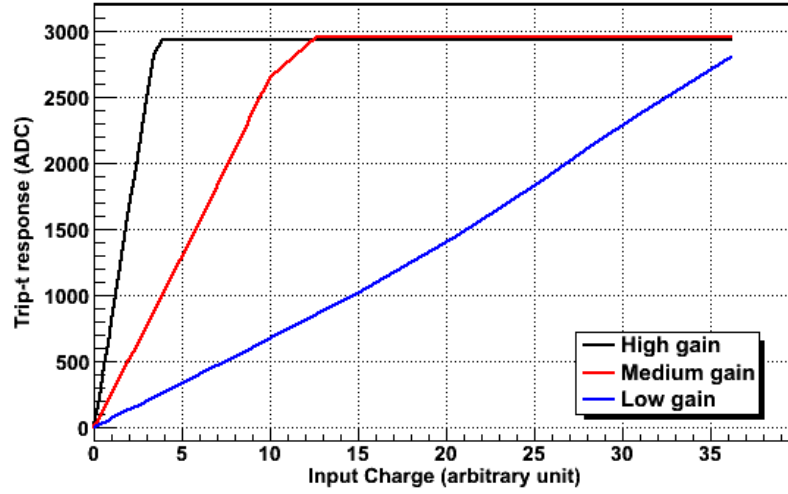


Figure 18: The digitized high, medium, and low gain response of one electronics channel as a function of input charge for a typical MINERvA front end circuit board.

## 6. *In situ* Calibrations and Monitoring

Several factors needed to convert ADC counts to an energy deposition are best measured in the assembled detector. Because these factors can vary over the course of a multi-year run, the time dependence must be accounted for in the reconstruction and the detector simulation. The rock muons generated from neutrino interactions upstream of the detector provide a natural calibration source. Through-going muons provide a standard candle to set the overall energy scale, timing calibration, and a measurement of the cross-talk between adjacent phototube pixels. They can also be used to determine the relative alignment of the ID modules and the relative light yield of each of the scintillator strips in the detector.

Some calibration factors, such as the pedestal value of each channel, are best measured in the absence of beam-induced detector activity. Other factors, such as the time-varying gain of each channel in each PMT, cannot be measured to the desired accuracy with rock muons. In order to track the gains of the PMTs (which vary at a different rate from the light yield of the scintillator), MINERvA uses a separate calibration system that injects

light into the optical boxes in between beam spills.

The following subsections describe the suite of calibration constants that are measured *in situ*, either using rock muons that occur during the beam spill, or using special calibration triggers taken between beam spills.

### 6.1. Pedestal Monitoring

Regular monitoring of detector noise during beam-absent time periods is necessary to establish the reference point, or pedestal, which needs to be subtracted from beam-on signals. During standard beam-on operation, pedestal levels are measured for all 32,448 channels during a special mixed beam/pedestal subrun that occurs once every 32 subruns, about 10.5 hours apart. This subrun collects approximately 750 gates from each channel over the course of roughly 27 minutes. Each readout gate is open for 16  $\mu\text{s}$  [18] and captures the noise from cosmic rays, radioactivity, electronic sources, and the PMTs dark current.

Background activity event displays have been hand-scanned for a sample of about 40,000 pedestal gates. A major contributor to this background is cosmic ray muons (at 18 Hz over the entire detector) penetrating the detector after passing through the 100 m rock overburden. Each cosmic ray muon event produces a single high signal during a pedestal gate for the illuminated channels. An example of a signal which is well above the normal pedestal distribution for a representative channel is shown in Fig. 19.

It is necessary to eliminate the high-side readings that occur from background particle entry into the detector and from spurious electronic signals. An outlier removal method known as Peirce's Criterion [21] is utilized to identify such pedestal readings in the raw data stream. After identification and removal of such outlying pedestal measurements, the mean and RMS pedestal is computed for each channel over the course of the subrun.

Pedestal mean values vary by about 7% across all channels, and each channel's pedestal is observed to be stable to within 2% during a pedestal subrun. A summary of the pedestal variation for the entire detector during a single pedestal subrun is given in Table 7. The number of gates per channel varies due to the removal of spurious pedestal val-

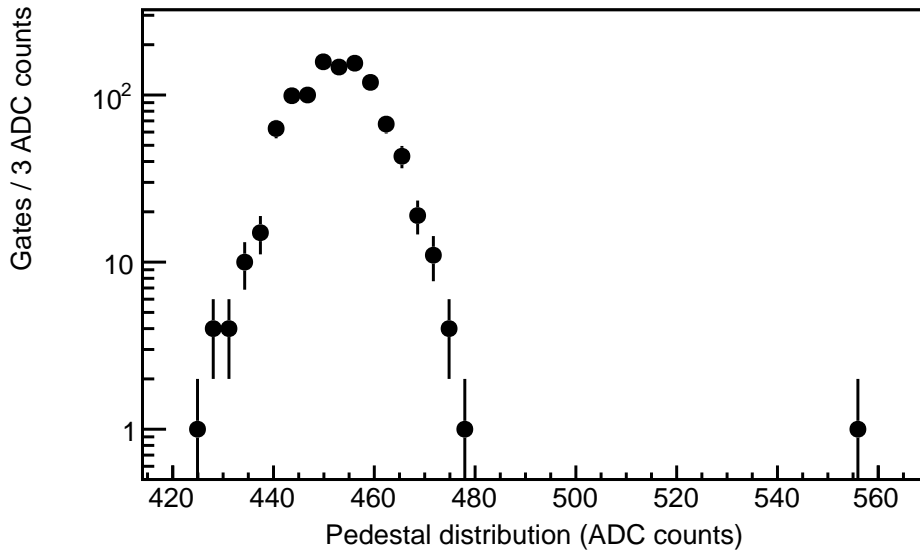


Figure 19: Example of a channel for a single pedestal gate with a measured signal of about 100 ADC counts above the pedestal level. Such gates are removed from the distribution before calculating pedestal means and widths.

ues taken during a subrun. No coherent drift of pedestal values has been observed over long time scales. The pedestal mean computed from the mixed pedestal/beam subrun is used as the reference point against which all signal levels are calculated for the 10.5 hours until the next pedestal sample is taken. The RMS of pedestal means over time is much smaller than the RMS of the pedestal values within one subrun, justifying the use of the latter as an estimate of the uncertainty on the true pedestal at the moment a beam signal is recorded.

## 6.2. PMT Gain Monitoring

MINERvA uses *in situ* calibration data to monitor fluctuations in the single PE PMT gain for each channel in the detector. The calibration source is LED light from a light injection (LI) system that is similar to that used by the MINOS experiment [22]. The LI system is triggered once after each beam spill. At this rate (0.5 Hz), enough LI data is collected

	Mean (ADC)	RMS (ADC)	Gates
High gain	$432 \pm 30$	$7.76 \pm 0.41$	$746 \pm 5$
Medium gain	$436 \pm 30$	$6.65 \pm 0.29$	$745 \pm 5$
Low gain	$440 \pm 29$	$6.36 \pm 0.27$	$746 \pm 5$

Table 7: Pedestal variation across 32576 detector channels for a representative subrun.

to measure the PMT gains across the entire detector once per day. This measurement rate is sufficient to monitor gain fluctuations, as significant gain changes tend to occur over a span of weeks.

#### 6.2.1. Light Injection System

Each optical box (Sect. 3.4) has two ports which receive clear optical fibers from the LI system. The light is spread out inside the PMT box by transmission through a polypropylene diffuser. The light reaches each of the PMT pixels through the small space between each clear fiber and its holder. Thus, the signal that reaches the PMT is small (few PEs), but uniform within a range of about 30%. This enables a rapid and accurate gain check for the entire PMT.

The core of the system is a blue AlGaInP (472 nm) LED which has a current limit of 20 mA. It is driven with a pulse generated by a custom circuit [22]. Because the pulse has a width of about 30 ns, the current can be much larger ( $\sim 200$  mA). The system has 23 LEDs. Each LED provides light to 50 clear fibers through an optical fanout, and two fibers are routed to each optical box. The optical hardware and electronics are in two boxes located 40 feet from the PMTs. The pulse amplitude, width, and timing are controlled through an RS232 interface driven by the DAQ computer.

Figure 20 shows a typical LI spectrum in one channel, where the light injection system was set to pulse at a 1 PE level. The large peak near zero is the pedestal. Subsequent peaks are too broad to be distinguished from each other.

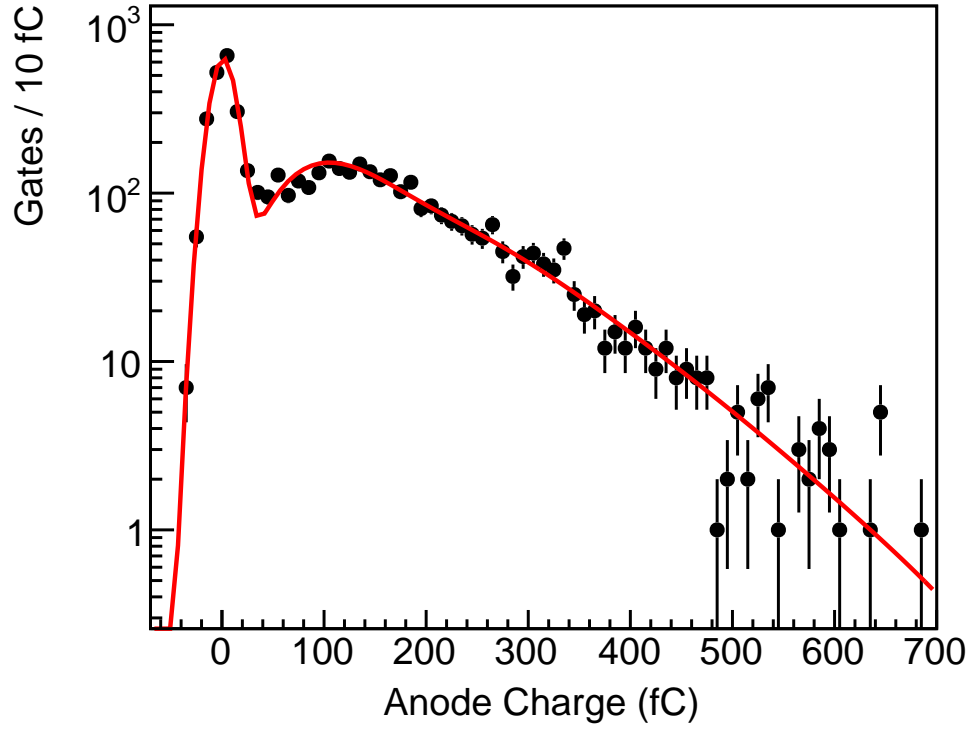


Figure 20: A typical 1 PE LI spectrum. The fit function is a simple noiseless parameterization of the PMT output.

#### 6.2.2. Gain Calculation

The PMT gain (i.e. electrons/PE count) is determined using LI data together with modeling of the photostatistics in the PMT dynode chain.

The gain  $g$  of a pixel is defined as

$$g = \frac{\overline{Q}}{\lambda e} \quad (2)$$

where  $\overline{Q}$  is the mean of the pixel's pedestal-subtracted anode charge distribution,  $\lambda$  is the mean number of PEs arriving at the first dynode, and  $e$  is the magnitude of the electron charge. Note that the quantum efficiency of the photocathode and the collection efficiency

of the first dynode are not included in this definition of the gain. Channel-to-channel differences in the latter quantities are accounted for in the relative strip-to-strip calibration (see Sec. 6.4).

For a PMT with  $n$  dynodes, the probability distribution  $P_n(q)$  of the charge  $q$  measured at the PMT anode is equal to the probability distribution of the number of PEs observed at the anode [23] convolved with a Gaussian to account for electronic noise. To good approximation each dynode amplifies according to a Poisson distribution, and the amplification is linear with the number of incoming PEs, the variance  $\sigma^2$  of  $P_n(q)$  is

$$\sigma^2 = \sigma_p^2 + \lambda g^2 e^2 + \lambda g^2 e^2 w^2. \quad (3)$$

Here  $\sigma_p$  is the electronic noise (pedestal) width and the gain  $g$  is identified as the product of the individual dynode gains  $g_i$ . The parameter  $w^2$  is defined as

$$w^2 \equiv \sum_{j=1}^n \left( \prod_{i=1}^j \frac{1}{g_i} \right). \quad (4)$$

Typically  $w^2$  has values between 0.2 and 0.3. Equation (3) states that the variance of the PMT anode charge distribution is the sum of the variance of the pedestal, the variance of the incoming PE distribution, and the variance due to the statistical broadening of the dynode chain.

By solving Eqs. (2) and (3) simultaneously, the gain  $g$  can be written as a function of  $w$  and the mean and standard deviation of the anode charge distribution:

$$g = \frac{\sigma^2 - \sigma_p^2}{\overline{Q}(1 + w^2)e}. \quad (5)$$

Equation (5) is not sufficient to calculate the pixel gains because the inclusion of  $w$  introduces  $n$  unmeasured parameters  $g_i$ . The parameter  $w$  can be expressed solely as a function of the total gain by noting that each  $g_i$  is proportional to a power of  $V_i$ , the potential difference that accelerates each PE arriving at the  $i$ th dynode

$$g_i \propto V_i^\alpha. \quad (6)$$

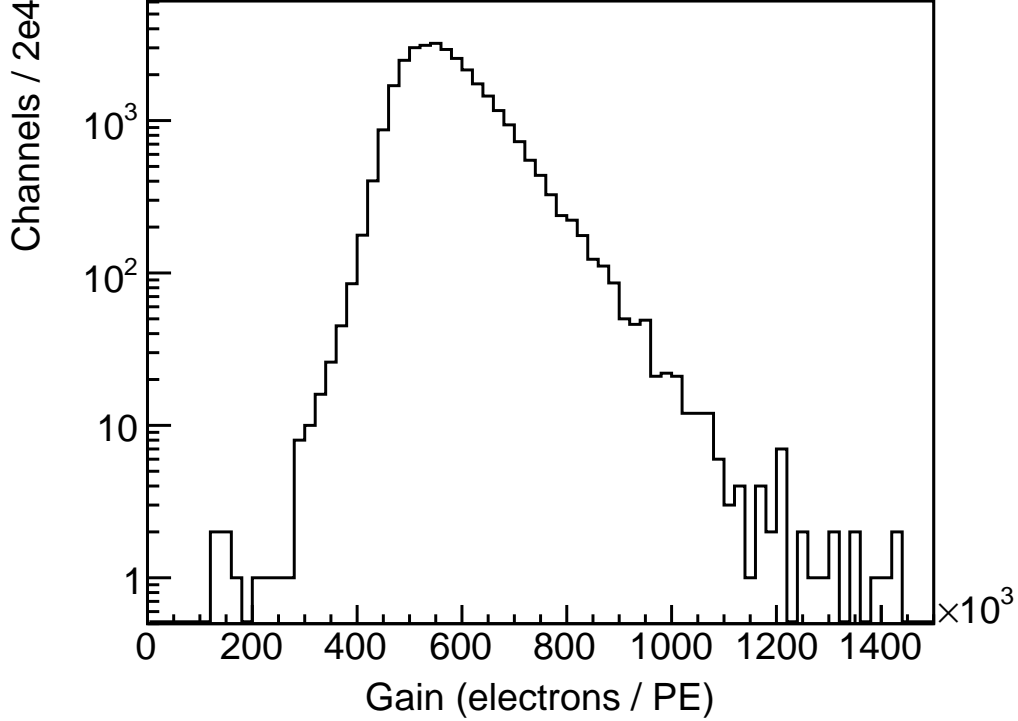


Figure 21: The measured distribution of gains of all PMT pixels in MINERvA on April 1, 2010.

The exponent  $\alpha$  typically has values between 0.7 and 0.8 [24]. MINERvA uses  $\alpha = 0.75$ , which introduces less than a 1% systematic uncertainty into the gain measurement.

The measured distribution of PMT gains in MINERvA is shown in Fig. 21. Figure 22 shows the statistical significance of gain fluctuations in consecutive measurements, demonstrating that daily fluctuations in the measured gains are mostly accounted for by the measurement's statistical uncertainty of 3% to 5%. Additionally, this gain measurement procedure is used to set the operating HV for each PMT box at the start of the data taking. The HVs are tuned such that the lowest-gain pixels have uniform gains across the detector. This is done by measuring the gain of the eight lowest-gain pixels on each tube, then adjusting the HV to give an average gain of  $4.38 \times 10^5$ .



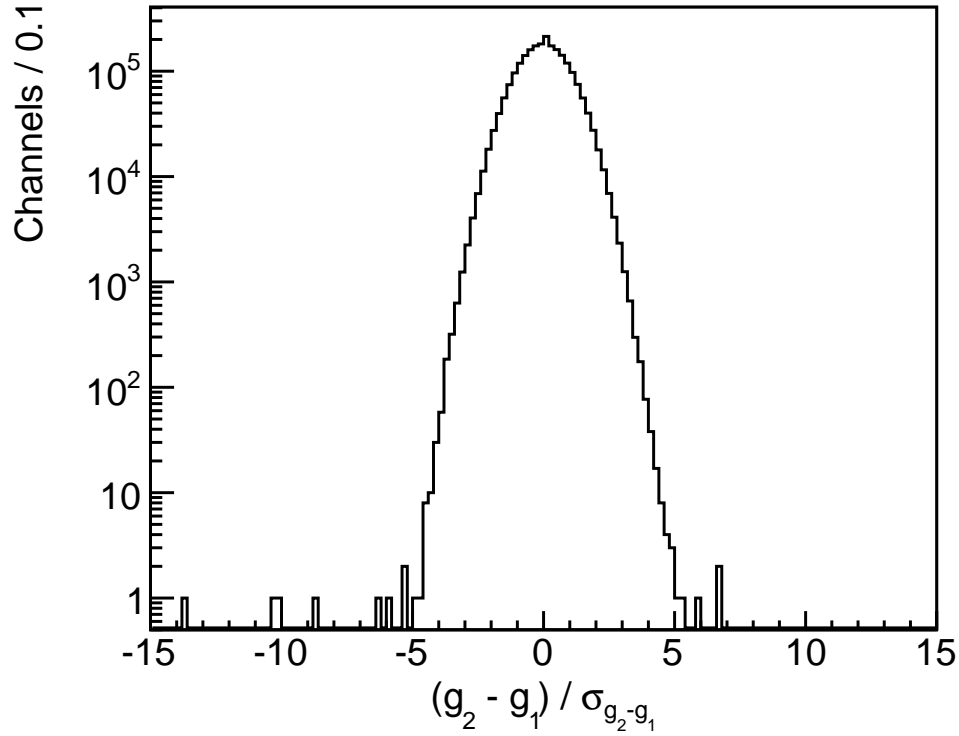


Figure 22: Statistical significance of gain fluctuations between consecutive measurements. The mean and width of the distribution are 0.002 and 0.97 respectively, indicating that gain measurement fluctuations over one day time periods are primarily statistical. The plot includes 70 gain measurements for each pixel, performed between March 1 and April 29, 2012. A total of 102 dead and underperforming channels were removed out of the 32,448 channels in the detector.

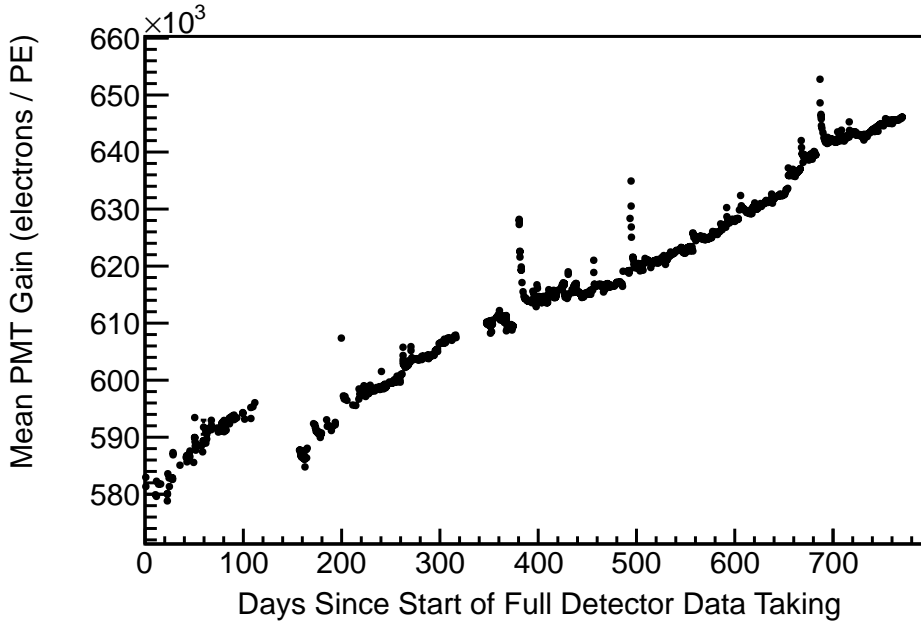


Figure 23: Average PMT gain vs. time. The nominal HVs were adjusted between days 120 and 160, causing a decrease in the mean gain. The gradual increase in gain over time is due to aging; the nature of the aging is dependent upon operating conditions and initial conditioning. The sharp peaks, e.g. day 380, correspond to times when the HV was turned off and on again. The gains typically stabilize within 24 hours after HV is re-applied.

The results of the HV tuning procedure can be seen in Fig. 21, as this data was collected shortly after the tuned target HVs were applied. The gains vary over the two years of data collection as shown in Fig. 23.

### 6.3. Scintillator Plane Alignment

The active MINERvA detector is built of 120 mechanically-independent modules, hung in series upon a rack. Small variations in the relative module positions are inevitable. The tracking and electromagnetic calorimeter modules have two active scintillator planes while the hadronic calorimeter modules have only one. Co-modular planes, although sharing support from one steel frame, can be perturbed independently by stresses and strain within the frame and manufacturing tolerances. Typical offsets are comparable to

or less than the strip widths of 33 mm. These offsets are determined by an alignment procedure and corrected for in event reconstruction.

The plane-based alignment procedure treats the 127 individual strips in a plane as a rigid unit. The first-order effect is an offset in the coordinate that corresponds to the direction of measurement in that plane. This can be expressed as a translation in the direction of the measurement. In addition to the translational parameter, a parameter for rotation about the  $z$ -axis is also introduced. Rotations are found to be on the order of a few milliradians. The translation and rotation parameters characterize the plane alignment model completely. This alignment is not sensitive to the component perpendicular to the measurement direction or to other degrees of freedom of the plane, such as rotation about the  $y$ -axis. The shift is measured by comparing the energy deposited by tracks of through-going rock muons up to their points of intersection with the 33 mm base of the strip.

The energy is corrected for normal incidence such that the maximum occurs at the strip center where the muon path length is greatest. The average energy in bins of triangle base position is fitted to the shape of the strip as shown in Fig. 24; the shift parameter is the peak of the fit. This procedure is performed in 6 bins along the strip. The shift is then plotted as a function of longitudinal position and the rotation parameter is extracted from the slope. One iteration of this procedure is sufficient to align all the planes. The residual alignment parameter uncertainties are  $< 1$  mm and  $< 1$  mrad. No further reduction in residuals is obtained if a second iteration of alignment is performed.

#### *6.4. Relative Strip-to-Strip Response Variations*

Variations in light level between ID strips can be caused, for example, by differences in the composition of batches of scintillator, by air bubbles in the epoxy used to fill the fiber hole, or by couplings between the optical fibers and photomultiplier tube. These variations are corrected by applying a multiplicative constant to strip energy deposits so that the response is uniform throughout the detector. The constants are determined from the path length-normalized peak energy deposited by through-going rock muons. The

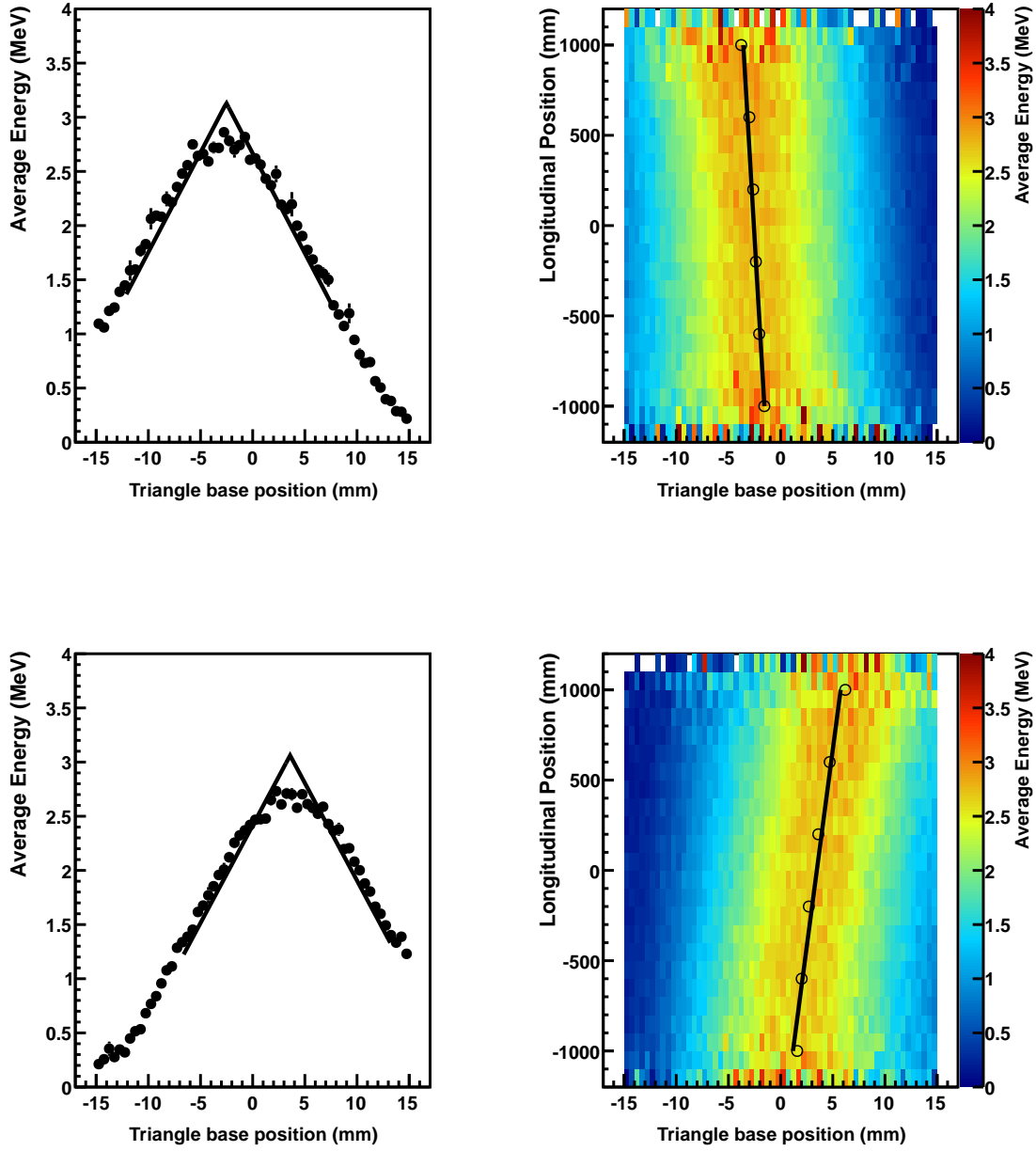


Figure 24: The alignment fits for module 50, plane 2 (top) and module 61, plane 1 (bottom). At left, the average energy as a function of triangle base position is fitted to yield the shift parameter. The rounded tip is due to the fiber hole in the scintillator. At right, the rotation parameter is determined from the dependence of the shift on longitudinal position.

calibration consists of three stages. Initially, an iteration of strip-by-strip corrections is generated using the truncated mean energy [25]. Secondly, dead channels are identified and a second iteration of strip-by-strip corrections is produced. Finally, the peak energy is equalized plane by plane. The constant for each strip is the product of the output of each iteration, normalized so that the average constant is 1.0 over the entire inner detector.

The calibration is performed in time intervals such that every strip is intersected by at least several hundred rock muon tracks in a given period. This imposes a requirement of hundreds of thousands of rock muons for adequate statistics. The boundaries of the intervals are defined by hardware changes in the detector, such as when a front end board or PMT is replaced. The energy spectrum of the incident rock muons is not measured. However, the peak energy loss per unit path length for a minimum ionizing particle is known to be a slowly varying function of the energy of the particle. Fitting for the peak requires higher statistics than can be obtained for each strip in a single interval, so this is done only on a plane-by-plane basis. For the strip-to-strip correction, the truncated mean is used as a proxy for the peak.

Differences in the relationship between the truncated mean and the peak could arise due to differences in the shape of the energy distributions between channels. Scintillator aging and absorber effects are expected to be among the leading causes of such shape differences. Scintillator within a plane was manufactured and installed at the same time, so aging effects might exist between planes but are uniform across strips within a plane. Absorber effects are uniform across a plane in the downstream calorimeters.

Non-uniform absorbers exist in the upstream nuclear target region and in the side ECAL. This could introduce differences in the shape of the response within a plane. The size of this difference is estimated by comparing the size of the fitted peak correction of Eq. (8) between the central tracking region and downstream ECAL region. This correction is essentially the amount by which the truncated mean overestimates the peak; it is 1.6% higher on average in the ECAL than in the tracking region. A similar difference might exist in the side ECAL but is not taken into account. The truncated mean is computed

iteratively. The mean for the first iteration is the full mean of events from 0 to 20 MeV per centimeter path length. In each successive iteration, the mean is calculated using events that fall between 50% and 150% of the mean from the previous iteration. Eight iterations are used; however the procedure typically converges within four iterations.

Events for which there is reconstructed path length but with null energy are counted separately. A channel is considered dead when zero-energy tracks represent more than 30% of all events. In addition to removing dead channels in which the zero-energy percentage is near 100%, this cut also eliminates extremely low-light channels where the expected number of photoelectrons from a minimum-ionizing hit has a high Poisson probability of fluctuating to zero. This effectively places an upper bound on the correction constant at about 5.0. Any strip that would require a correction larger than this is treated as a dead channel and ignored by the reconstruction in both data and simulation. It is also required that the RMS of the energy in a strip not exceed four times the truncated mean. This cut addresses rare channels where the energy response changes dramatically over a calibration interval.

The constant  $C_i$  for strip  $i$  is

$$C_i = \frac{\frac{1}{x_i}}{\frac{1}{N} \sum_j \frac{1}{x_j}} \quad (7)$$

where  $x_i$  is the truncated mean energy in strip  $i$ , and  $N$  is the number of good channels in the inner detector. The sum in the denominator is over all good channels, indexed by  $j$ . This definition guarantees that the average constant is 1.0, so that application of the constants will correct for strip-to-strip energy differences without affecting the overall energy scale.

The fitted peak correction is performed only after data is processed with the first iteration of strip-to-strip constants based on the truncated mean. This ensures that the energy distribution in a plane is not due to large variations between constituent strips.

The correction factor  $C^j$  for plane  $j$  is

$$C^j = \frac{\frac{E^j}{p^j}}{\frac{1}{n} \sum_k \frac{E^k}{p^k}} \quad (8)$$

where  $E^j$  is the truncated mean energy averaged over a plane,  $p^j$  is the fitted peak energy for a plane,  $n$  is the number of planes, and the sum in the denominator is over planes. The applied strip-to-strip constant is the product of the constant from Eq. (7) for two iterations and the plane-to-plane constant from Eq. (8).

After applying the calibrations, the plane-to-plane peak energy is roughly uniform over the modules, as shown in Fig. 25. Non-statistical fluctuations, such as in the ECAL region from module 85 to 95, could be reduced by further iterations of fitting but are already approximately the size of the fit uncertainty after one iteration.

#### 6.5. Absolute Energy Scale Determination Using Minimum Ionizing Particles

The absolute energy scale of MINERvA is calibrated using the well understood muon energy loss in the active scintillator. The absolute energy scale is described in terms of a “muon equivalent unit” (MEU factor) of energy deposited in a plane of scintillator. This factor converts attenuation and strip corrected number of photoelectrons to an energy. The MEU factor is tuned using clusters of energy depositions (cluster energies) from rock muon tracks in data and the simulation. Details of cluster energy formation are presented in Sec. 7.1.

The data sample consists of rock muons whose track in MINERvA has a matching track in MINOS. The muon momentum at its entrance point to MINERvA is estimated by correcting the MINOS momentum reconstructed by range or curvature for energy loss in MINERvA. The reconstructed position and momentum vector is used as input to a data-driven simulation sample.

The data are first analyzed with a trial MEU factor. The reconstructed cluster energy is the product of the attenuation and strip response-corrected PE and the trial MEU factor.

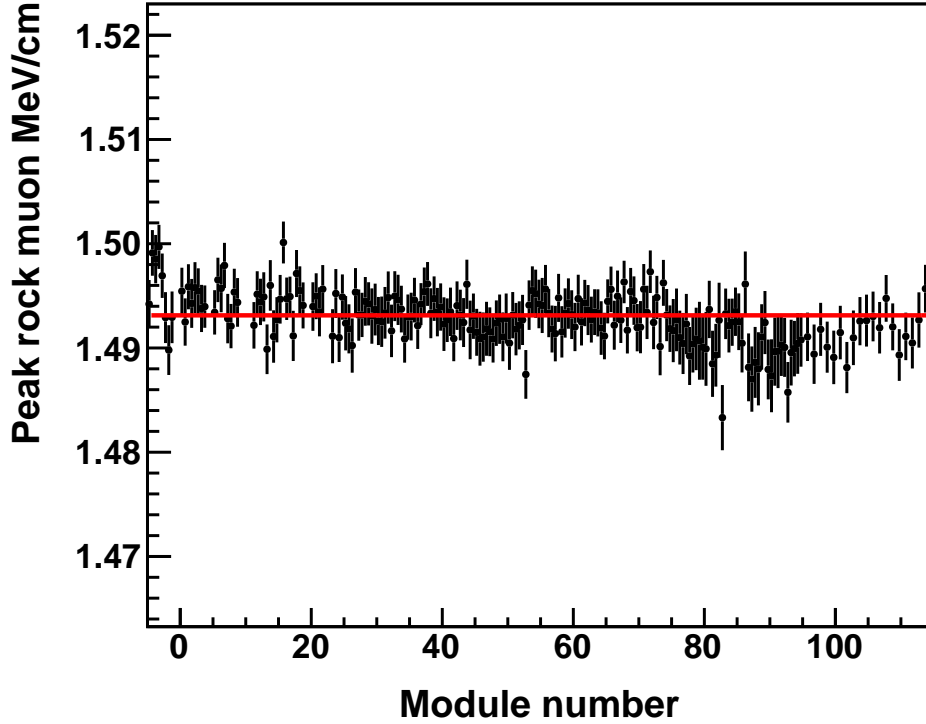


Figure 25: The peak energy per unit path length is fitted for each plane. The resulting peaks, with uncertainties from the fit, are fitted to a linear distribution with zero slope since the plane-to-plane energy is expected to be flat.

The peak reconstructed cluster energy in data and simulation (Fig. 26) is determined by fitting the region of the distribution above half-height with a fifth-order polynomial. Separately, the reconstructed cluster energy in the simulation is compared to the true energy. The true cluster energy is the total energy in the active scintillator of the strips composing the cluster, according to the GEANT simulation. The reconstructed and true peaks are fit to a straight line as shown in Fig. 27. The dominant uncertainty in the energy scale is due to uncertainty in the per plane thickness of the active scintillator. Given the uncertainties in the material assay described in Sec. 2.1, the MEU uncertainty is 2%.



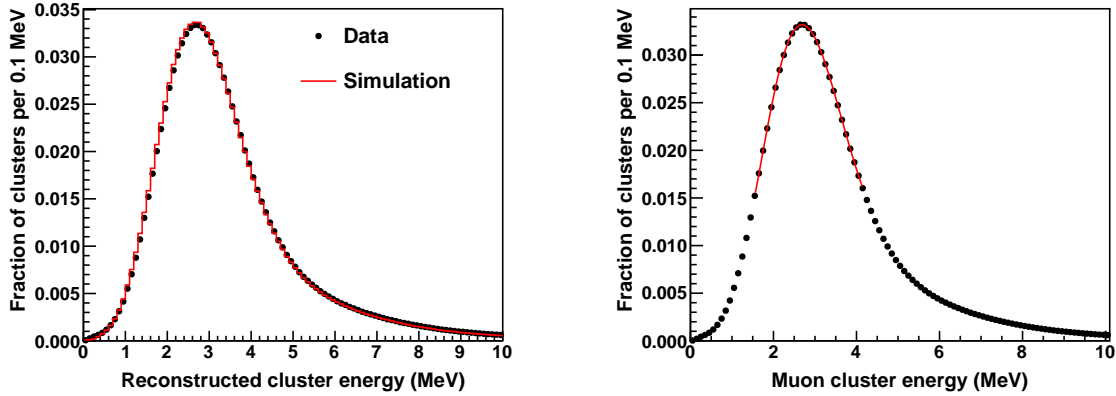


Figure 26: The energy distribution of clusters along a muon track in data and the simulation (left) and the resulting fit to the peak of the data distribution (right).

The trial MEU factor is corrected by the ratio of simulated to data reconstructed energy and by the slope of the simulated reconstructed to simulated true energy to give the final MEU factor. The tuning uses the peak reconstructed cluster energy to minimize absorber effects and muon energy loss. Absorber effects, particularly delta ray propagation and absorption, vary by subdetector due to the passive materials. Delta rays contribute primarily to the high-side tail of the cluster energy distribution, and sampling the peak minimizes this contribution.

Reconstructed cluster energy in the simulation includes simulated detector effects that smear true cluster energy. Detector smearing shifts the peak of the true cluster energy distribution while preserving the mean. It gives the correct absolute energy scale by correcting the reconstructed cluster energy mean from the simulation to the true cluster energy mean using the slope of reconstructed versus true cluster energy in the simulation.

The light output of the scintillator is found to vary with time due to scintillator aging and environmental conditions of the detector hall. Figure 28 shows the peak cluster PE as a function of time in the rock muon sample over the full detector LE data set. Around day 600 a new cooling system was installed in the detector hall; subsequently the ambient temperature was reduced by about  $6^{\circ}$  C. A modest improvement in the peak cluster PE is

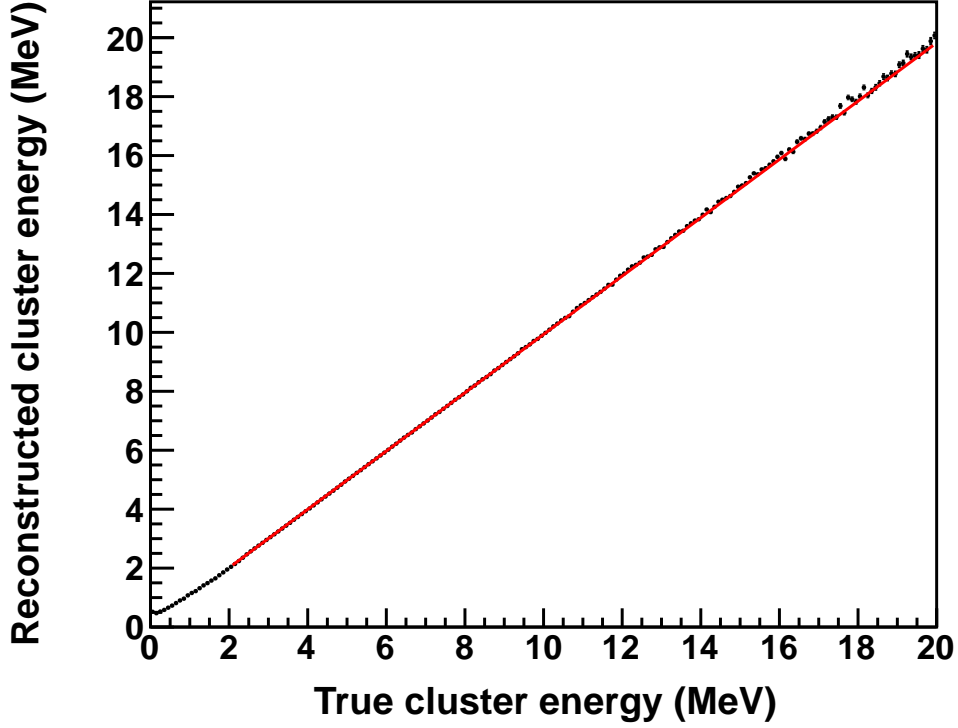


Figure 27: Plot of the reconstructed cluster energy as a function of the generated cluster energy in the simulation, and the resulting linear fit.

indicated by the light level evolution around that time, as displayed in Fig. 28. Time variation of the light output is accounted for in the absolute energy scale by dividing the data set into two-day intervals and tuning a MEU factor for each interval. The resulting peak-calibrated reconstructed cluster energy as a function of time for rock muons in data over the full detector LE data set is constant.

#### 6.6. Timing Calibration

A timing calibration is performed to correct for transport time in the optical fiber, time slewing, and channel-to-channel time offsets. Time slewing is due primarily to the scintillator decay times and is a function of the PE yield within a scintillator strip.

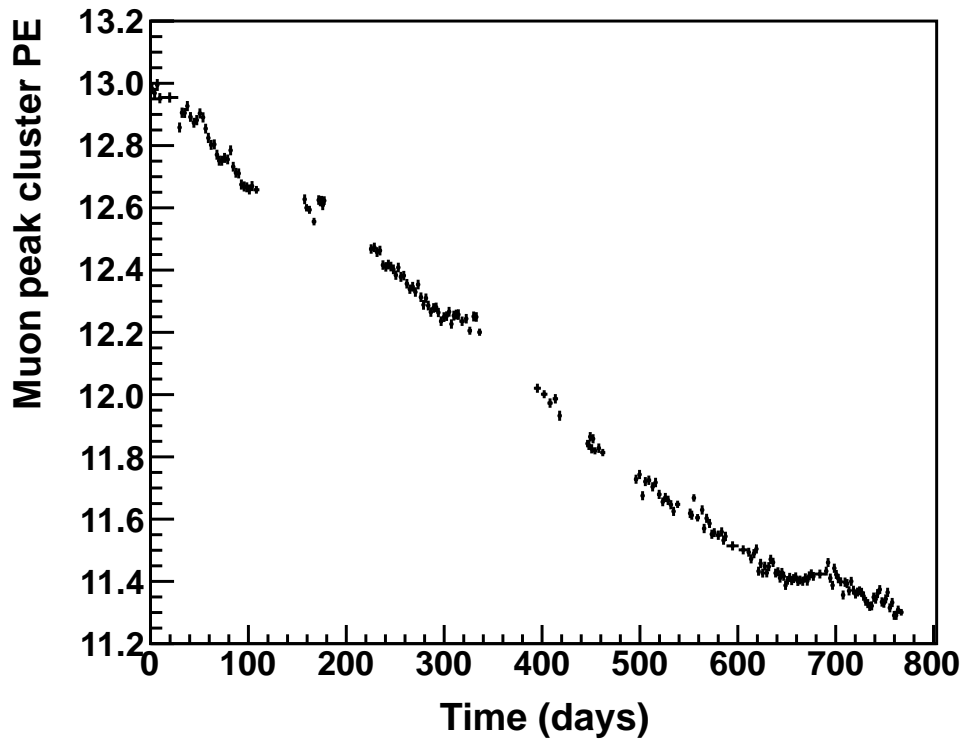


Figure 28: Light level in the MINERvA detector as a function of time, as demonstrated by the number of PE in the peak of the muon cluster distribution.

to-channel time offsets include cable delays between FEBs along a chain and time offsets between chains. The time offsets between channels on the same FEB are negligible.

Time slewing and the channel-to-channel offsets are measured in an iterative procedure using hit time and PE from identified rock muon tracks. They are measured relative to the truncated mean hit time along the rock muon track, which is corrected for muon time-of-flight, transport time in the optical fiber, and time-slewing and channel-to-channel offsets measured in the previous iteration. Transport time in the optical fiber is corrected using the fiber length and the speed of light in the fiber. The measured time slewing as a function number of PE in a single strip ("hit PE") (Fig. 29) is parameterized by a third order polynomial in  $1/\sqrt{\text{hit PE}}$ , which is used to correct for time slewing in data.

One time offset is measured for each group of channels read out by the same high-gain TriP-t chip. This accounts for channels that have low statistics and takes advantage of the small time offsets between channels on the same FEB. The time offset between channels on different FEBs is observed to be as large as 30 ns. Since hardware swaps change the channel-to-channel time offsets, the timing calibration is performed after each hardware swap.

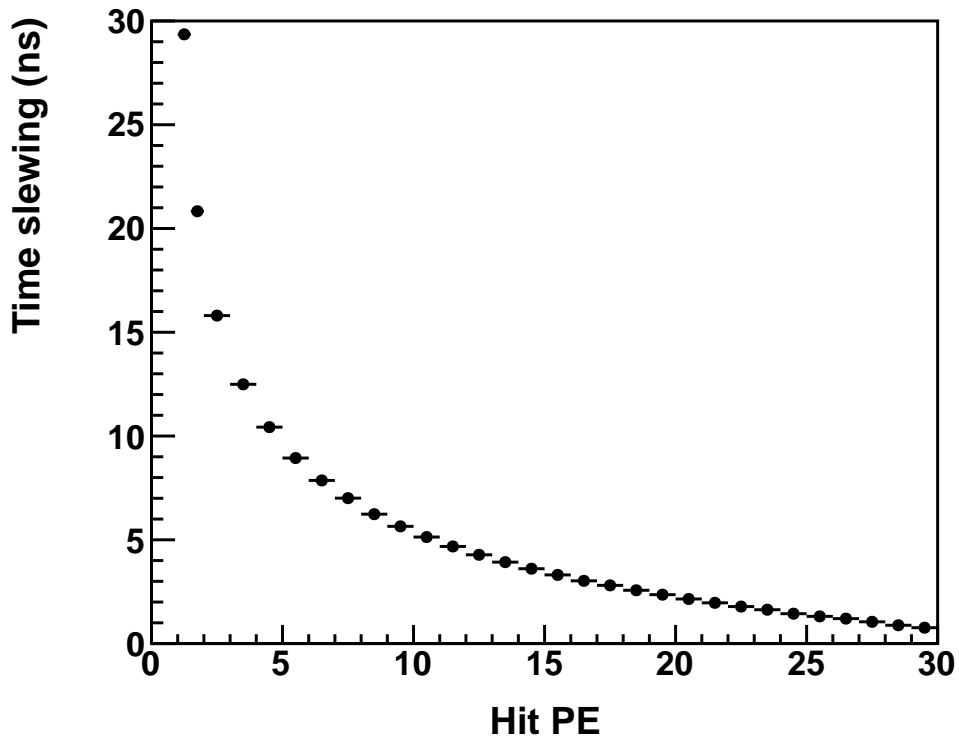


Figure 29: Measured time slewing vs. hit PE along rock muon tracks.

The calibrated time resolution is determined from calibrated hit times along rock muon tracks. Figure 30 shows the calibrated hit time along rock muon tracks relative to the truncated-mean calibrated hit time of the track. A Gaussian fit to the region above half-height gives a width of 3.0 ns. The tails are asymmetric, especially for low pulse-height hits. This is because hit times are set by the first photon to liberate a photoelectron.

Low pulse-height hits with a small number of scintillation photons can fluctuate at late times due to scintillator decay times. This effect becomes insignificant at higher pulse heights where there are many scintillation photons.

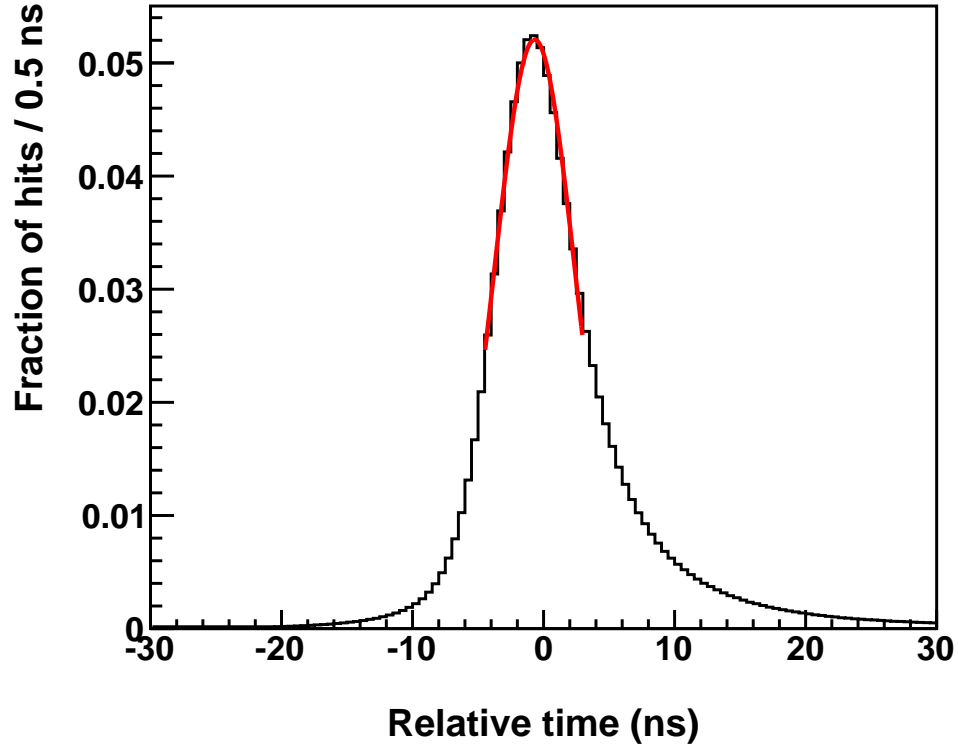


Figure 30: Calibrated hit time along rock muon tracks relative to the truncated-mean calibrated hit time along the track.

### 6.7. Cross-talk Measurements

A number of processes can cause light incident on one PMT channel to produce a signal in another channel. These are collectively known as “cross-talk.” While these can, in principle, be differentiated by tests on the bench, once the detector components are assembled and installed it is virtually impossible to separate them from one another with any significant confidence, particularly at large pulse-heights. As discussed in Sects. [5.2](#)

and 5.3 the dominant types of cross-talk in MINERvA are optical (fiber-to-PMT coupling) and PMT internal (dynode chain). Effects other than the readout electronics cross-talk discussed in Sect. 5.3 will be discussed here.

The ideal probe for a measurement of either type of cross-talk in the detector would be one in which individual pixels were illuminated with a well-defined light pulse. Unfortunately, once a PMT is mounted on the detector there is no system available to MINERvA that can accomplish this goal. The LI system discussed in Section 6.2.1 cannot be used because it illuminates all pixels at once. The next best option is to use data generated by neutrino interactions. For this measurement, we use the data-set from rock muons described in Section 6.5.

Hits within a rock muon’s time slice are classified as signal or noise based on whether or not they have been associated with the track by the track reconstruction software. The fiber weave described in Section 3.4 moves cross-talk hits far enough away from the track that they are not associated with it. Cross-talk hits can be further distinguished from other noise by assuming that the hit occurs in the same PMT as on-track activity, and associating each cross-talk hit to the on-track hit that is nearest to it on the PMT pixel grid. A sketch of how this process would work for a typical muon event is shown in Fig. 31.

Once hits have been identified as signal or cross-talk and the rest discarded, an average cross-talk fraction  $f_{xt}$  for the PMT is defined as the ratio of the energy of cross-talk hits to the energy of the on-track hits. Various permutations of this metric are also used, most notably the “nearest neighbor” pixel cross-talk  $f_{xt,NN}$  average for each PMT, because the strongest cross-talk is generally between nearest-neighbor pixels.

The measured values of  $f_{xt,NN}$  for PMTs currently in use in MINERvA are shown as the black points in Fig. 32. The vast majority of PMTs have total nearest-neighbor cross-talk fractions below 4%. Comparisons with the detector simulation can also be made using this method. The red curve in Fig. 32 depicts the simulation’s prediction for the optical cross-talk component only (the dominant mechanism and the sample used to tune

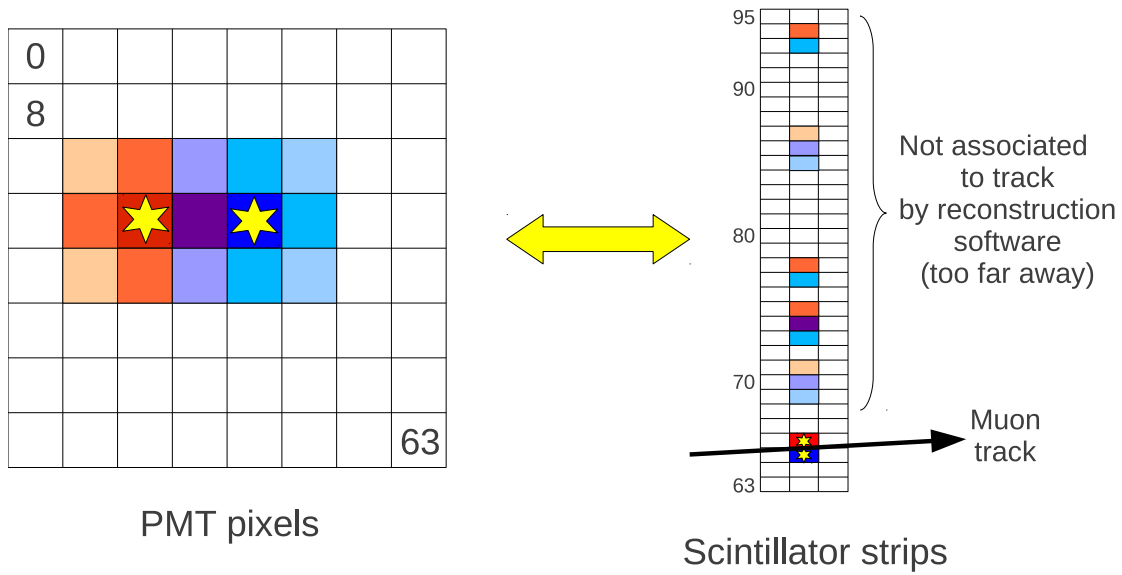


Figure 31: Schematic depiction of cross-talk on the PMT face maps to scintillator strips. The darkest blue and red (stars on the PMT diagram; strips 65 and 66 in the scintillator sketch) are the original signal from a muon track; the cross-talk energy is colored according to which original signal hit it will be associated with by the algorithm described in the text (darker means stronger cross-talk). Purple represents cross-talk that will be associated with either hit at random since it is ambiguous.

the simulation). Though the simulation implements a technique to individually scale the cross-talk for each simulated channel to that measured, agreement is modest at best. The disagreement is likely driven by individual channels in PMTs whose response deviates significantly from the underlying model used in the simulation (based on studies by MINOS [26]). Comparisons are made only in channels in the inner detector region, where the tracking software performs robustly. Channels in the outer detector are scaled using the default parameters obtained from MINOS's study.

Though the simulation's per-PMT averages do not identically match the data, the individual pulse height spectra for simulated cross-talk hits do agree. Figure 33 illustrates this: within the 1-3.5 photoelectron range (where cross-talk is most important), the difference between simulation and data is typically less than 10%. Below this range, agreement is less important in practice because the electronic discriminator threshold for nearly all

FEBs is roughly 0.8 PE. Above this range, agreement is again less essential because the Poisson probability for a resultant cross-talk hit of this pulse height is extremely low. For example, the probability of a 4 PE cross-talk hit resulting from a 100 PE hit from neutrino-induced activity, assuming the nominal 1% nearest-neighbor cross-talk leakage quoted above, is roughly 1.5%; for a 25 PE hit, the probability drops to about 0.01%. Moreover,  $\geq 100$  PE hits (corresponding to roughly 25 MeV of energy deposited in a single strip) are rare; they comprise less than 1% of usable (i.e., discriminated) hits in typical LE data.

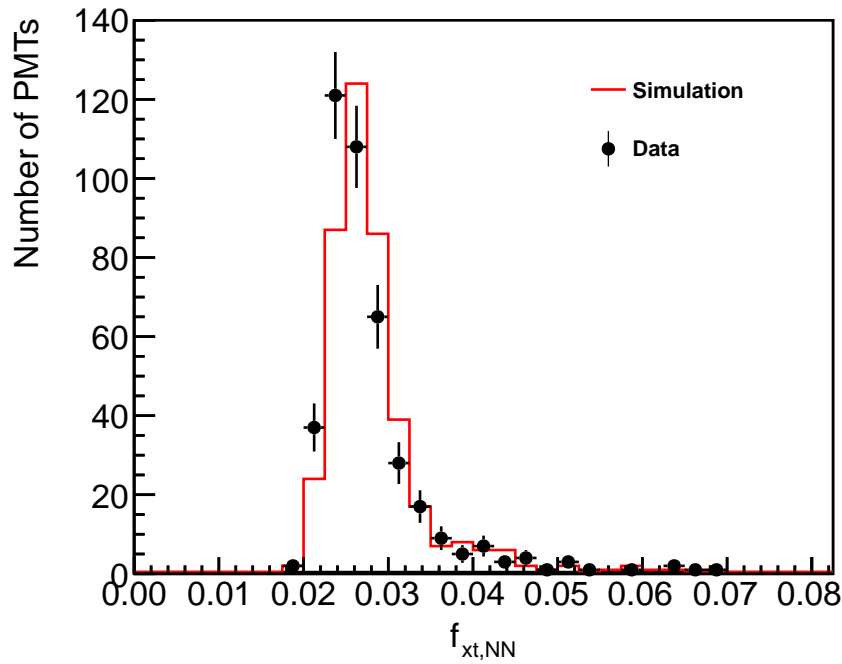


Figure 32: Distribution of nearest-neighbor pixel cross-talk,  $f_{xt,NN}$  in data (solid points) compared with simulation (red histogram). A detailed description of  $f_{xt,NN}$  is given in the text.

## 7. Muon Reconstruction

This section describes the reconstruction of tracks which start in the MINERvA detector and continue into MINOS. The tracks must first be found and associated (matched)



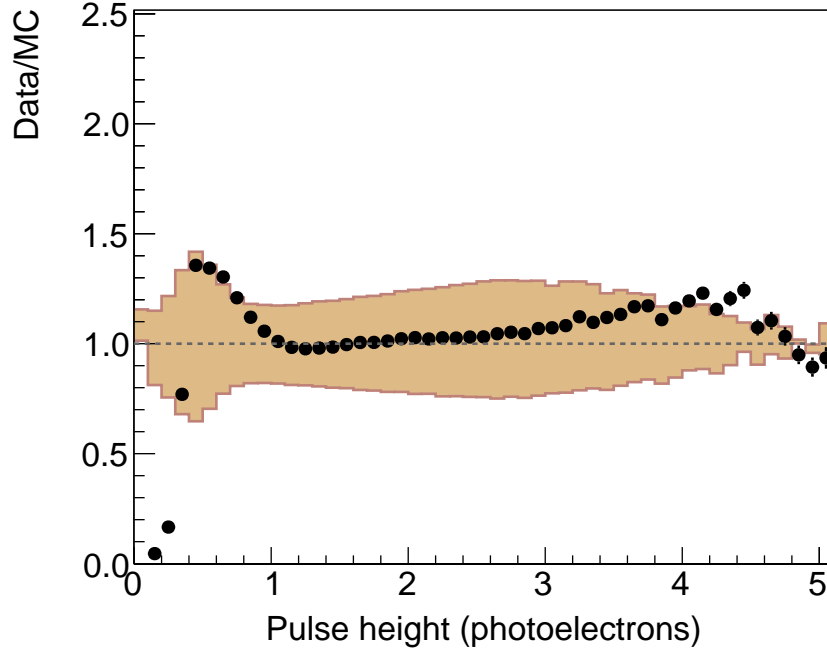


Figure 33: Ratio of data to simulation for the photoelectron pulse-height spectrum of measured cross-talk hits. The shaded region corresponds to the size of the systematic uncertainty assigned to cross-talk in neutrino analyses.

in the two detectors. The momentum is measured using range or curvature in MINOS and the sign of the track charge is determined using the direction of track curvature as described below.

### 7.1. Cluster Formation

Due to the overlapping triangular profiles of the scintillating strips in the central detector, particles traversing a plane will normally pass through at least two strips in the plane, and can induce activity in more than two strips, giving a “cluster” of activity. The first step in reconstruction of events is identification of clusters. Clusters are formed from groups of hits directly adjacent to each other in a single plane, within the same time slice. Any strip which does not register hits between strips with valid hits leads to a new clus-

ter being formed. An isolated strip without neighbors that has registered a hit is also identified as a cluster.

A position is calculated for each cluster based on the energy deposition in the strips. The energy-weighted position is calculated using all hits contained within a cluster. A time is also found for a cluster, where the time from the hit with the most energy within the cluster is assigned as the cluster time. The resulting clusters are classified by their composition. The types of clusters are: *low activity*, *trackable*, *heavily ionizing*, *superclusters*, or *cross-talk*.

- (i) *Low activity* clusters are those with a total energy deposit of less than 1 MeV.
- (ii) *Trackable* clusters meet the following requirements: total cluster energy between 1 and 12 MeV, four hits or fewer, and at least one hit with more than 0.5 MeV. If more than two hits have a hit energy greater than 0.5 MeV, they must be adjacent to each other.
- (iii) *Heavily ionizing* clusters must meet similar criteria to trackable clusters: total cluster energy greater than 1 MeV and one to three hits with energy greater than 0.5 MeV. If two or three hits are greater than 0.5 MeV, they must be adjacent to each other. In addition, it must not be a trackable cluster. Heavily ionizing clusters are important in forming high angle tracks.
- (iv) *Superclusters* are those with more than 1 MeV in energy that do not meet the criteria for either trackable or heavily ionizing clusters. Any cluster with five or more hits is automatically considered a supercluster.
- (v) *Cross-talk* clusters are identified by inspecting the PMT pixels associated with hits within that cluster. The PMT pixels associated with that cluster are compared to PMT pixels associated with a particle interaction. If these cluster PMT pixels are

found to be directly adjacent to the pixels related to the particle interaction, the cluster is considered to be a cross-talk cluster.

## 7.2. Track Reconstruction in MINERvA

A “track” is a reconstructed object that approximates a charged particle’s trajectory through the detector. Typically, only one track is needed to reconstruct a particle trajectory, but multiple tracks may be necessary if the particle undergoes a large-angle scatter or else decays. A single track pattern recognition scheme is used multiple times to find all tracks in an event.

The track pattern recognition uses all “seeds” within a single time-slice, where a seed is a collection of three trackable or heavy-ionizing clusters that meet the following requirements: no two clusters in the same plane; each cluster’s plane is in the same orientation (X, U, or V); clusters must be in consecutive planes, when the planes are sorted by orientation and longitudinal position; and clusters must satisfy a fit to a two-dimensional line. A single cluster may be used to make multiple seeds. These requirements limit seeds to an angle of less than  $70^\circ$  with respect to the longitudinal axis, which in turn imposes a similar limit upon reconstructed tracks.

Seeds within the same plane orientation are merged to form track “candidates”. The merger of two seeds requires that: the slope of the seeds’ linear fits are consistent; the seeds share at least one cluster; and the seeds do not contain different clusters in the same scintillator plane. If the algorithm merges two seeds into a candidate, it will attempt to merge additional seeds to the candidate using the same criteria. A seed may only be used by one candidate, therefore this stage of the algorithm is sensitive to the order of merging attempts. After all candidates are built, they may be merged using criteria similar to those for seeds; they must have consistent fitted slopes and intercepts and may not contain different clusters in the same scintillator plane. Track candidates are not required to share clusters and therefore may contain gaps, i.e. tracks that cross a scintillator plane without containing a cluster in that plane. This allows a track candidate to accurately follow

particle trajectories that intersect dead regions in the detector.

Two algorithms are used in succession to attempt to form 3D-track objects from track candidates. The first algorithm examines all possible combinations of three candidates in which no two candidates share the same plane orientation. Such a combination of candidates are formed into a 3D-track if they overlap longitudinally and are mutually consistent with the same three-dimensional line. By requiring a track candidate in each view, this algorithm is unable to form tracks that intersect fewer than 11 planes. The algorithm also searches for a particular topology in which a particle trajectory bends in only two views. In this instance, the combination of candidates will fail the overlap requirement because the candidate in the view without a visible bend will be longer. If this topology is detected, the longer candidate is broken into two shorter candidates and kinked tracks are found.

The second algorithm considers all remaining candidates that have not been used to make a track. It forms all possible combinations of two candidates which do not share the same plane orientation. If the candidates have a similar longitudinal overlap, they are used to construct a three-dimensional line. A search for unused clusters that have a position consistent with the candidate pair is then performed in the remaining view and a 3D-track is formed if a sufficient number of clusters is found. This algorithm is more successful in tracking particle trajectories that are obscured by detector activity in one of the three orientations and is able to make tracks that intersect as few as 9 planes. Both algorithms reject candidates that contain only one seed with an angle greater than  $60^\circ$  with respect to the neutrino beam direction; such candidates typically correspond to random energy deposits that happen to fit a straight line.

All 3D-tracks that are found are fit by a Kalman filter fit routine that includes multiple scattering[19]. The fit is required to converge, but there is no requirement placed on the fit  $\chi^2$ . Figure 34 shows the tracking position resolution after the Kalman filter fit. The fit is then used to add additional clusters to the track by searching nearby planes for which the track does not contain a cluster. Superclusters are made available here, allowing the

track to project into a region of shower-like activity (as in the case of a muon track that is partially obscured by a hadronic shower in all three views). Multiple tracks are allowed to claim the same cluster, each taking a fraction of its energy, to handle situations where two tracks intersect the same supercluster.

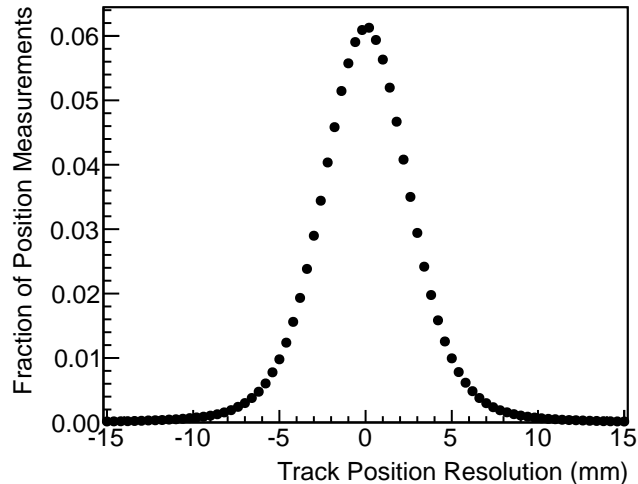


Figure 34: Resolution of the fitted positions along a track relative to the measured cluster positions for a sample of data rock muons. The RMS of the distribution is 3.1 mm.

Tracks produced by rock muons entering the front face of MINERvA with momentum less than 20 GeV were used to study tracking performance. Each track is divided into two cluster groups and upstream and downstream clusters are then fit separately into two independent tracks. The cluster at the break point is included in both tracks. The differences between the upstream and downstream track positions and angles is then a measure of the position and angular resolution, as shown in Fig. 35. The distributions in the data and simulation are consistent with each other. The position resolution is simulated to within 1 mm and the angular resolution is simulated to within 1 mrad. The position offsets are less than  $60\mu\text{m}$  in both transverse dimensions and the angular offsets are less than 1 mrad in both directions.

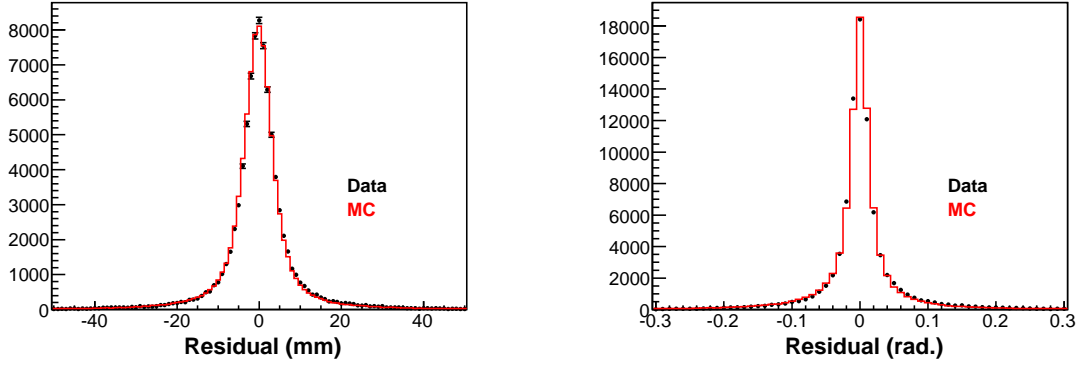


Figure 35: Residuals of fitted positions and angles between the upstream and downstream regions of tracks made in a rock muon sample.

The track pattern recognition scheme described above is used by a master reconstruction algorithm designed to reconstruct high-multiplicity final states while imposing restrictions to reduce the number of tracks formed from unrelated detector activity. If at least one track of 25 clusters or more is found, the longest track is designated the “anchor track” and its clusters are marked as used. The starting point of the anchor track is used to define the neutrino interaction location, called the primary vertex. The track pattern recognition is then re-run on the remaining un-used clusters. Tracks consistent with emerging from the primary vertex are identified and the primary vertex location is re-estimated with the Kalman filter technique[20] using all tracks. Tracks that are inconsistent with emerging from the primary vertex are deleted. The procedure is repeated, searching for tracks consistent with the endpoint of each track emerging from the primary vertex, in order to find particle trajectories that abruptly change direction due to secondary interactions. Figure 36 illustrates this procedure using event displays.

Each found track is submitted to a procedure, called “cleaning,” that removes extra energy, which varies according to the type of track found. The purpose of cleaning is twofold: to remove the energy that is likely to be unrelated to the tracked particle so that it may be used by future iterations of the track pattern recognition, and to improve the vertex energy measurement. Anchor tracks are typically found to be muons and are thus

expected to deposit energy as a MIP. If the track contains energy near the vertex that is inconsistent with a MIP, or contains a supercluster, the extra energy is removed from the track. Non-anchor tracks are assumed to be hadronic and only their superclusters are cleaned thereby minimizing bias in downstream particle identification algorithms. The non-anchored track will only use energy from the supercluster in strips that intersect the track fit. If the supercluster is near the track's endpoint, the track will incorporate as much energy as possible from the intersected strips in order not to disturb the energy loss profile of the Bragg peak. Otherwise, the track will use an energy equal to its mean cluster energy.

### 7.3. Charge Determination and Energy Reconstruction

The charges and momenta of muons exiting MINERvA are reconstructed using the MINOS near detector, which lies directly downstream of the MINERvA detector. The MINOS calorimeter region is designed to measure both shower energies and muon momenta, while the downstream spectrometer region is only used for tracking. The MINOS coordinate system is defined as follows: the positive  $Z$ -axis is parallel to the coil and points downstream; the positive  $Y$ -axis is  $90^\circ$  with respect to the  $Z$ -axis and points upward. The  $X$ -axis is orthogonal to the other two axes. The center of the MINOS coordinate system is located at the intersection point between the coil and the first steel plane. Typically, muons produced with momenta between 0.5 and 6 GeV/ $c$  within MINERvA and matched to MINOS are contained in the MINOS calorimeter region. Higher momentum muons stop in the MINOS spectrometer region or escape MINOS completely. Given the transverse extent of MINOS relative to MINERvA, the MINOS detector provides coverage only for muons created that are at most  $20^\circ$  relative to the  $Z$ -axis.

Charged particles traversing MINOS are deflected due to the magnetic field. From this deflection, information about the charge and momentum of the particle can be extracted using the same procedures used by the MINOS collaboration. [27]. In neutrino mode, if the deflection is towards the coil, the muon is negatively charged; and if the muon is deflected away from the coil, the charge is positive. The coil polarity is normally

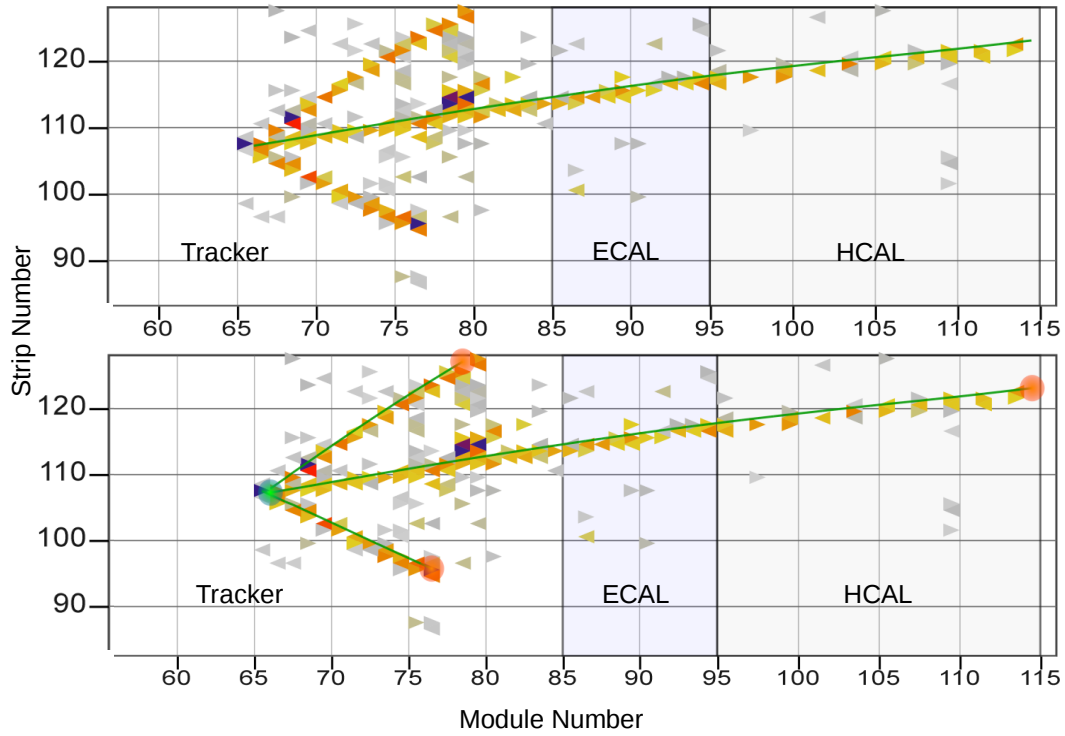


Figure 36: Display in X-view of a neutrino interaction recorded in data. Each triangular “hit” depicts a single scintillator strip with deposited energy. Reconstructed tracks (vertices) are indicated by superposed lines (dots). Initially the reconstruction algorithm finds a long muon-like anchor track (upper display) and the primary vertex location is inferred. Then additional tracks emerging from the vertex are searched for. In this event, two hadronic tracks are found and further constrain the vertex position (shorter lines and solid dot in the lower display).



reversed in anti-neutrino mode to ensure that the dominant neutrino type is focused by the spectrometer.

For tracks in MINERvA and MINOS to be merged into a muon candidate, the two tracks under consideration must be within 200 ns of each other in time, MINERvA tracks must have activity present in at least one of the last five modules of the detector, and the MINOS track must start within one of the first four planes of MINOS.

Two separate methods are used to match tracks: a track projection method and a closest approach method. For the track projection method, the MINOS track is extrapolated to the plane that contains the last activity on a MINERvA track and the MINERvA track is extrapolated to the plane that contains the start of the MINOS track. The position of the most downstream activity on a MINERvA track is computed with the projection of the MINOS track, and likewise the projection from MINERvA is compared to the start of the MINOS track. The distance between these points is called the match residual. If both match residuals are smaller than 40 cm, the tracks are considered matched tracks. If multiple candidate matches exist, the match with the smallest residual is taken.

If no matches are found using the track projection method, a closest approach method is used. The MINOS track is projected toward MINERvA and the MINERvA track is projected toward MINOS and the point of closest approach of the two tracks is found. This method can be useful if the muon undergoes a hard scatter in the passive material between the two detectors (for example, the support structure of the MINERvA detector or the first MINOS steel plane). The MINERvA tracks matched to a MINOS track are almost exclusively muons giving a high level of confidence to the particle identification in such cases.

The  $\mu^\pm$  momentum in MINOS is determined by two different methods: range and curvature. The range method is based on total energy loss through interactions in the MINOS detector and is applied only to muons that are contained inside the calorimeter region. The curvature method reconstructs the momentum by means a track fitting algorithm developed by MINOS [29]. The algorithm relates the curvature of the track

( $K$ ), the magnetic field ( $B$ ) and the momentum component perpendicular to the field ( $P$ ), according to

$$K \equiv \frac{1}{R(cm)} = \frac{0.3 B(kGauss)}{P(MeV)}, \quad (9)$$

where  $R$  is the radius of curvature.

The two methods differ in their ability to reconstruct momentum, as illustrated in Figs. 37 and 38. The  $P_{range}$  method is more precise; its estimated systematic uncertainty is 2% [27] derived from uncertainties on the simulation of the MINOS geometry, detector mass, and  $dE/dx$  parameterization, and track vertex reconstruction. The momentum resolution for muons in MINOS is 10% (5%) for muons measured by curvature (range)[28].

For muons initiated in MINERvA which are sufficiently energetic to escape from the calorimeter region of MINOS, the momentum is reconstructed via the  $P_{curv}$  method. This is done because the coarser sampling in the MINOS spectrometer region and the fact that the signals in that region are summed together. Both facts together result in a potential bias in momentum determinations based on range due to the high accidental activity. MINERvA has developed an approach to calculate the systematic uncertainty of the  $P_{curv}$  method that is similar to that used by the MINOS collaboration [27].

This study does differ from that of MINOS because it uses a high-statistics rock muon sample illuminating the entire face of the MINOS detector and it uses a well-defined track vertex at the front face of the MINOS detector. For this study, only muon tracks that are contained in the fully instrumented part of MINOS are used, so that information is available from both the  $P_{range}$  and  $P_{curv}$  methods.

In order to determine the systematic error on  $P_{curv}$ , the  $(1/P_{curv} - 1/P_{range})$  distributions of the data and the simulation were divided into six  $P_{range}$  bins to determine the error as a function of the momentum. The arithmetic means for the data,  $\bar{\mu}_{data}$ , and simulation,  $\bar{\mu}_{MC}$ , distributions are found. Then the *curvature difference*, defined as  $\Delta K = |\bar{\mu}_{data} - \bar{\mu}_{MC}|$ , or the deviation of the  $1/P_{curv}$  measurement from the  $1/P_{range}$  measurement is obtained. For small curvature uncertainty,  $\Delta K$ ,  $\Delta P_{curv} = -P_{curv}^2 \Delta K$ . The additional systematic uncertainties on muon momenta measured by curvature are 0.6% for muons with momenta

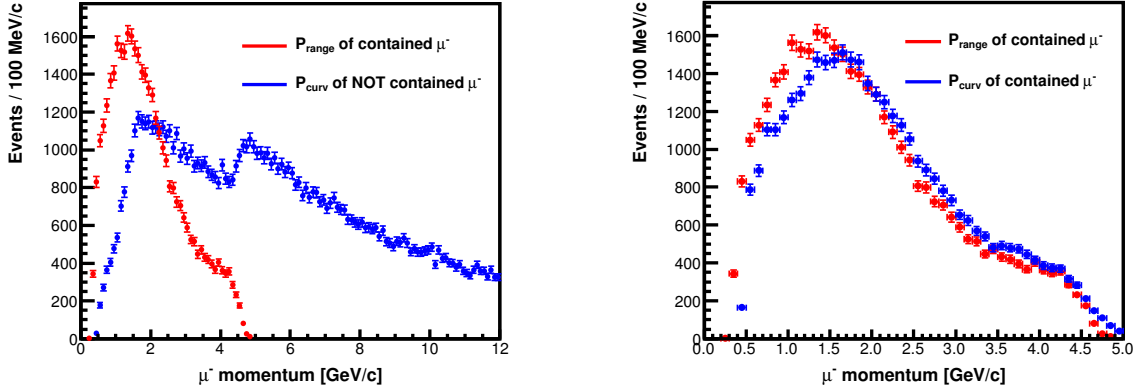


Figure 37: Left: The distribution in  $P_{range}$  of muons contained in the calorimeter region versus the distribution of  $P_{curv}$  for non-contained muons. The contained muon sample peaked at lower momentum. Right: Comparison of  $P_{range}$  and  $P_{curv}$  distributions of contained muons. The plot shows that the two methods for reconstructing the momentum have different resolutions and reconstruction biases, especially at lower momenta.

greater than 1 GeV/ $c$  and 2.5% for those less than 1 GeV/ $c$ . The range and curvature uncertainties for muons measured by curvature are added in quadrature to obtain the total muon momentum uncertainty for muons measured by curvature of 2.1% (3.1%) for muons with momenta above (below) 1 GeV.

#### 7.4. Muon Reconstruction Efficiency and Acceptance

The muon reconstruction efficiencies are evaluated using simulated inclusive charged current muon neutrino interactions inside the MINERvA detector tracker region. All muons are counted in the efficiency denominator, and the efficiency numerator is determined by matching reconstructed tracks to the true particle trajectory that deposited the most energy into the clusters on the track. A true muon is “tracked” if a track is matched to it in this manner.

Figure 39 shows the muon tracking efficiency as a function of momentum and angle with respect to the longitudinal axis, respectively. The tracking efficiency decreases below 2.0 GeV/ $c$  primarily due to the requirement that the anchor track contain at least 25

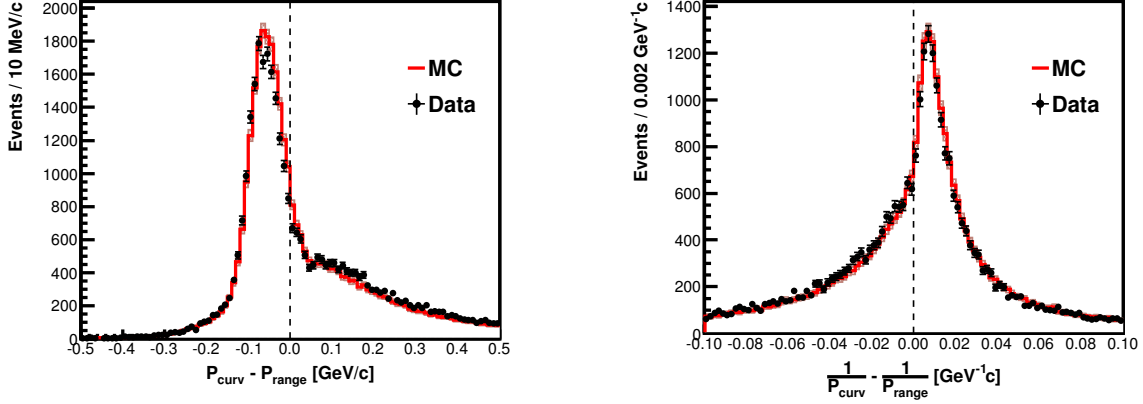


Figure 38: Left: Residual  $P_{\text{curv}} - P_{\text{range}}$  distribution of all CC inclusive events where the muon stops in the calorimeter region of MINOS. Right: Residual  $1/P_{\text{curv}} - 1/P_{\text{range}}$  distribution for the same events. This distribution is used to determine the systematic uncertainty for the curvature-based measurement relative to the range-based measurement.

clusters. The MINOS muon acceptance turns on at approximately 2.0 GeV/ $c$  because of the requirement that the muon pass through 25.4 cm of steel to be tracked in MINOS. As a result, the anchoring requirement in MINERvA does not inhibit charged current (CC) analyses that require MINOS-matched muons. The angular efficiency decreases sharply around  $60^\circ$  because only trackable and heavy-ionizing clusters are initially used in the track pattern recognition. The more gradual decline in efficiency between  $20^\circ$  and  $60^\circ$  is attributed to muons that exit the inner detector before crossing the minimum number of planes needed to form a track. The MINOS angular acceptance is zero above  $20^\circ$ , so again the limitations of the track pattern recognition do not inhibit MINOS-matched muon analyses.

## 8. Recoil Energy Reconstruction

MINERvA is a finely grained detector, capable of identifying individual particles in the recoil system (event energy not associated with the primary lepton) for moderate multiplicity events. As of early 2013, the energy of the recoil system is reconstructed

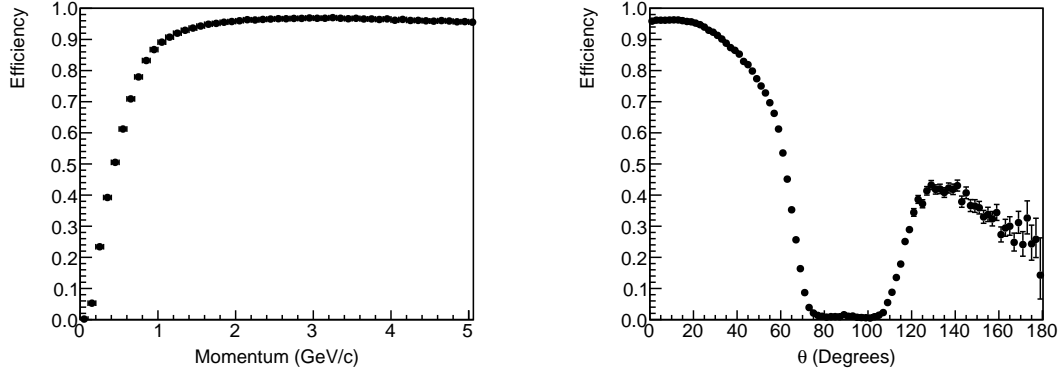


Figure 39: Muon tracking efficiency as a function of muon momentum (left) and angle with respect to Z-axis (right). The shape of the efficiencies is primarily a function of the number of planes intersected by the muon trajectory. Backwards muons are tracked less often because they typically have momenta below 1 GeV/ $c$ .

by calorimetrically summing energy depositions within the detector, without regard to the topology of the event. In the future, a more complete algorithm will be developed which identifies individual final state particles and compensates for electromagnetic and hadronic depositions to improve energy resolution.

MINERvA currently employs a simple calorimetric sum in which energy in the sub-detectors not associated with the muon track is weighted to account for the active fraction of the scintillator planes and additional passive absorber. The calorimetric constants are determined by the  $dE/dx$  of a minimum ionizing particle at normal incidence. For a given sub-detector, the calorimetric constant is given by:

$$C^{sd} = \frac{E_{\text{abs}} + E_{\text{sc}}}{f \times E_{\text{sc}}}, \quad (10)$$

where  $E_{\text{abs}}$  is the energy loss in one absorber plane,  $E_{\text{sc}}$  is the energy loss in one scintillator plane, and  $f$  is the active fraction of the scintillator plane in that sub-detector. For the central tracking region,  $E_{\text{abs}} = 0$ , yielding  $C^{sd} = 1/f = 1.222$  from the 81.85% active fraction. The corresponding fractions for the ECAL and HCAL are 2.013 and 10.314. The constant for the OD is likewise calculated assuming normal incidence into the OD

(orthogonal to the beam axis).

An overall calorimetric scale is derived by fitting calorimetric reconstructed recoil energy to true recoil energy for simulated events. True recoil energy is defined as the energy of the neutrino minus the energy of the outgoing lepton

$$E_{\text{recoil}}^{\text{true}} \equiv E_{\nu} - E_{\text{lepton}} \quad (11)$$

Calorimetric reconstructed recoil energy is defined as:

$$E_{\text{recoil}}^{\text{cal}} \equiv \alpha \times \sum_i C_i^{\text{sd}} E_i \quad (12)$$

where  $\alpha$  is the overall scale,  $i = \{\text{central tracking region, ECAL, HCAL, OD}\}$ ,  $C_i^{\text{sd}}$  is the calorimetric constant for sub-detector  $i$  and  $E_i$  is the total visible recoil energy in sub-detector  $i$ , calculated from all clusters of hits within a  $-20$  to  $35$  ns window around the event time (defined by the muon) and not identified as cross-talk. This time window is narrower than a typical time slice to remove pile-up from neutrino and background interactions that are adjacent in time. The cross-talk rejection prevents energy from the muon track being included in the calorimetric sum.

The parameter  $\alpha$  is determined by minimizing the quality factor  $Q$

$$Q = \sum \frac{[\arctan(E_{\text{recoil}}^{\text{cal}}/E_{\text{recoil}}^{\text{true}}) - \pi/4]^2}{N}, \quad (13)$$

where the summation is over events of true recoil energy between  $1.0$  and  $10.0$  GeV, and  $N$  is the total number of such events. This metric is less susceptible to the asymmetric tails of the  $E_{\text{recoil}}^{\text{cal}}/E_{\text{recoil}}^{\text{true}}$  distribution, which is bounded below by zero, and bounded from above by energetic hits in the active portion of the calorimeters (which are weighted up by the calorimetric constants) and overlapping events.

After fitting  $\alpha$ ,  $\Delta E/E_{\text{recoil}}^{\text{true}} = (E_{\text{recoil}}^{\text{cal}} - E_{\text{recoil}}^{\text{true}})/E_{\text{recoil}}^{\text{true}}$  is plotted in bins of true recoil energy. A per-bin energy correction is derived in the form of a polyline mapping  $E_{\text{recoil}}^{\text{cal}}$  to  $E_{\text{recoil}}^{\text{cal}'}$ . Each node on the polyline corresponds to one true recoil energy bin, with

$$x = E_{\text{recoil}}^{\text{cal}} = \langle E_{\text{recoil}}^{\text{true}} \rangle \times (1 + \eta) \quad (14)$$

$$y = E_{\text{recoil}}^{\text{cal}'} = \langle E_{\text{recoil}}^{\text{true}} \rangle, \quad (15)$$

where  $\langle E_{\text{recoil}}^{\text{true}} \rangle$  is the average true recoil energy in the bin, and  $\eta$  is the mean of a Gaussian fit to the distribution. For example, if a bin with  $\langle E_{\text{recoil}}^{\text{true}} \rangle = 1.0$  GeV is 3% low ( $\eta = -0.03$ ), the polyline maps 0.97 GeV to 1.0 GeV. The lower limit of the polyline is fixed at (0.0, 0.0) GeV; the upper limit is fixed at (50.0, 50.0) GeV.

For simulated charged-current events with MINOS-matched muons and with vertices within the fiducial tracking region, the value  $\alpha = 1.568$  is obtained, with a calorimetric energy resolution of  $\sigma/E = 0.134 \oplus 0.290/\sqrt{E}$  (see Fig. 40). The observed calorimetric energy resolution is a convolution of many effects: final-state interactions, shower fluctuations to electromagnetic, hadronic and neutral components, passive absorber deposition, scintillator, PMT and electronics response, attenuation along scintillator strips, containment in the detector, and overlapping events. For the lowest recoil energies (below 1 GeV) the systematic uncertainty is considerably lower than suggested by the parameterization. This is due to the fact that for those events the recoil system is dominated by a single proton that is not subject to many of the sources of shower fluctuations, and the particle is usually contained in the fully active region. In these cases the resolution is better if the ionization profile is fit to a proton hypothesis, as described in Sec. 10.2.

## 9. Test Beam Detector Response Calibration

The simulation of the calorimetric response of single final state particles in the MINERvA detector has been validated in a test beam program at the Fermilab Test Beam Facility in 2010. A dedicated tertiary test beam with hadron momenta between 0.4 and 2.0 GeV/ $c$  was used to study the response of a small test detector of similar design to the full MINERvA detector. The beam line included a spectrometer for momentum analysis and a time-of-flight system for particle identification. A stack of 40 scintillator planes of 1.15 m<sup>2</sup> active area, identical to MINERvA planes other than the smaller transverse dimension was exposed using two different configurations. The first configuration, with no absorber in front of the first 20 planes and Pb absorber before each of the downstream 20 planes, corresponds to the downstream tracker region and ECAL. The second configura-

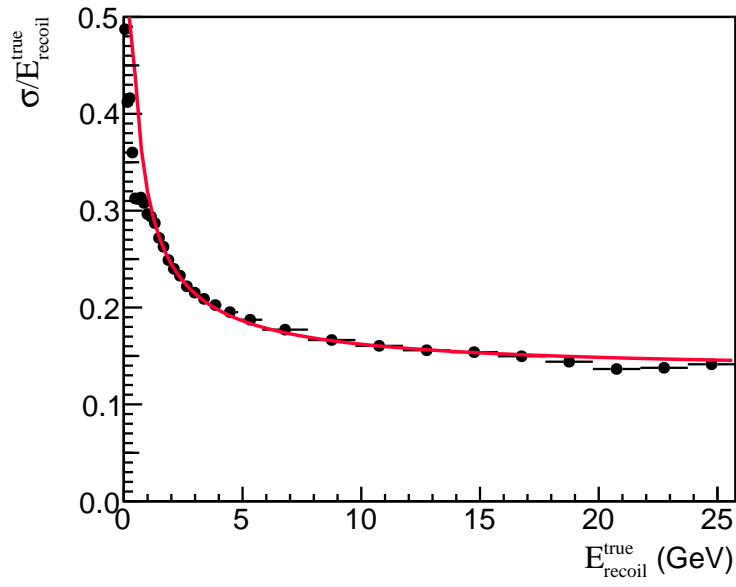


Figure 40: Calorimetric energy resolution for simulated charged-current inclusive neutrino events in the MINERvA detector. The points show the width of a Gaussian fit to the difference between the measured and true recoil energy divided by the true recoil energy, binned by true recoil energy. The line represents a functional fit,  $\sigma/E = 0.134 \oplus 0.290/\sqrt{E}$ .



tion, with lead upstream and steel downstream, is very similar to the ECAL and HCAL region of the MINERvA detector.

Other than the smaller transverse size, the detector design, electronics, and software are intentionally as similar to the full MINERvA detector as possible. The most important differences are as follows: the air gap between planes and passive absorber is larger for the tracker and ECAL configurations, the typical light yield is doubled due to the shorter average fiber length, sets of four planes alternate readout on opposite sides instead of all from the same side, and the muon energy response calibrations are primarily done with cosmic-ray muons. These produce differences in response that are accounted for in the simulation and through the identical in-situ calibration procedures. Calibrations have been performed for the beamline momentum, the detector response to cosmic ray muons, and unrelated particle activity from the beamline. The uncertainties in the material assay are comparable to the uncertainties in the calibrations.

These data are compared to a Monte Carlo simulation of the testbeam detector geometry and its response using the same software and calibration infrastructure as the full MINERvA detector. In order to assure that simulation and data share the same beam phase space, the particles trajectories input to the detector simulation are derived from data events with added resolution smearing based on multiple scattering in the beamline. The hadronic interaction model used in the simulation is the Bertini Cascade model packaged with the 9.4.p02 version of GEANT4[9].

### 9.1. Pions

The GEANT4 simulation of pions is approximately consistent with the pion data in the ECAL + HCAL configuration as illustrated in Fig. 41. At the low end of the momentum range, differences between the data and simulation are 5% on average, with the simulated response somewhat lower. Consequently a 5% uncertainty is assigned to the calorimetric energy response for pions in that energy regime. The energy resolution is well reproduced in the simulation.

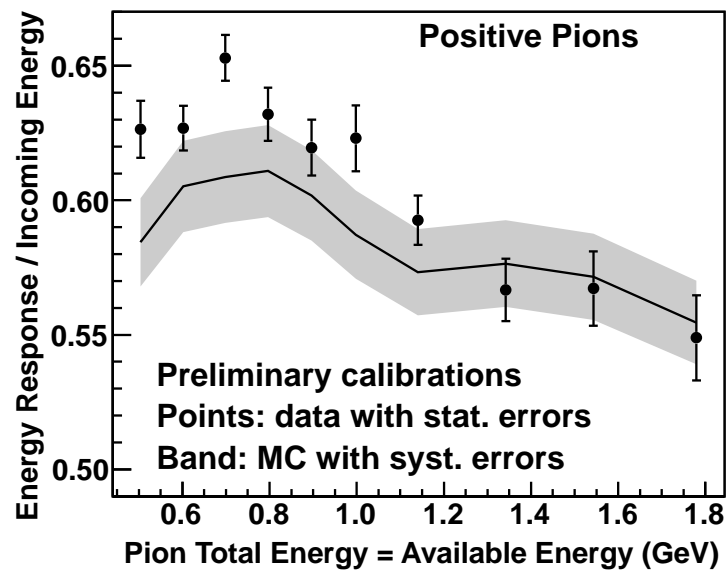


Figure 41: Results from calorimetry analysis for positive pions. The error band represents relative uncertainties between the data and simulation; there is an additional systematic uncertainty in the relative scale between simulation and data of 3%.

## 9.2. Protons

A proton sample is used to set constraints on the proton calorimetry response. An analysis similar to the pion case for the ECAL + HCAL configuration gives an uncertainty in the calorimetric response of 5% for protons of momenta between 1 and 2 GeV/ $c$ .

### 9.2.1. Stopping protons and Birks' parameter

The proton sample is also used to study the Birks' law behavior of stopping protons in the central tracking region. The central tracking + ECAL configuration has too little material to contain interacting protons of momenta exceeding 1 GeV/ $c$ , but does provide constraints on calorimetry for lower momenta. A subset of the latter sample is used to study saturation behavior of the scintillator, which is commonly parameterized using Birks' Law, where the ionization is scaled by a factor of  $(1 + k_B \times dE/dx)^{-1}$ . Events are selected which terminate in a tracking region plane between 11 and 19 and have a gap of no more than one plane upstream of that point.

For all planes of all selected proton events, the distribution of energy loss per plane is formed as a function of the number of planes from the end of the event and shown in Fig. 42. The data in the figure are constructed from a Gaussian fit to the energy-per-plane distribution. The central value from the Gaussian fit is shown for the data and simulation, while the fit uncertainty is also shown for the data. The uncertainty at the end of the track is larger because that final distribution is not Gaussian. There is a range of observed energy loss from protons that travel only a short distance into the plane to protons that stop just before they would have exited the plane. This leads to a larger spread in the peak energy loss. The data lie between two alternative Birks' parameters at  $\pm 30\%$  of the nominal value ( $k_B = 0.133\text{mm/MeV}$ ). The  $\pm 30\%$  is taken to be the estimate of the uncertainty in the parameter. For physics in this region that is sensitive to both the total proton response and the Birks' parameter, such as activity near the neutrino interaction vertex, the uncertainty in the response (3.5%) and the Birks' parameter uncertainty are added in quadrature.

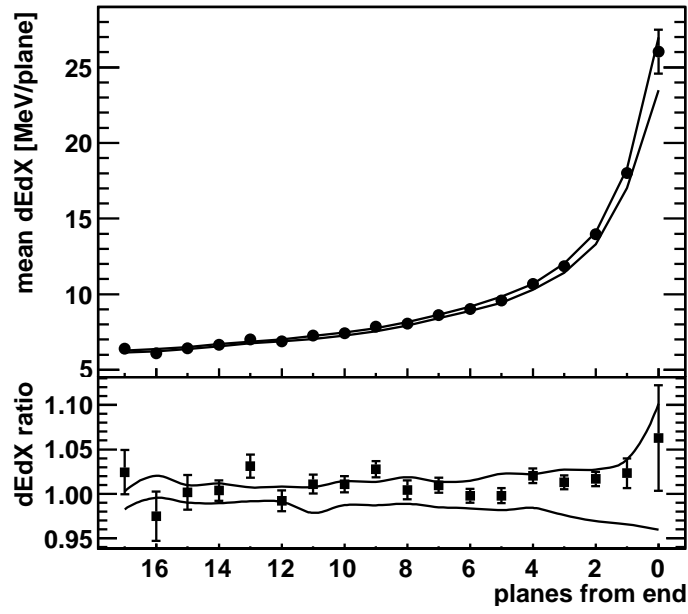


Figure 42: Energy loss profile for protons that stop at the end of their range. The two smoothed lines in each part of the figure show the high-statistics simulated profile with a Birks parameter that is 30% lower (top) and higher (bottom), corresponding to higher and lower response, respectively. The ratio is taken relative to the default simulation (not shown).

A full description of the test beam program and associated measurements is the subject of a separate manuscript which currently is in preparation.

## 10. Detector Performance

Once all calibration procedures are complete, several checks are done to ensure that the detector's energy scales are accurate, well-modeled in the simulation, and constant over time. Charged current events in the detector are used as checks, since their analysis requires all the calibration steps described in this article, and occur at high enough rates to provide precise measurements of the energy scales as a function of time. Another check of the reconstruction is the energy deposition at the end of a track for particles that stop in the active region of the detector. Other calibration cross-checks use the electrons that come from muon decays, for those muons that stopped in the detector (Michel electrons). This chapter demonstrates the performance of the calibrated detector using these three data samples.

### 10.1. Charged Current Interactions

Muon neutrino and muon antineutrino charged current (CC) interactions occurring within the ID volume provide high statistics checks of both the muon and recoil energy reconstruction, since the CC reactions  $\nu_\mu(\bar{\nu}_\mu)N \rightarrow \mu^-(\mu^+) + X$ , include both a muon and a hadronic recoil system.

Events are selected as follows: first, the event must contain a reconstructed track which matches a muon reconstructed in the MINOS detector where its momentum and charge are determined; second, the reconstructed muon vertex must lie within a fiducial volume in the scintillator-only section of the MINERvA ID (see Sect. 1.1). The event must not contain any dead channels induced by previous interactions. Channels whose discriminators trip due to detector activity experience a dead-time, where they are insensitive to new energy, during an approximately 100 ns push-and-reset period which follows the  $\sim 150$  ns charge integration window. We require that there be no more than

one such dead discriminator in a path projected upstream of the muon track. This selection is essential to prevent rock muons with tracks partially lost to dead time from being confused with fiducial events.

Figure 43 shows the mean muon energy and the mean recoil energy, as functions of integrated protons on target over the first four months of neutrino data taking (left) and the first four months of antineutrino data taking (right), corresponding to  $10^{20}$  protons integrated on the NuMI target. The mean muon energies are constant to within 1.5% (1.2%) over the time shown for the neutrino (antineutrino) running. The mean recoil energies are constant to within 3.0% (3.5%) over the time shown for the neutrino (antineutrino) running.

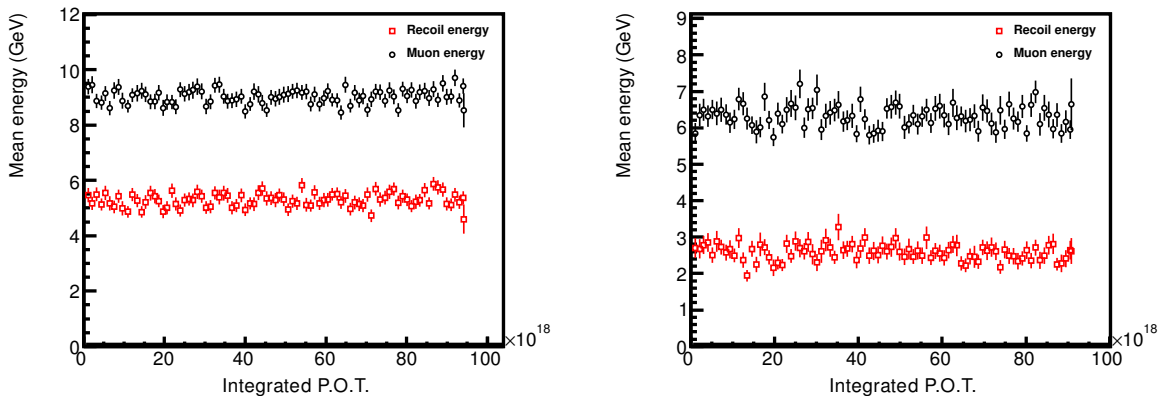


Figure 43: Mean muon and recoil energies in CC neutrino (left) and antineutrino (right) events as a function of integrated protons on target (POT). Each point corresponds to  $10^{18}$  POT, which is approximately one day of running.

## 10.2. Energy Loss for Stopping Particles

The granularity and light yield of the detector make it possible to use  $dE/dx$  profiles near the ends of the tracks to identify some of the particles that stop in the detector. In cases where the hadron loses energy via electromagnetic processes, decays in flight, elastically scatters, or undergoes minimum inelastic hadron scattering, the  $dE/dx$  distinguishes

between minimum and heavily ionizing particles. However, because hadrons traversing the detector can undergo various other processes, such as inelastic scattering, pion charge exchange, and absorption in flight, the particle's  $dE/dx$  profile cannot always be used in this fashion.

In practice, for every track that is found, a  $\chi^2$  is determined by comparing the energy deposited per scintillator plane to templates derived from the  $dE/dx$  profile expected in the detector for different momenta and for two different particle types: pion and proton.

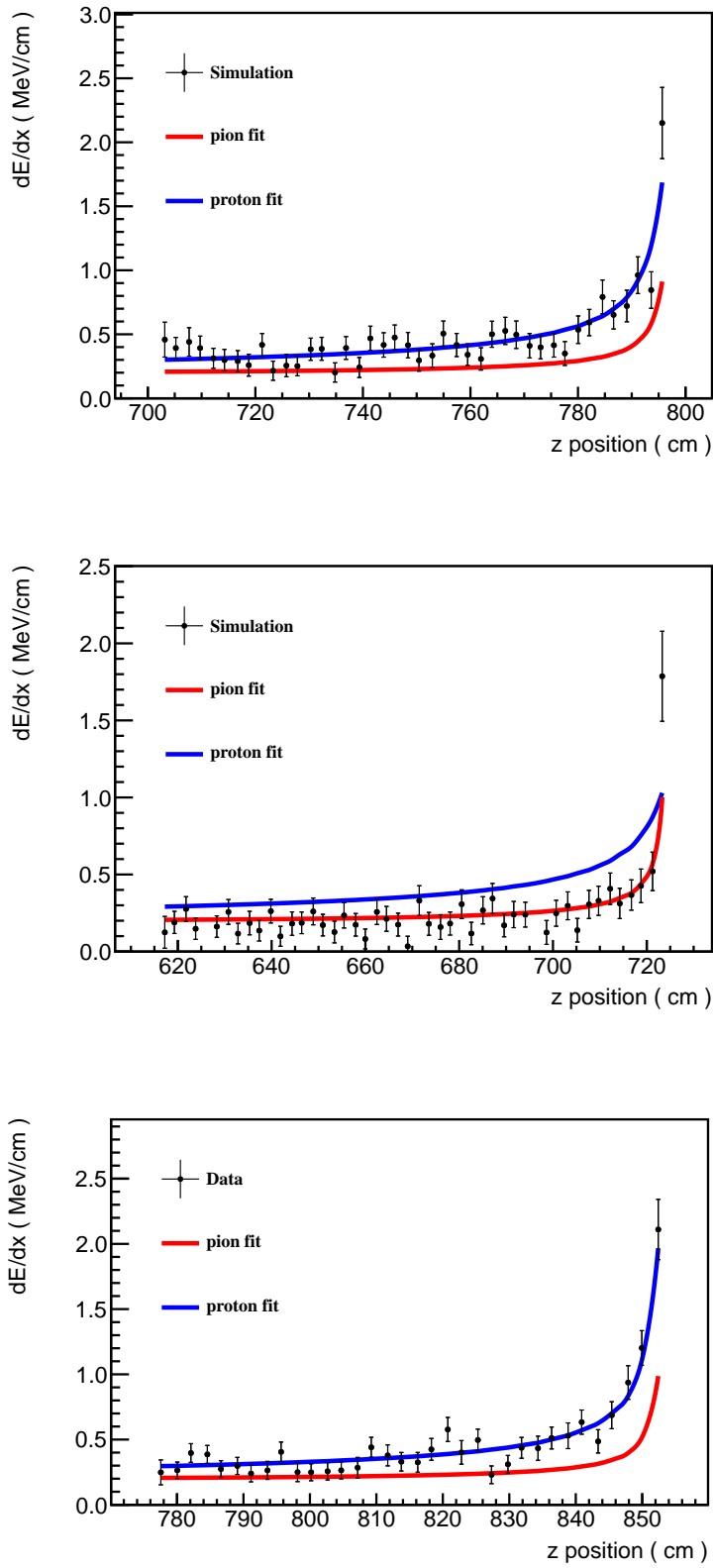
Figure 44 shows the  $dE/dx$  profiles for two events from the detector simulation and an event from the data compared to pion and proton templates. The topmost profile shows a proton generated with a momentum of 1.0 GeV/ $c$ ; the  $\chi^2$  for the proton (pion) hypothesis is 34 (177) for the 41 degrees of freedom (planes traversed). The reconstructed momentum for the proton (pion) hypothesis is 1.2 (0.475) GeV/ $c$ . The center profile shows a simulated pion of 0.385 GeV/ $c$  momentum; the  $\chi^2$  for the pion (proton) hypothesis is 31 (185) for the 39 planes traversed. The reconstructed momentum for the pion (proton) hypothesis is 0.36 (1.00) GeV/ $c$ . The lower profile is taken from a reconstructed track in data, where the measured proton (pion) momentum is 1.00 (0.36) GeV/ $c$  and the  $\chi^2$  for the proton (pion) hypothesis is 29 (197) for 33 degrees of freedom.

When available, the  $dE/dx$  information is also used to measure energy for stopping particles more precisely than a calorimetric energy sum. Figure 45 shows the predicted momentum resolution derived from  $dE/dx$  information for protons and pions that stop in the inner tracking region of the MINERvA detector.

### 10.3. Michel Electrons

Michel electrons are produced by a stopped (anti-) muon from a neutrino interaction or the decay chain of  $\pi^\pm$ . The response of the detector to Michel electrons at different locations provides a cross-check of the relative calibration. The overall electromagnetic energy scale can also be checked by comparing the Michel electron spectrum in the data to that predicted by a simulation tuned to muon energy depositions.

In principle, a Michel electron is most cleanly identified by searching for a delayed



88  
Figure 44:  $dE/dx$  profiles for a typical simulated proton (top) and pion (middle) interaction, and for a clearly identified proton candidate in the data (bottom).



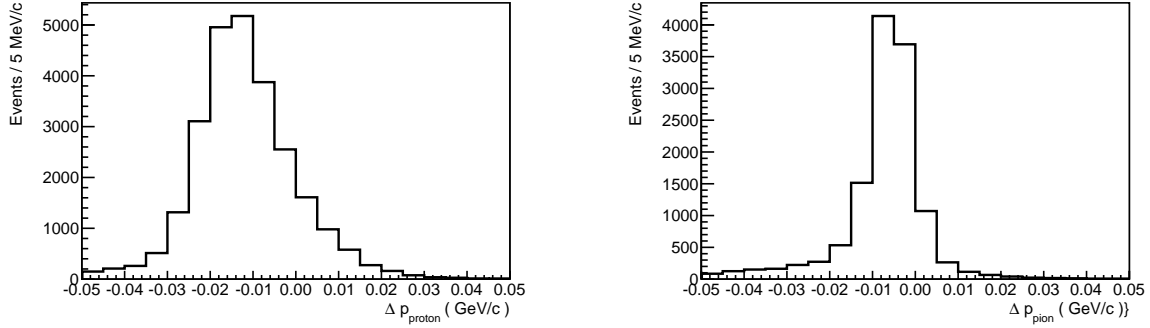


Figure 45: Momentum resolution for protons (left) and pions (right) obtained for simulated reconstructed tracks that stop in the MINERvA inner tracking detector.  $\Delta p$  is the difference between the reconstructed and true momentum of the single particle.

signal near the endpoint of a stopped muon track. However, isolated energy depositions in time slices with no other detector activity are found to be predominantly due to delayed Michel electrons. The full sample of such energy depositions can therefore be used without requiring an identified precursor muon.

Figure 46 shows the energy spectrum comparison between data and simulation, where the simulation only includes neutrino interactions in the detector and the data includes all low energy candidates. The lack of a high-side tail in the energy distribution shows that the non-Michel background is low and can be ignored in this comparison. The means of the distributions agree to within 3%.

#### 10.4. Energy loss by Electrons and Photons

The separation of electrons from photons is important for studying electromagnetic final states in MINERvA. The high granularity and low  $Z$  nuclei of the central tracking region allows the  $dE/dx$  near the beginning of electromagnetic showers to be used to distinguish electrons from photons. Electrons lose energy as a single highly-ionizing particle near the start of a track. Because a photon produces an electron-positron pair when it converts to form a track, the energy loss is then twice that of an electron. This difference in  $dE/dx$  is only valid near the start of a shower because an electromagnetic (EM) shower

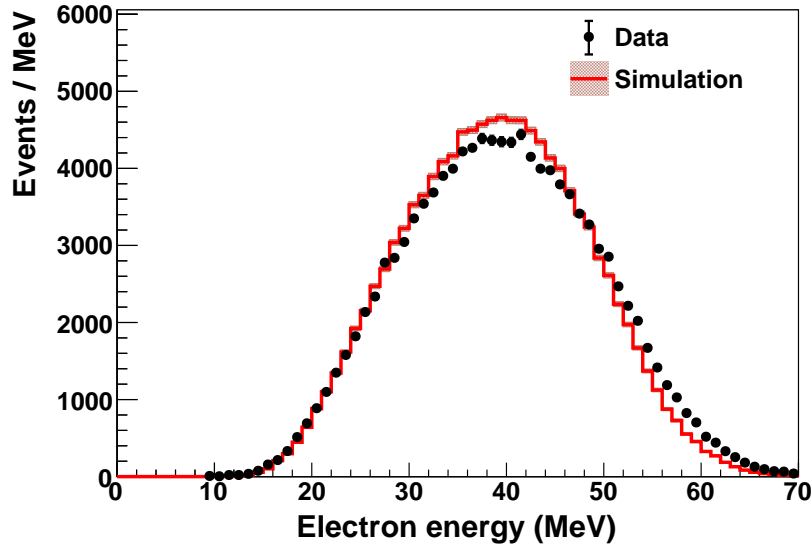


Figure 46: Energy distribution of Michel electron events observed in the detector (solid points) compared to the full detector simulation (histogram).

develops stochastically as it propagates. Consequently, the average  $dE/dx$  over the first four planes at the start of an EM shower is a good discriminant. A distribution of the average  $dE/dx$  over the first 4 planes for Michel electron events is shown in Fig. 47.

## 11. Conclusions

The MINERvA detector has been operating since March 2010, and has achieved a total integrated live time exceeding 97% for the “Low Energy” run that extended through the end of April 2012. During that time over 99.5% of the channels were live and calibrated, using *in situ* neutrino beam-induced calibration samples and *ex situ* tests.

The detector energy scale for the signal initiated by minimum ionizing particles is understood at the 2% level and the response has been calibrated to be constant to better than 1% across the 200 scintillator planes in the detector. Although the light level decreased by over 15% due to scintillator aging during the course of the initial two-year run, a calibrated energy stability of better than 2.5% and a timing resolution of better than

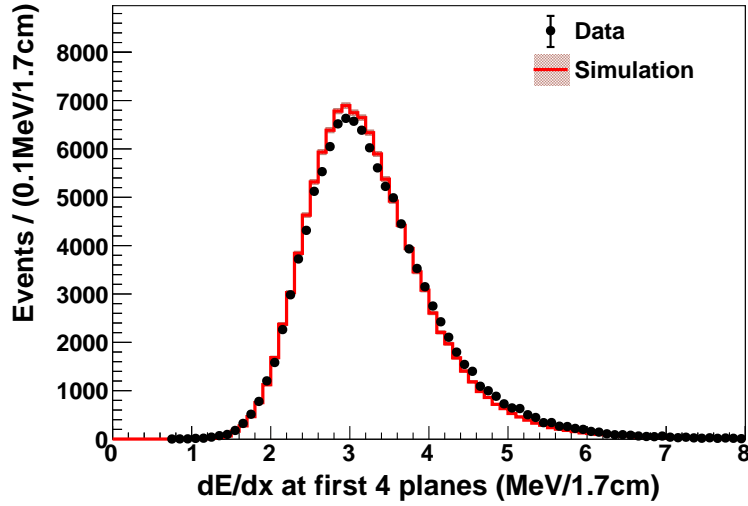


Figure 47: Average  $dE/dx$  over the first 4 planes of Michel Electron events.

4 ns has been achieved over the length of the run. The detector alignment, light collection, and calibration procedures result in a detector whose position resolution per plane for muons impinging perpendicular to the scintillator plane is 3.1 mm. The calorimetric energy resolution of the detector is estimated to be  $\sigma/E = 0.134 \oplus 0.290/\sqrt{E(\text{GeV})}$  for hadron showers generated by neutrino interactions. Using a test beam and a smaller version of the detector, the hadron energy scale has been determined to 5% for pions, and the Birks' law constant to characterize saturation in the scintillator has been constrained to  $0.133 \pm 0.040 \text{ mm/MeV}$ . Knowledge of this constant is particularly important for measuring energy depositions of low energy protons which may be in the final state of neutrino quasi-elastic interactions.

The detector composition is an important part of any cross section measurement. The fiducial masses and chemical makeup of this detector and its various nuclear targets have been measured at the 1.5% level for the scintillator planes and at the 1% level for the solid nuclear targets.

The MINOS near detector plays an integral role in any MINERvA CC cross section measurement. The MINERvA implementation of the MINOS near detector geometry and

reconstruction are shown to give an absolute muon energy scale to 2.6% (3.1%) for muons above (below) 1.0 GeV for muon momenta measured by curvature. The momentum uncertainty for muons measured with range is 2%, as determined by MINOS material assay,  $dE/dx$  parameterization, and track reconstruction uncertainties.

In summary, detailed neutrino cross section measurements for both exclusive and inclusive channels for a wide range of target nuclei is now underway as the result of implementation by MINERvA of the detector design and calibration approaches reported in this article.

## 12. Acknowledgments

This work was supported by the Fermi National Accelerator Laboratory, which is operated by the Fermi Research Alliance, LLC, under contract No. DE-AC02-07CH11359, including the MINERvA construction project, with the United States Department of Energy. Construction support also was granted by the United States National Science Foundation under NSF Award PHY-0619727 and by the University of Rochester. Support for participating scientists was provided by DOE and NSF (USA) by CAPES and CNPq (Brazil), by CoNaCyT (Mexico), by CONICYT (Chile), by CONCYTEC, DGI-PUCP and IDI/IGI-UNI (Peru), by the Latin American Center for Physics (CLAF) and by FASI(Russia). The MINERvA Collaboration wishes to express its thanks to the MINOS Collaboration for the use of its near detector data, reconstruction, calibration and simulation. Finally, the authors are grateful to the staff of Fermilab for their contribution to this effort, during the design, construction, data taking and data analysis phases of the experiment.

## References

- [1] S. Kopp, FERMILAB-CONF-05-093-AD, Proceedings of the 2005 Particle Accelerator Conference, Knoxville, TN [arxiv: \[physics\] 0508001](#); A.G. Abramov *et al.*, Nucl. Instr. and Meth. A485 (2002) 209.
- [2] K. Abe et al. [T2K Collaboration], Phys. Rev. Lett. 107 (2011) 041801.

- [3] D. S. Ayres et al. [NOvA Collaboration], hep-ex/0503053.
- [4] K. Abe, T. Abe, H. Aihara, Y. Fukuda, Y. Hayato, K. Huang, A. K. Ichikawa and M. Ikeda et al., arXiv:1109.3262 [hep-ex].
- [5] T. Akiri et al. [LBNE Collaboration], arXiv:1110.6249 [hep-ex].
- [6] D. G. Michaels et al., [MINOS Collaboration] Nucl. Instr. and Meth. A596 (2008) 190.
- [7] J. J. Chvojka, “Anti-Neutrino Charged Current Quasi-Elastic Scattering in MINERvA,” FERMILAB-THESIS-2012-22.
- [8] C. Andreopoulos et al., Nucl. Instr. and Meth. A614 (2010) 87, and [www.genie-mc.org](http://www.genie-mc.org).
- [9] S. Agostinelli et al., Nucl. Instr. and Meth. A506 (2003) 250, and J. Allison et al., IEEE Trans. Nucl. Sci. 53 (2006) 270.
- [10] P. Adamson et al., Phys. Rev. D. 81 (2010) 072002.
- [11] Eljen Technology, [www.eljentechnology.com](http://www.eljentechnology.com).
- [12] E. Gallas and J. Li, “Polishing Optical Fibers for the D0 ICD in Run II”, FNAL-TM-2062, 1998.
- [13] S. Aota et al., Nucl. Instr. and Meth. A357 (1995) 71.
- [14] R. Blair et al., [CDF Collaboration], CDF II Technical Design Report, FERMILAB-Pub- 96/390-E, 1996, p. 9-1.
- [15] Heigl Technologies, [www.heigltech.com](http://www.heigltech.com).
- [16] N. Tagg et al., Nucl. Instr. and Meth. A539 (2005) 668.
- [17] J. Estrada, C. Garcia, B. Hoeneisen, and P. Rubinov, “MCM II and the TriP Chip”, Aug 2002, FERMILAB-TM-2226.

- [18] G.N. Perdue et al., Nucl. Instr. and Meth. A694 (2012) 179.
- [19] R. Fruhwirth, Nucl. Instr. and Meth. A262 (1987) 444.
- [20] R. Luchsinger and C. Grab, Comp. Phys. Comm. 76 (1993) 263.
- [21] S.M. Ross, J. Eng. Tech., 20 (38) 2003.
- [22] P. Adamson et al., Nucl. Instr. and Meth. A492 (2002) 325.
- [23] J. Rademacker, Nucl. Instr. and Meth. A484 (2002) 432.
- [24] Photomultiplier Tubes: Basics and Applications, Edition 3A, Hamamatsu Photonics K.K., 2007.
- [25] P.S. Auchincloss et al., Nucl. Instr. and Meth. A343 (1994) 463.
- [26] N. Tagg et al., Nucl. Instr. and Meth. A539 (2005) 668-678.
- [27] R. OSPANOV, Ph.D. thesis, University of Texas at Austin (2008).
- [28] P. Adamson et al. [MINOS Collaboration], Phys. Rev. D 81 (2010) 072002, [arXiv:0910.2201 [hep-ex]].
- [29] THE MINOS COLLABORATION, *P-875: A Long-baseline Neutrino Oscillation Experiment at Fermilab*, Technical report (1996) 105.